The Dissertation Committee for Tianfei Liu Certifies that this is the approved version of the following Dissertation:

Rheology and Wall Slip of Soft Particle Glasses

Committee:

Roger T. Bonnecaze, Supervisor

Michel Cloitre

Venkat Ganesan

Thomas M. Truskett

Rheology and Wall Slip of Soft Particle Glasses

by

Tianfei Liu

Dissertation

Presented to the Faculty of the Graduate School of

The University of Texas at Austin

in Partial Fulfillment

of the Requirements

for the Degree of

Doctor of Philosophy

The University of Texas at Austin

May, 2021

Acknowledgments

I'd like to thank my supervisor Dr. Roger Bonnecaze for his great mentorship. He's always been encouraging, supportive, and inspiring throughout the whole journey of my PhD study. He sets a great example, not only by his passion for academic research but also by his extraordinary character which is caring, compassionate, and being responsible. I got inspired by him over and over again beyond the research on working methods and life attitudes.

I'm very grateful to Dr. Michel Cloitre, who provides insightful guidance in many parts of my research work. He motivates me with his thoughtfulness, industriousness, and dedication; encourages me to enjoy the inevitable uncertainty of scientific explorations.

I'm grateful that I choose to study in the department of chemical engineering at UT Austin. I want to thank my committee members, Dr. Venkat Ganesan and Dr. Tom Truskett for their insights and suggestions. I want to thank all the supportive staff members, especially Randy Rife, Jason Barborka, Eloise Boisjoli, Kate Baird.

I want to thank all my fellow Bonnecaze group members. Thanks to Fardin Khabaz for being a great collaborator in the research. Thanks to all the other group members, including Soumik Das, Shruti Jain, Benjamin Huntington, Mohammadreaza Shafiei, Xilan Zhu, Yang Ban, Mark Ferraro, Talha Arshad, Michael Clements, Andrew Spann, Meghali Chopra, Akhilesh Jain, Steven Stanley, Ali Shahmohammadi, Shreyas Sudhaman, and Monica Zakhari, with whom I have shared interesting conversations, and quality time.

I want to thank my friend Cheng Chen, Yue Zhang, Yifei Xu, and many other friends I get to know during my study at UT. I feel lucky to have these friends. Their friendship has made my life more enjoyable during my study.

I also want to thank all my family members for all their love and support, my dear parents, my grandparents, my uncles, aunts, and cousins.

I gratefully acknowledge support from the William and Bettye Nowlin Chair of Engineering at UT Austin.

Rheology and Wall Slip of Soft Particle Glasses

Tianfei Liu, Ph.D.

The University of Texas at Austin, 2021

Supervisor: Roger T. Bonnecaze

Soft particle glasses (SPGs) are highly concentrated suspensions of deformable particles above random close-packing for hard spheres. SPGs have wide applications in many areas including tissue engineering, drug delivery, etc. Three aspects of SPGs are studied in this dissertation.

Minimal interparticle interactions are identified as necessary for a particle dynamics simulation to predict the structure and flow behavior of soft particle glasses. Generally, two kinds of forces between the particles must be accounted for in simulations of SPGs: far field drag forces are required to dissipate energy in the simulations, and elastic forces are found to be dominant compared to near field frictional forces. The shear stress, the first and second normal stress differences for different interparticle force laws collapse onto universal master curves of the Herschel–Bulkley form by non-dimensionalization.

The behavior of the storage and loss moduli for jammed SPGs is studied computationally for a variety of interparticle potentials and volume fractions. The qualitative behavior of the storage modulus is independent of the nature of the interparticle potential. The storage modulus follows a universal sigmoidal curve for non-dimensionalized values of the frequency. The qualitative nature of the loss modulus depends on the nature of the near-field drag force between the soft particles. At moderate to high frequency, the loss modulus increases with the frequency according to a power law whose exponent is related to the drag force law.

Wall slip is an important aspect since it is an inseparable part of characterizing and processing SPG materials. Two simulation frameworks are built to serve as tools to understand, explore and investigate the wall slip process. Both frameworks work for shear between rough-

rough walls, with matching results from bulk rheology, which proves their validity. One framework works for shear between rough-smooth walls, with fixing randomly selected particles on the smooth wall, which sheds light on the linear regime between slip velocity and slip stress. 15 percent of stuck particles on the smooth wall would have a similar no-slip effect as a rough wall. The inclusion of elastohydrodynamic forces and stuck particles reduces the slip velocity given the same slip stress.

Table of Contents

List of Tables

List of Figures

Chapter 1: Introduction

1.1 WHAT ARE SOFT PARTICLE GLASSES?

Soft particle glasses (SPGs) are dispersions of highly concentrated soft particles beyond random close packing fraction of hard spheres, which is around 0.64 (Berryman, 1983). Examples of soft particles include microgels, emulsions, micelles, star polymers, polymer coated particles and vesicles as illustrated in Figure 1.1 (Mohan, 2013).

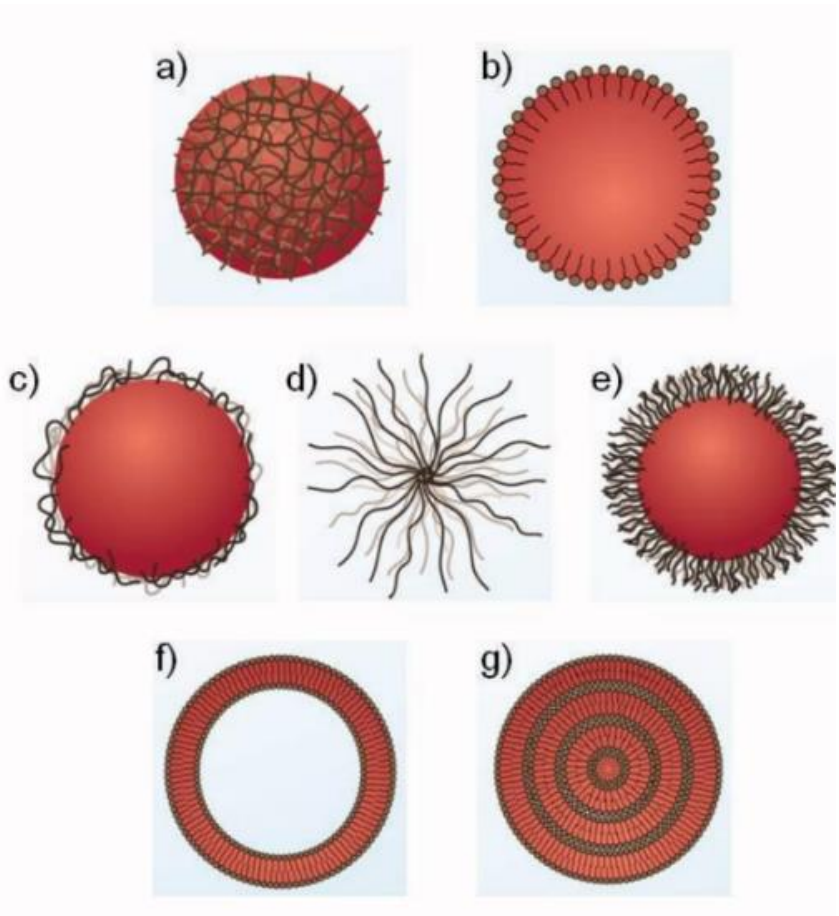

Figure 1.1: Schematic of some examples of soft particles. (a) microgel; (b) emulsion droplet; (c) solid particle covered with adsorbed or grafted polymer chains; (d) star polymer; (e) block copolymer micelle; (f) liposome; (g) multi-lamellar vesicle (Mohan, 2013)

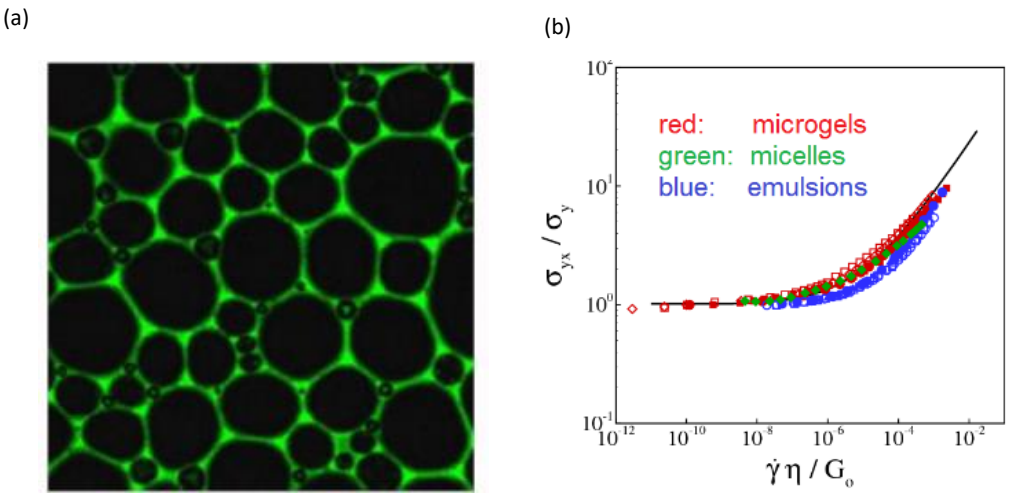

Figure 1.2: (a) Example of highly jammed soft particle glass: aqueous foam under a confocal microscope (Mohan, 2013); (b) nondimensional flow curves for microgels, micelles and emulsions showing in one plot.

Soft particles behave like hard spheres at low volume fractions in dilute suspensions. As the volume fraction increases above 0.58, they begin to exhibit glassy behavior and each particle is trapped in a cage formed from its neighbors which results in entropic elasticity that is thermally activated. At higher volume fractions beyond the random close packing limit, facets begin to form between crowded neighboring particles and the repulsive particle-particle interactions result in a soft solid with an elastic modulus and yield stress of the whole system (Figure 1.2). The jamming together of the particles leads to a cage around each particle that it must break through for the suspension to flow. This gives rise to a yield stress; once beyond the yield stress, the suspension is shear thinning.

SPGs have intermediate properties of both solids and liquids: after deformation, they retain their shape like solids if the stress is below the yield stress, and they will flow like liquids if the stress is beyond yield stress. The unique properties of SPGs make them useful as additives to modify and control rheological properties and their wide applications include personal care and food products, high-performance coating, and material processing aids (Saunders & Vincent, 1999; Thorne, Vine, & Snowden, 2011; Vlassopoulos & Cloitre, 2014).

1.2 RECENT APPLICATIONS OF SPGS

1.2.1 Biomedical and pharmaceutical applications

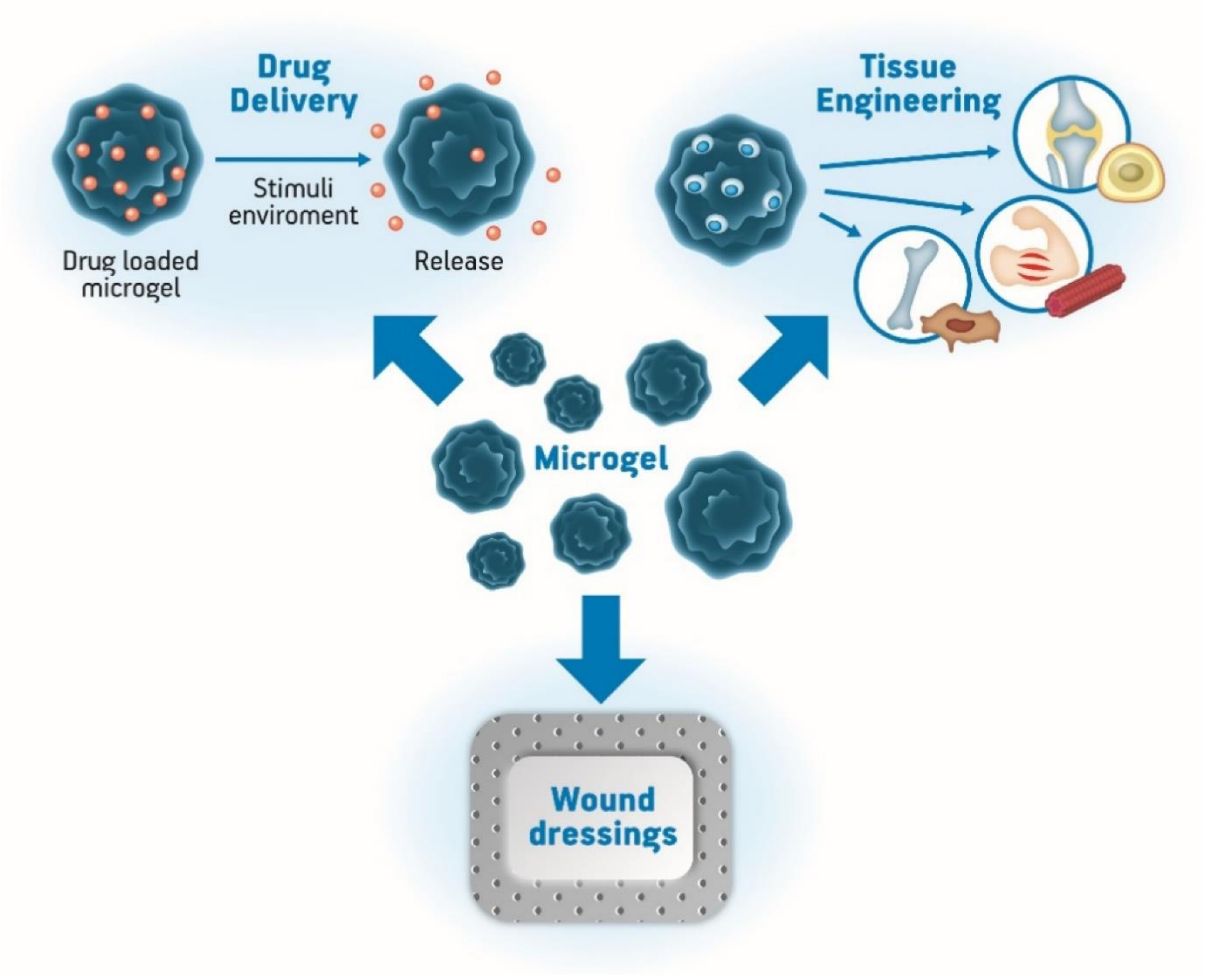

Figure 1.3: Biomedical applications of microgel (de Lima et al., 2020)

Microgels have great potential in drug delivery, tissue engineering, and wound dressings in the biomedical and pharmaceutical fields (de Lima et al., 2020; Wang, Guo, Dong, Cui, & Hao, 2019). They are widely used as biomaterials and nanomedicines because of their high water content, high surface area due to porosity, nontoxicity, biodegradability, abundancy, and relatively low cost.

Microgels can serve as reliable carriers for drug delivery. One example is in the area of delivery of chemotherapy for cancer treatment. Many microgel-based polymer drug delivery

systems have been developed to target cancer cells more specifically, thus avoiding the limitation of the low specificity of chemo treatments (Eswaramma, Reddy, & Rao, 2017; Ranquin, Versées, Meier, Steyaert, & Van Gelder, 2005). They can provide stabilization, reduce toxicity, control the release rate and protect sensitive drugs from degradation (Bysell, Månsson, Hansson, & Malmsten, 2011; Jooybar, Abdekhodaie, Mousavi, Zoetebier, & Dijkstra, 2019; Lopez, Hadgraft, & Snowden, 2005; Wu, Böttcher, & Haag, 2015).

Another promising application of jammed microgels is in the area of 3D bioprinting (Bhattacharjee & Angelini, 2018; Highley, Song, Daly, & Burdick, 2019; Hipfinger et al., 2020; Jeon, Lee, Hinton, Feinberg, & Alsberg, 2019; Subbiah et al., 2020). Many research groups have proposed bioinks composed exclusively of jammed microgels to replace traditional soft hydrogels, which can be difficult to be used as bioinks without additional modification or the use of additives (Jungst, Smolan, Schacht, Scheibel, & Groll, 2016; Moroni et al., 2018).

Microgels can be innovatively used in tissue engineering beyond being used as bioinks. For example, a team led by Eben Alsberg has developed an internal-scaffold free platform to print stem-cell-only bioink into 3D tissues using photocurable, self-healing, and shear-thinning alginate microgel supporting bath (Dang et al., 2017). The microgel could heal under UV light and form a medium to hold the printed stem cells in place. This process overcomes the limitation of scaffold which could bring cytotoxicity and interrupt cell-cell interaction.

Other interesting applications of microgels include being used as wound dressings which can release antibacterial zinc ions(Wilke et al., 2015); being used as biosensors for glucose to manage the release of insulin (Matsumoto et al., 2012); being used as biological lubricants to treat osteoarthritis (Wang et al., 2019).

1.2.1 Environmental protection

Microgels loaded with inorganic nanoparticles have been of great interest to reduce toxic chemicals including nitroarenes and organic dyes as catalytic systems (Shahid et al., 2020). Traditionally toxic chemicals are treated by techniques such as oxidation, reduction, and

physical methods like adsorption, which are usually associated with high operating cost and energy consumption. Many hybrid nanocatalytic microgel systems have shown great potential as more energy-efficient, environmental-friendly treatment of waste water using catalysts such as metal (Corma, Concepción, & Serna, 2007), metal oxide (Gupta et al., 2012), metal sulfide (Bahnemann, 2004), and bimetallic (Gao et al., 2003) nanoparticles.

1.2.3 Food industry

Foam is an essential component in the processing of many food industry products including bread, cakes, carbonated, creams, mousses et al.(B. S. Murray, 2020). Egg white protein is the dominant conventional foaming agent to stabilize foams. Motivated by consumer trends for more plant-based alternatives, novel stabilizers to replace egg proteins have been a popular literature subject, particularly with Pickering foams. Converting the protein into protein microgels or nanoparticles is one way of improving the foaming properties of foam (Dickinson, 2015; Mohammadian & Madadlou, 2018; Brent S Murray, 2019; Peng et al., 2018; Wouters, Schaefer, Joye, & Delcour, 2019). Novel, non-protein-based systems are also a popular research area including using modified polysaccharides (Beatrice et al., 2017; Bertsch & Fischer, 2020; Tzoumaki, Karefyllakis, Moschakis, Biliaderis, & Scholten, 2015).

1.3 Outline of Dissertation

1.3.1 Origin of universality and minimal ingredients

In order to explain the universal flow properties of soft glassy materials as introduced in 1.1, many pairwise 2D force models have been proposed to describe and capture the behavior of these materials (Chaudhuri, Berthier, & Bocquet, 2012; Cloitre & Bonnecaze, 2017; Durian, 1997; Langlois, Hutzler, & Weaire, 2008; Mansard, Colin, Chaudhuri, & Bocquet, 2013; Nordstrom et al., 2010; Tighe, Woldhuis, Remmers, van Saarloos, & van Hecke, 2010). These 2D models have provided useful insights in describing the various insights in the rheology of

soft matter materials. In all of these models, mechanisms of storing and dissipation energy are built via elastic forces and viscous drag forces.

All these are basic 2-D models that use similar frameworks to each other, and only a few 3-D models have been established. It is still unknown if the microscopic ingredients to store and dissipate energy are essential in 3-D models as in 2-D models, how the exact form of the interparticle forces would influence macroscopic rheology, and whether the obtained results are universal via proper scaling across different forces. We propose to use a 3D model that is based on pairwise interactions to explore these open questions. To answer this question, the following are determined in Chapter 2:

- The critical forces and their form in the pairwise force model of SPGs;
- The importance of different elastic and viscous forces in determining the final flow curve;
- How flow curves from different forces models are collapsed using proper scaling.

1.3.2 Behavior of storage and loss moduli of jammed soft particles at high frequency

The low frequency limit G_0 of storage modulus G' is an important characteristic property of these materials and often encompasses the volume fraction dependency in non-dimensionalizations. In previous simulation and experimental research, G_0 has been used very effectively for collapsing rheological data like shear stress and normal stress difference of different systems onto universal curves(Cloitre, Borrega, Monti, & Leibler, 2003; T. Liu, Khabaz, Bonnecaze, & Cloitre, 2018). For the viscous force side of the system, loss modulus G'' is also important in understanding the relaxation of the material.

Storage and loss moduli can be measured by imposing small amplitude oscillatory shear (SAOS), which explores the linear viscoelastic regime of the material. It's always been a challenge to measure high-frequency SAOS rheology of complex fluids experimentally where classic time-temperature superposition doesn't apply(Plazek, 1996) considering the frequency limitations of conventional rheometers. Simulations measuring storage and loss moduli could provide insights beyond the limitations of experiments. While the high frequency modulus G_∞

follows the theoretical prediction of the Mountain-Zwanzig formula (Zwanzig & Mountain, 1965), which depends on the pair distribution function and interparticle potential, no such formula exists for the low frequency modulus G_0. The natural question following this would be, how does the system transition gradually from G_0 to G_∞ frequency increases? To address this question, the following are uncovered in Chapter 3:

- The behavior of the storage and loss moduli for jammed soft particles over a range of different frequencies computationally;
- The impact of interparticle potentials and volume fractions;
- The universality despite interparticle potential or volume fraction differences.

1.3.3 Modelling of wall slip behavior

Wall slip is a fundamental component of the rheology of soft particle pastes in many natural phenomena and industrial processes (Cloitre & Bonnecaze, 2017; Hatzikiriakos, 2015). The identification and proper correction of slip's influence are necessary to guarantee the accuracy in rheological characterization and experiments of soft glass materials. It's also significant during the applications and use of soft glassy materials as slip over certain surfaces is a fundamental property of these materials which cannot be avoided.

Several previous experimental publications (Seth, Cloitre, & Bonnecaze, 2008; Seth, Locatelli-Champagne, Monti, Bonnecaze, & Cloitre, 2012) have shown how the flow of soft particle glasses is influenced over macroscopic distances by the chemistry and roughness of the solid surface. For slip over smooth repulsive surfaces, the slip is divided into two different regimes depending on whether the slip stress is larger than the yield stress: below the yield stress, elastohydrodynamic forces play a dominant role in determining the parabolic slip stress versus slip velocity relationship; whereas above the yield stress, the relationship is linear. The microscopic origin behind these experimental observations is essentially unknown. The goal of this part of my research is to develop a microscopic model and use simulation to answer the following questions. How does the wall influence and determine the movements of soft particles through their interactions? What degree of roughness is enough to suppress wall slip?

What’s the role of elastohydrodynamic forces in wall slip, especially in the linear regime? To answer these questions, the following topics are decided in Chapter 4:

- Simulation model systems of soft particles shearing with walls;
- Wall slip behavior with different walls (including rough wall and smooth wall) using the established models;
- The impact of different parameters, for example, roughness, forces, on wall slip behavior.

Chapter 2: Universality of the Flow Properties of Soft-Particle Glasses*

2.1 INTRODUCTION

Soft particle glasses (SPGs) are composed of deformable particles that are jammed at volume fractions beyond close-packing. They cover a wide range of materials such as microgels, emulsions, block copolymer micelles, and star polymers (Bonnecaze & Cloitre, 2010). They show elastic solid behavior at rest and flow under stresses larger than the yield stress. These characteristics make them useful for coating applications, paints, pastes, textured foods, and cosmetic products (Thorne et al., 2011). Similar to hard sphere glasses, soft particle glasses demonstrate nonergodicity and caged dynamics (Vlassopoulos & Cloitre, 2014). However, while hard sphere glasses only experience forces due to excluded volume interactions, soft particle glasses are compressed via a bulk osmotic force and interact through an elastic repulsive potential. The phase diagram of soft particle suspensions shows strong similarities with that of hard spheres (Vlassopoulos & Cloitre, 2014). Many systems like emulsions or microgels exhibit the same sequence of fluid, entropic glass, and soft glass phases upon increasing the density (Pellet & Cloitre, 2016; Scheffold, Cardinaux, & Mason, 2013). For relatively monodisperse suspensions, jamming takes place at a volume fraction of about 0.64. Above the jamming point, thermal or Brownian forces become negligible compared to contact forces, which determine the microstructure and macroscopic properties.

The shear stress σ of soft particle glasses is well represented by the Herschel-Bulkley equation (Bonn, Denn, Berthier, Divoux, & Manneville, 2017):

---

*Part of this chapter has been published in Liu, T., Khabaz, F., Bonnecaze, R. T., & Cloitre, M. (2018). On the universality of the flow properties of soft-particle glasses. *Soft Matter*, *14*(34), 7064-7074. (T. Liu et al., 2018) DOI: 10.1039/C8SM01153B

$$\sigma = \sigma_y + k\dot{\gamma}^m, \tag{2.1}$$

where σ_y is the yield stress, k the consistency, and m the so-called Herschel-Bulkley exponent. For a long time, this equation has been considered as a purely empirical, albeit convenient, tool for characterizing the nonlinear rheology of yield stress materials. More recently the problem has stimulated a lot of research with the objective to connect the microscopic properties and the macroscopic rheology of soft particle glasses (Bonn et al., 2017; Bonnecaze & Cloitre, 2010; Vlassopoulos & Cloitre, 2014). Important questions concern the origin and the prediction of the yield stress, the values of the parameters involved in the Herschel-Bulkley equation, and in particular the exponent m. Careful experiments on well-characterized SPGs have demonstrated that the Herschel-Bulkley equation provides a good description of the flow properties of SPGs with an exponent close to 0.5 (Basu et al., 2014; Becu, Manneville, & Colin, 2006; Cloitre et al., 2003; Denkov, Tcholakova, Golemanov, Ananthapadmanabhan, & Lips, 2008; Nordstrom et al., 2010; Paredes, Michels, & Bonn, 2013; Pellet & Cloitre, 2016; Seth, Mohan, Locatelli-Champagne, Cloitre, & Bonnecaze, 2011). Besides, the flow curves measured for different particle densities have been found to collapse onto master curves when the stress and the shear rates are rescaled by appropriate parameters (Basu et al., 2014; Cloitre et al., 2003; Nordstrom et al., 2010; Paredes et al., 2013; Pellet & Cloitre, 2016; Seth et al., 2011). These experimental findings have stimulated an intense theoretical activity resulting in a variety of descriptions based on scaling methods (Lin, Lerner, Rosso, & Wyart, 2014), STZ theory (Langer, 2015). phenomenological models like the SGR model (Sollich, 1998), and elastoplastic models and its many variants (Agoritsas & Martens, 2017; Bocquet, Colin, & Ajdari, 2009; Hébraud & Lequeux, 1998; Lin & Wyart, 2018; A. Nicolas & Barrat, 2013; Alexandre Nicolas, Martens, & Barrat, 2014; Puosi, Olivier, & Martens, 2015). However many features of the flow properties of soft particle glasses remain poorly understood.

Microscopic models have also been developed in order to describe and capture the macroscopic flow behavior of jammed suspensions in relation with their particle scale behavior (Chaudhuri et al., 2012; Durian, 1995, 1997; Langlois et al., 2008; Lemaître & Caroli, 2009; Mansard et al., 2013; P. Olsson & Teitel, 2012; Tighe et al., 2010). In 2D the particles are represented by circular disks which, when overlapping and only then, interact via repulsive forces. The repulsive force between two particles α and β depends on the overlap distance $h_{\alpha\beta} = R_\alpha + R_\beta - r_{\alpha\beta}$, where R_α and R_β are the radii of the particles and $r_{\alpha\beta}$ is their center-to-center distance. The second key ingredient is the viscous dissipation force, which in general is assumed to be the sum of the drag forces exerted on each particle by its neighbors. In general an external force is applied to keep the suspension moving and provide the applied shear strain and strain rate. Inertia is generally neglected or made negligible resulting in strongly overdamped motion. In his pioneering work, Durian took an elastic repulsive force derived from a harmonic potential and for simplicity computed the dissipation with respect to the imposed average linear shear velocity flow. Inertia was neglected. The resulting flow curves were found to obey the Bingham equation (m = 1 in Eq. 2.1). Later on Langlois *et al.* allowed the particles to move independently so that the drag force between two particles was computed in proportion to their relative difference and not with respect to the background fluid velocity (Langlois et al., 2008). A mass was attributed to particles but it was small enough to make inertia negligible. The flow curves were found to obey the Herschel-Bulkley equation with an exponent m close to 0.5. Different authors have implemented the soft-disk model with harmonic interactions and drawn similar conclusions (Chaudhuri et al., 2012; P. Olsson & Teitel, 2012). Tighe *et al*. identified four different shear rate dependent regimes, namely yield stress, transition, critical and viscous regimes (Tighe et al., 2010). In the critical regime, the flow curve was characterized by a Herschel-Bulkley exponent of 0.5 whereas, in the viscous regime at very high shear rates, it followed the Bingham equation. The exponent $m \cong 0.5$ has

also been observed in molecular dynamic simulations of 2D athermal Lenard-Jones glasses (Fusco, Albaret, & Tanguy, 2014; Lemaître & Caroli, 2009; Alexandre Nicolas et al., 2014; Puosi et al., 2015).

These models are 2D in essence, which raises the question of whether they are representative of experiments. Actually, only a few 3D simulation schemes have been developed to investigate the flow of jammed materials (Gross, Krüger, & Varnik, 2014; Seth et al., 2011; Vasisht, Dutta, Del Gado, & Blair, 2018). It is not yet clear if and how the microscopic ingredients of the models influence the macroscopic rheology and whether the results which have been obtained are general. The main questions concern the form of the repulsive forces acting on the particles and the nature of the viscous drag forces that controls the dissipation. In this paper we address these issues using a 3D micromechanical model that we have shown to successfully describe the linear and nonlinear rheology of jammed SPGs, and produce shear stress and normal stresses predictions in quantitative agreement with steady and oscillatory experiments (Mohan, Pellet, Cloitre, & Bonnecaze, 2013; Seth et al., 2011). We implement different repulsive forces corresponding to varying softness and explore the role of the dissipative drag force between particles. We show that the non-linear rheological properties depend on the expressions of the viscous and elastic forces but that the shear stress and normal stresses difference can be rescaled on similar universal Herschel-Bulkley master curves once the elastic modulus is used as the control parameter.

2.2 COMPUTATIONAL METHOD

2.2.1 Model description and equations of motion

The suspension consists of particles with a Young modulus E, dispersed in a solvent of viscosity η_S, at a volume fraction ϕ. As depicted in Figure 2.1a, the jammed

suspension flows in the *x*-direction and is subject to a velocity gradient $\dot{\gamma}$ in the *x*-*y* plane. The motion of each particle is determined by the sum of the pairwise forces exerted by the neighboring particles, which can be categorized into dissipative drag forces $\mathbf{f}_{\alpha}^{\text{drag}}$ and interparticle repulsive forces associated with elastic interactions $\mathbf{f}_{\alpha\beta}^{\text{elas}}$. The total drag forces are split into two contributions, namely the far-field drag force $\mathbf{f}_{\alpha\beta}^{\text{far-drag}}$ and the near-field drag force $\mathbf{f}_{\alpha\beta}^{\text{near-drag}}$.

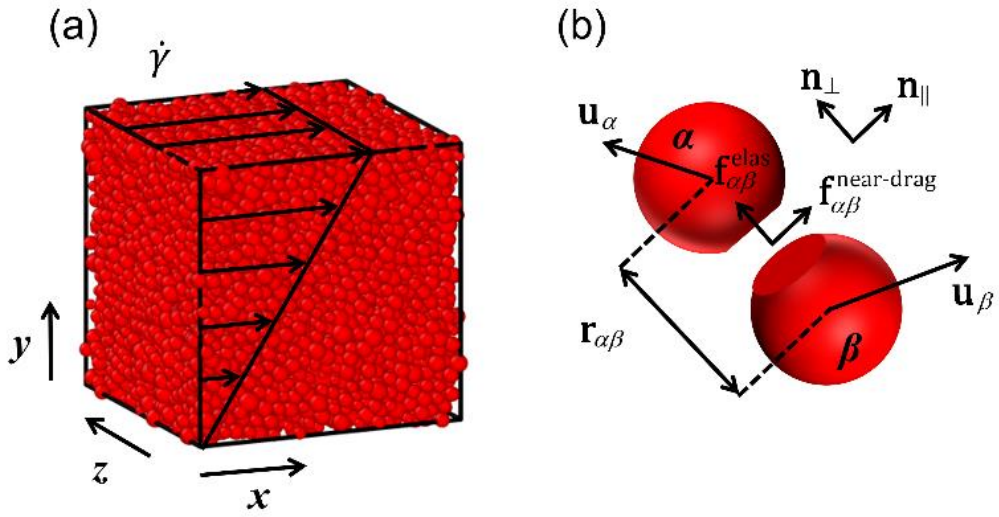

Figure 2.1: Schematic representation of a sheared suspension (a) and pairwise interaction (b).

2.2.1.1 Elastic forces $\mathbf{f}_{\alpha\beta}^{\text{elas}}$

Elastic forces are the normal forces acting on the contacting facets between a particle and their neighbors. They are responsible for the mutual repulsion between two neighboring particles In the original version of the model (Seth et al., 2011), the repulsive elastic force has the form of a modified Hertzian force, which is known to well

represent the repulsive forces between two elastomeric particles (K. K. Liu, Williams, & Briscoe, 1998):

$$\mathbf{f}_{\alpha\beta}^{\text{elas}} = \frac{4}{3} C E^{*} \varepsilon_{\alpha\beta}^{n} R_c^2 \mathbf{n}_{\perp}, \tag{2.2}$$

where $E^{*} = E / 2(1-\nu^2)$ is the contact modulus based on the Young modulus E and Poisson ratio ν, $R_c = R_\alpha R_\beta / (R_\alpha + R_\beta)$ is the contact radius, $\varepsilon_{\alpha\beta} = \left(R_\alpha + R_\beta - r_{\alpha\beta}\right) / R_c$ is the dimensionless overlap distance characterizing the degree of compression, and $\mathbf{n}_{\perp}$ is the unit vector perpendicular to the flat surface representing the particle-particle contact. The values of C and n change with $\varepsilon_{\alpha\beta}$ as follows: when $0 < \varepsilon_{\alpha\beta} \le 0.1$, n = 1.5 and C = 1; when $0.1 < \varepsilon_{\alpha\beta} \le 0.2$, n = 3 and C = 31.62; when $\varepsilon_{\alpha\beta} > 0.2$, n = 5 and C = 790.6. This piecewise form takes into account the nonlinear elasticity of the particles and ensures that the elastic force for large overlap is larger than in classic Hertz theory (Bonnecaze & Cloitre, 2010; K. K. Liu et al., 1998). This form is used in Section 3.1, where we investigate the influence of the drag forces on the flow curves. When inspecting the influence of the force law in Section 3.2, a simplified form of Eq. 2.2 is used where C is set to be 1 and the value of the elastic exponent n is set to be 1.5, 3 and 5 separately, which correspond to force laws with different softness.

2.2.1.2 Far-field drag force $\mathbf{f}_{\alpha}^{\text{far-drag}}$

The far-field drag force $\mathbf{f}_{\alpha}^{\text{far-drag}}$ on particle α is a hindered Stokes drag originating from the velocity difference between the imposed flow field and particle α:

$$\mathbf{f}_{\alpha}^{\text{far-drag}} = b(\langle \mathbf{u}_{\beta} \rangle - \mathbf{u}_{\alpha}) = \frac{6\pi R \eta_s}{f(\phi)} (\dot{\gamma} y_{\alpha} \mathbf{e}_x - \mathbf{u}_{\alpha}). \tag{2.3}$$

It is referred to as a far-field drag term in relation with Stokesian dynamics. It has the same form as in the initial Durian model except for the expression of the dissipation constant in the prefactor. The latter involves the average radius of the particle *R*, the interstitial fluid viscosity η_s, and a term $f(\phi)$ that is the hindered settling coefficient that accounts for the reduced mobility of the particles at high volume fractions. The value of 0.01 used for this coefficient in the following is the estimated value for a suspension of spheres near close-packing (Phillips, Brady, & Bossis, 1988). It can be easily shown that changing $f(\phi)$ affects the characteristic time scale for dissipation and is thus equivalent to translating the flow curves along the shear rate axis.

2.2.1.3 Near-field drag force $\mathbf{f}_{\alpha\beta}^{\text{near-drag}}$

The particles do not collide like in granular materials but come into close contact forming flat facets to generate elastic and near-drag forces. The near-field drag force $\mathbf{f}_{\alpha\beta}^{\text{near-drag}}$ is the tangential force acting on the flat contacting surface between neighboring particles as shown in Figure 2.1b. Two different forms of near-field drag forces are used in the simulation to test the importance of the near-field contribution: an elastohydrodynamic drag force (EHD) $\mathbf{f}_{\alpha\beta}^{\text{EHD}}$ and a Coulombic frictional force $\mathbf{f}_{\alpha\beta}^{\text{C}}$.

The elastohydrodynamic drag force $\mathbf{f}_{\alpha\beta}^{\text{EHD}}$ arises from a coupling between the hydrodynamic pressure in the lubrication film separating two particles and the elastic repulsion force between them and is given by

$$\mathbf{f}_{\alpha\beta}^{\text{EHD}} = -\left(\eta_S C u_{\alpha\beta,\|} E^* R_c^3\right)^{1/2} \varepsilon_{\alpha\beta}^{(2n+1)/4} \mathbf{n}_{\alpha\beta,\|}. \tag{2.4}$$

where $\mathbf{n}_{\alpha\beta,\|} = \mathbf{u}_{\alpha\beta,\|} / \left|\mathbf{u}_{\alpha\beta,\|}\right|$ is a unit vector parallel to the relative velocity in the direction parallel to the contact surface, $\mathbf{u}_{\alpha\beta,\|}$. $\left|\mathbf{u}_{\alpha\beta,\|}\right|$ is also noted as $u_{\alpha\beta,\|}$. This formula was

originally derived for a single particle dragged along a smooth surface (Seth et al., 2008). Parameters C, E^*, R_c, and $\varepsilon_{\alpha\beta}$ are as defined in Eq. 2.2. The EHD force is computed using the difference between the center of mass velocities. It is to note that, in the jamming regime, the local elastic forces that trap the particles hinder their rotation, which accordingly is not considered in the simulations (Dagallier, Cardinaux, Dietsch, & Scheffold, 2012).

The tangential Coulombic frictional force $\mathbf{f}_{\alpha\beta}^{C}$ is defined with respect to the normal repulsive force $\mathbf{f}_{\alpha\beta}^{\text{elas}}$ assuming a simple linear relationship:

$$\mathbf{f}_{\alpha\beta}^{C} = -\mu f_{\alpha\beta}^{\text{elas}} \mathbf{n}_{\alpha\beta,||} \tag{2.5}$$

where again $\mathbf{n}_{\alpha\beta,||}$ is a unit vector parallel to the tangential velocity $\mathbf{u}_{\alpha\beta,||}$. Because the contacts between soft repulsive particles like particle gels or emulsion droplets are lubricated by the solvent, it is assumed here that there is little or no static friction (Gong, Iwasaki, Osada, Kurihara, & Hamai, 1999).

2.2.1.4 Equation of motion

In SPGs the movement of the particles is slow and highly constrained by their jammed environment. For typical SPGs simulations, $\rho \approx 10^3 \text{kg/m}^3$, $R \approx 10^{-7}\text{m}$, $\eta_s \approx 10^{-3}\text{Pa}\cdot\text{s}$ and the shear rate $\dot{\gamma}$ falls between $10^{-9}\text{s}^{-1} - 10^{-3}\text{s}^{-1}$. The Reynolds number $\text{Re} = \rho\dot{\gamma}R^2/\eta_s$ ranges from 10^{-17} to 10^{-11}, and so inertia can be neglected, resulting in overdamped motion. Since all forces on each particle are balanced:

$$\mathbf{f}_{\alpha}^{\text{far-drag}} + \sum_{\beta}\left(\mathbf{f}_{\alpha\beta}^{\text{near-drag}} + \mathbf{f}_{\alpha\beta}^{\text{elas}}\right) = \mathbf{0}\,. \tag{2.6}$$

The equation of motion that describes the trajectory of particle α is derived by expanding the $\mathbf{f}_{\alpha}^{\text{far-drag}}$ term in Eq. 2.6 using its form given by Eq. 2.3,

$$\frac{d\mathbf{x}_{\alpha}}{dt} = \mathbf{u}_{\alpha} = \dot{\gamma} y_{\alpha} \mathbf{e}_{x} + M_{\alpha} \sum_{\beta} \left(\mathbf{f}_{\alpha\beta}^{\text{near-drag}} + \mathbf{f}_{\alpha\beta}^{\text{elas}} \right), \tag{2.7}$$

where $\dot{\gamma}$ is the shear rate, y_{α} is the vertical location of the particle and $\mathbf{e}_{x}$ is the unit vector in the x direction; $M_{\alpha} = f(\phi)/6\pi R\eta_{s}$ is the mobility and is equivalent to the inverse of the dissipation constant in the Durian's model (Durian, 1995, 1997). $\mathbf{f}_{\alpha\beta}^{\text{near-drag}}$ can take the form of either the elastohydrodynamic drag force $\mathbf{f}_{\alpha\beta}^{\text{EHD}}$ or the Coulombic-like frictional force $\mathbf{f}_{\alpha\beta}^{\text{C}}$. In the following, the flow behavior is investigated using different models of $\mathbf{f}_{\alpha\beta}^{\text{near-drag}}$ and $\mathbf{f}_{\alpha\beta}^{\text{elas}}$.

2.2.2 Simulation and characterization method

The model is implemented using a particle dynamics simulation scheme on random packings of 10,000 elastic spheres confined in a cubic box that is periodically replicated. The radii of the spheres have a 20% polydispersity to avoid forming shear-induced structures at high shear rates (Khabaz, Cloitre, & Bonnecaze, 2018; Khabaz, Liu, Cloitre, & Bonnecaze, 2017). Suspensions with different volume fractions are prepared as follows. A glass-like structure is first created using the compression algorithm introduced by Lubachevsky and Stillinger (Lubachevsky & Stillinger, 1990). The close-packed configurations are compressed by reducing the box size in small steps until the desired volume fraction is achieved. Because the Poisson ratio for the particles is ½, their volume upon deformation remains constant. The volume fraction of the suspension is computed as the ratio between the total volume of the particles and the volume of the box. After each size variation, the system is allowed to relax using the

conjugate gradient algorithm so there is no net force on any of the particles. This procedure ensures that each particle has reached a mechanical equilibrium and no internal stress is trapped inside the suspension (Mohan, Bonnecaze, & Cloitre, 2013). The volume fractions investigated range from 0.70 to 0.90.

Constant shear rate simulations are performed using the granular package of LAMMPS (Plimpton, 1995). The shear rate is applied via Lees-Edwards boundary conditions. The position and the velocity of each particle are obtained by solving the N equations of motion above using the Euler integration algorithm (Rapaport, 2004). An explicit time integration scheme is used to solve the equations. First, the forces on the right hand side are evaluated from the position and velocity from the last time step; then the velocity and position on the left hand side are evaluated in the current time step.

The stress tensor that characterizes the flow properties is computed from the Kirkwood formula (R. G. Larson, 1999):

$$\boldsymbol{\sigma} = -\frac{1}{V}\sum_{\beta}^{N}\sum_{\alpha>\beta}^{N}\mathbf{f}_{\alpha\beta}(\mathbf{x}_{\alpha}-\mathbf{x}_{\beta}), \tag{2.8}$$

where V is the volume of simulation box, $\mathbf{f}_{\alpha\beta}$ is the total force between neighboring particles α and β including near-field drag force and elastic force, $\mathbf{x}_{\alpha}$ and $\mathbf{x}_{\beta}$ are the position vectors of α and β. Three component of the stress are reported later in the paper: the shear stress $\sigma = \sigma_{yx}$; the first normal stress difference $N_1 = \sigma_{xx} - \sigma_{yy}$; and the second normal stress difference $N_2 = \sigma_{yy} - \sigma_{zz}$.

The applied dimensionless shear rate $\eta_s\dot{\gamma}/E^*$ varies from 10^{-12} to 10^{-4}, depending on the specific repulsive force law. Simulations are conducted at sufficiently low shear rates to access the yield point of the suspension. All suspensions are sheared

for 100 strain units to ensure that they reach steady state and that no crystallization or layering occurs (Khabaz et al., 2018; Khabaz et al., 2017). Simulations at each volume fraction and shear rate are performed starting from at least three different initial configurations of particles in the periodically replicated suspension. Each initial configuration has the requisite volume fraction and polydispersity and is statically stable, i.e., the net force on the particles is zero. It is found that the initial condition does not affect the steady state flow curves.

As values of the stresses fluctuate throughout the simulation, average stress values over the last 80 strain units are calculated for each initial configuration. Then the stresses obtained for the different initial configuration are averaged and the standard deviations are calculated and plotted in the figures as error bars. Some error bars are smaller than the symbols. For each volume fraction, the variations of the shear, first, and second normal stress differences with the shear rate define flow curves that are fitted to the Herschel-Bulkley equation. For each flow curve, all the data available are included in the fits and the standard deviation of the individual data of the flow curves are taken into account. The quality of the fits is characterized by the confidence limits of the standard deviation reported for the parameters in S2.2.

The low-frequency shear modulus G is an important characteristic property of the suspension at rest. It can be computed either by subjecting the packing to an oscillatory shear deformation at small strain amplitude (Mohan, Pellet, et al., 2013) or equivalently by applying a quasi-static uniaxial stretching deformation (Lacasse, Grest, Levine, Mason, & Weitz, 1996; Seth, Cloitre, & Bonnecaze, 2006). In this work we use the second method. The packing is deformed step by step by increasing the uniaxial deformation in small increments in a quasi-static way. At each step, the periodic box is

stretched by a small amount and the particles are allowed to adjust their position with respect to their neighbors, so that they reach their local energy minimum. When the final deformation is reached, the extension ratio is $1 + \delta$ (δ<<1) and the low frequency modulus G is computed from the net change in energy ΔU with respect to the undeformed state (Lacasse et al., 1996; Mohan, Pellet, et al., 2013; Seth et al., 2006):

$$G \cong \frac{2}{3\delta^2}\frac{\Delta U}{V}. \tag{2.9}$$

2.3 RESULTS AND DISCUSSION

2.3.1 Static properties

In this section, we examine the effect of the repulsive force law on the low-frequency modulus and structural properties of SPGs. We compute the low-frequency modulus, the average contact number and the particle overlap from equilibrated packing configurations which are mechanically stable using different force laws given by Eq. 2.2 when C = 1 and n = 1.5, 3, and 5. Since there is no flow, the far-field and near-field hydrodynamic contributions are not included.

2.3.1.1 Low-frequency modulus

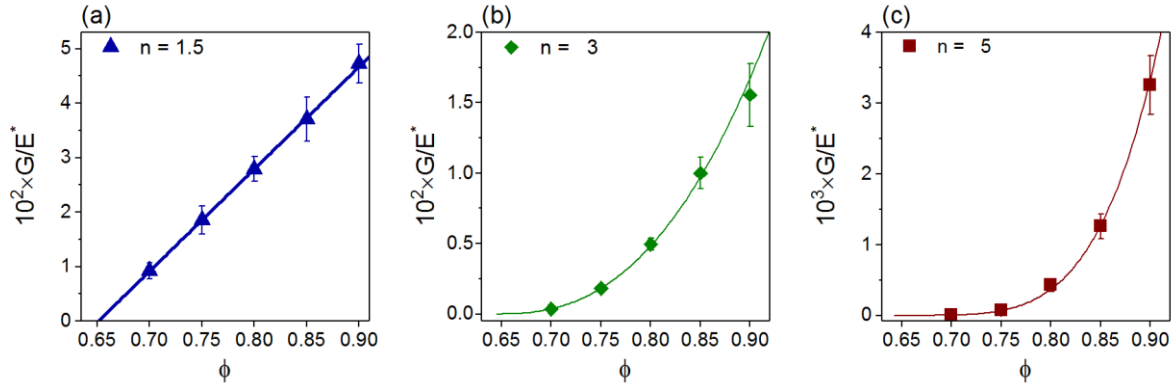

Figure 2.2: Variations of the low frequency modulus G versus the volume fraction for different values of the force law exponent n; from left to right: n = 1.5 (a), 3 (b), and 5 (c). The continuous lines are fits of the data to expression (10d) with $\gamma = 1$ ($\phi_c = 0.651 \pm 0.001$), $\gamma = 2.5$ ($\phi_c = 0.645 \pm 0.002$), $\gamma = 4.5$ ($\phi_c = 0.641 \pm 0.002$) for (a) to (c), respectively.

Figure 2.2 shows the variation of G computed for the different force laws. For each value of n, G increases with the volume fraction. However, we observe significant quantitative differences between the three graphs. The variations of G can be interpreted by considering that it is the product of the spring constant $k \propto \partial f_{\alpha\beta}^{\text{elas}} / \partial \varepsilon \propto \varepsilon^{n-1}$ and the number of excess contacts Z -Z_c, where Z_c is the number of contacts at the jamming transition (Mohan & Bonnecaze, 2012; O'Hern, Silbert, Liu, & Nagel, 2003; van Hecke, 2010): $G \propto k\left(Z - Z_c\right)$. The dimensionless overlap distance ε being small, the potential becomes softer when n increases and the elastic modulus is smaller. ε, k, Z, and G are power law functions of the distance to the jamming point (Lacasse et al., 1996; O'Hern et al., 2003):

$$\varepsilon = \varepsilon_0(\phi - \phi_c)\,, \tag{2.10a}$$

$$k = k_0(\phi - \phi_c)^{n-1}\,, \tag{2.10b}$$

$$Z - Z_c = Z_0(\phi - \phi_c)^{\zeta}\,, \tag{2.10c}$$

$$G = G_0(\phi - \phi_c)^{\gamma} \quad , \tag{2.10d}$$

where $\gamma = n+\zeta - 1$; ϕ_c is the jamming volume fraction; Z_c is the average contact number at the jamming point; ε_0, k_0, and Z_0 are prefactors. For monodisperse packing and in the asymptotic limit of large systems, the exponent ζ is equal to 1/2, $Z_c = 6$, and $\phi_c \cong 0.64$.

The elastic moduli shown in Figure 2.2 are well-fitted to Eq. 2.10d with $\gamma = 1$, 2.5, and 4.5, which are the values of γ expected for $n = 1.5$, 3, and 5 respectively. Letting the jamming point ϕ_c be a fitted parameter, we find that it consistently occurs at $\phi_c = 0.65 \pm 0.01$. Note that the value of ϕ_c is larger for polydisperse than for monodisperse suspensions. The details of the fitting parameters are presented in S2.2.

2.3.1.2 Structural properties of SPGs for different elastic force laws

Figures 3a-b show the variations of the contact number Z and the dimensionless average overlap distance ε versus the volume fraction for different values of the exponent n in equilibrated packings. Because the elastic repulsive forces are smaller for greater values of the exponent n, packing with greater n have larger average overlap distances for the same volume fraction. To compensate for larger overlap and still have the same volume fraction, they thus have fewer average contacts.

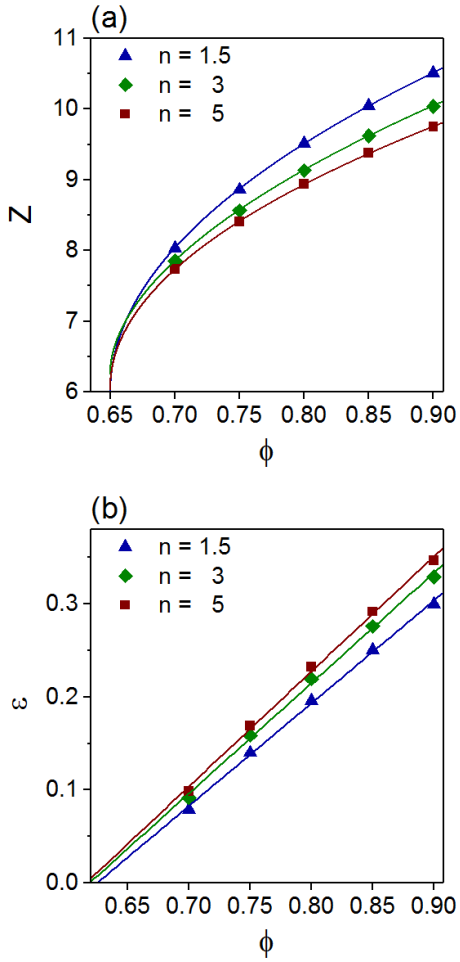

Figure 2.3: Variations of the average contact number Z (a) and overlap distance ε (b) for different values of exponent n. The solid lines in (a) are fits to Eq. 2.10c with $\phi_c = 0.65$ yielding: $Z_c = 6.0\pm0.1$, 6.3 ± 0.1, 6.0 ± 0.1 and $\zeta = 0.49\pm0.02$, 0.54 ± 0.02, 0.49 ± 0.02, for $n = 1.5$, 3, 5 respectively. The solid lines in (b) are fits to Eq. 2.10a yielding: $\phi_c = 0.63\pm0.01$ ($n = 1.5$); $\phi_c = 0.62\pm0.01$ ($n = 3$); $\phi_c = 0.62\pm0.01$ ($n = 5$).

In Figure 2.3a we have fitted the data to Eq. 2.10c assuming that jamming occurs at $\phi_c = 0.65$, the value which was determined from the shear modulus variations in Figure 2.2. The data are well represented by Eq. 2.10c. We find that the average number of contacts at ϕ_c is approximately six and the exponent ζ is close to 0.5, which are the values expected for monodisperse suspensions (Lacasse et al., 1996; O'Hern et al., 2003). The fitting parameters are given in S2.2. Finally, we have fitted the data for the average overlap distance in Figure 2.3b to the linear expression given by Eq. 2.10a. The

resulting values of ϕ_c are slightly different from those previously determined but both determinations remain within the interval of confidence which is admissible (see also S2.2).

2.3.2 The effect of the near-field drag force on the flow properties

In this section we investigate the effect of near-field contributions on the shear stress, first and normal stress differences. The elastic force law is has the generalized Hertz form in Eq. 2.2 and the far-field Stokes force is included in the simulations.

2.3.2.1 Elastohydrodynamic (EHD) drag force

Figures 4a-c show the results of the dimensionless shear stress σ, the first normal stress difference N_1 and the second normal stress difference N_2 versus the dimensionless shear rate at different volume fractions with and without EHD drag forces. All three quantities are well-fitted to Herschel-Bulkley equations over the entire range of shear rates investigated. It is also interesting to note that the first and second normal stress differences N_1 and N_2 are similar in magnitude and opposite in sign for the same volume fraction at the same shear rate. So-called film fluids, such as emulsions and foams, exhibit this property due to the storage of elastic energy in their interfaces (R. Larson, 1997). Here, the elastic energy is stored in the local deformations at contact. Interestingly, the results show little difference between the model with EHD drag forces and the one without EHD drag forces, which demonstrates the non-essential role of the near-field EHD drag forces in predicting shear stress and normal stress differences in the range of shear rates considered.

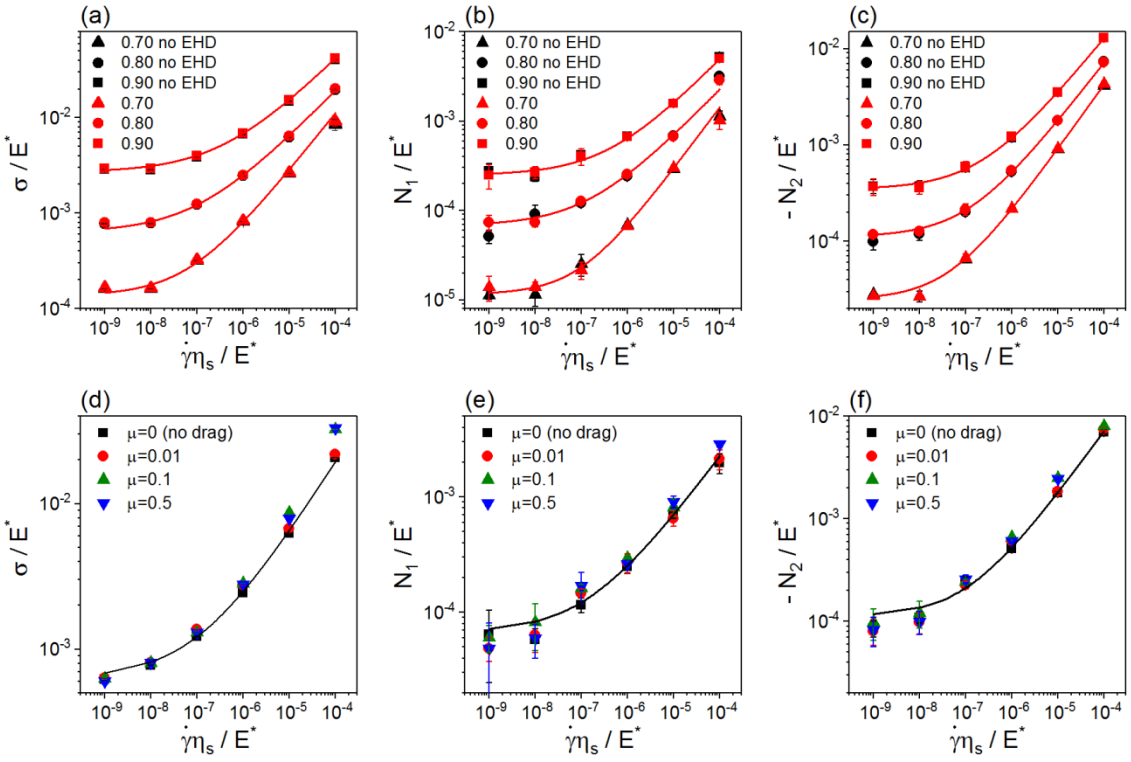

Figure 2.4: Top: role of the near-field elastohydrodynamic force; dimensionless shear stress (a), first normal stress difference (b) and second normal stress difference (c) versus dimensionless shear rate at ϕ = 0.70, 0.80 and 0.90 with EHD (red symbols) and without (black symbols). Bottom: role of Coulombic drag forces; dimensionless shear stress (d), first normal stress difference (e), and second normal stress difference (f) versus dimensionless shear rate at ϕ = 0.8 with coefficient μ = 0, 0.01, 0.1, 0.5. The results for ϕ = 0.70 and 0.90 also show negligible difference for different values of μ at ϕ = 0.80 and are not shown for clarity. Solid lines are fitted curves for simulations with no drag forces to the Herschel-Bulkley equations $\sigma / E^* = \sigma_y / E^* + k_\sigma(\dot{\gamma}\eta_S / E^*)^m$ and $N_i / E^* = N_{iy} / E^* + k_{Ni}(\dot{\gamma}\eta_S / E^*)^{mi}$ with parameters reported in SI (N_i refers to N_1 or $-N_2$).

2.3.2.2 Coulombic frictional drag force

Figures 2.4d-f show the results for the dimensionless shear stress and dimensionless normal stress differences versus the dimensionless shear rate at ϕ = 0.8 when Coulombic frictional drag forces with different friction coefficients μ are included in the simulations. Four cases are tested with μ set to be 0, 0.01, 0.1 or 0.5. The results show little difference among flow curves for all the friction coefficients. Similar to the

near-field EHD, Coulombic frictional drag forces play a negligible role in determining the shear stress versus shear rate flow curve.

2.3.3 The effect of the repulsive force law on the flow properties

In this section we investigate the effect of the repulsive force law on the shear stress, first and normal stress differences. The force law is given by Eq. 2.2 with $C = 1$ and $n = 1.5$, 3, and 5. Only the far-field Stokes force is included in the simulations; the near-field contributions being negligible from the previous section are not included.

2.3.3.3 Shear stress and first and second normal stress differences

The flow curves computed for exponents n =1.5, 3 and 5 at different volume fractions are shown in Figures 2.5a-c. At large shear rates and low values of the shear modulus, a microstructural transition could be observed, where the initially disordered suspension was evolving to a partially ordered structure with layers parallel to the flow-vorticity plane (Khabaz et al., 2017). Those corresponding shear stress data are not plotted in Figure 2.5. For the same volume fraction, shear stresses are larger for smaller n. Large shear stresses are generated for large overlap distances which occur for large volume fractions and small n.

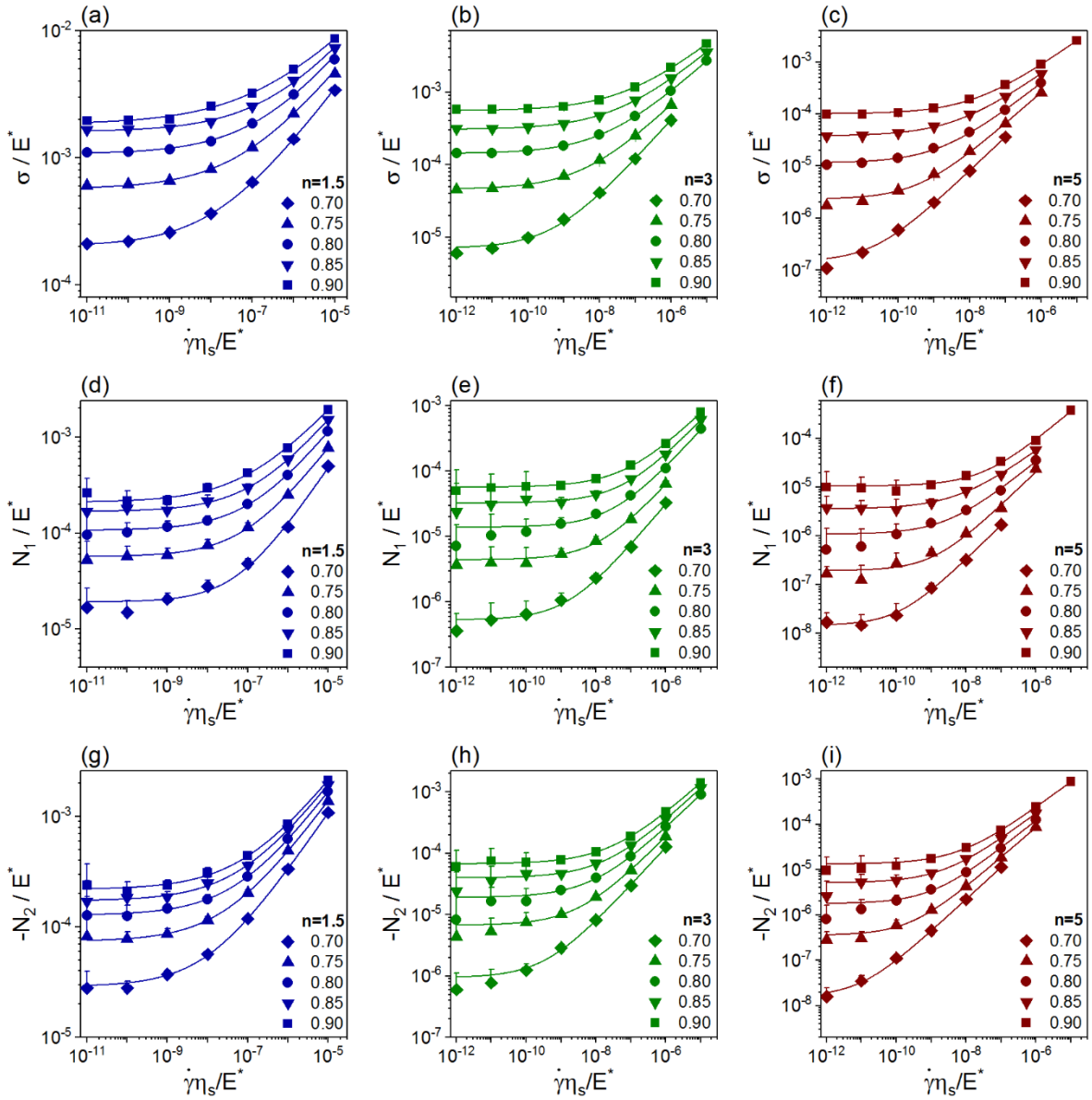

Figure 2.5: Dimensionless shear stress (a-c), dimensionless first (d-f) and second normal stress differences (g-i) versus dimensionless shear rate for different values of exponent n = 1.5, 3, 5. Solid lines are fitted curves to the Herschel-Bulkley equation. Only positive parts of error bars are shown for easier visualization. Data for all Herschel-Bulkley parameters are listed in S2.2.

The corresponding dimensionless first and second normal stress differences in Figures 2.5d-f and Figures 2.5g-i show the same trend as the shear stresses. They all exhibit a yield normal stress at small shear rates. Second normal stress differences N_2 are slightly larger in magnitude than N_1 and opposite in sign. The differences between

N_1 and N_2 are greater for lower volume fraction, higher shear rates and larger n. Microstructures and pair distribution functions for different n are also investigated which exhibit the same qualitative behavior as reported earlier (Mohan & Bonnecaze, 2012; Mohan, Pellet, et al., 2013; Seth et al., 2011).

Irrespective of the interparticle force law, the flow curves can be fitted to the canonical Herschel-Bulkley equation. The parameters m, σ_y and k as well as pair distribution functions are reported in S2.2. The exponent m lies in the range between 0.4 and 0.5 with weak dependencies on the volume fraction and the exponent of the force law. The exponent m decreases slightly when the volume fraction increases. This trend has also been noted in experiments (Pellet & Cloitre, 2016). The softness of the interaction has a small influence on the Herschel-Bulkley exponent, which has its smallest value for the Hertz law with n = 1.5 and is closer to 0.5 for n = 3 and 5. The same trends are observed for the first and second normal stress differences, although the Herschel-Bulkley exponents are slightly larger than for the stress and close to 0.5.

2.3.2.4 Scaling of shear stress and first and second normal stress differences

The shear stresses and normal stresses for each volume fraction and each elastic force law (n =1.5, 3 and 5) can be collapsed onto universal flow curves by scaling the stress with the yield stress and the shear rate with G/η_s, as shown in Figure 2.6. The collapse is satisfactory except for the shear stress data at volume fraction ϕ = 0.7 close to the jamming transition which fall slightly outside the master curve. These data were not included in the following fits. Each master curve can be described by an equation of the Herschel-Bulkley form:

$$\sigma/\sigma_y = 1 + \tilde{k}_\sigma \left(\dot{\gamma}\eta_s/G\right)^{\tilde{m}} \tag{2.11a}$$

$$N_1 / \sigma_y = \tilde{N}_{1y} + \tilde{k}_{N1} \left(\dot{\gamma} \eta_s / G \right)^{\tilde{m}_1} \tag{2.11b}$$

$$-N_2 / \sigma_y = -\tilde{N}_{2y} + \tilde{k}_{N2} \left(\dot{\gamma} \eta_s / G \right)^{\tilde{m}_2} \tag{2.11c}$$

The fitting parameters are tabulated in the supplement section S2.

For the shear stress, the exponent of the Herschel-Bulkley power law $\tilde{m}$ ranges from 0.41 to 0.50 as *n* increases from 1.5 to 5. For comparison the dotted lines in Figures 2.6a-c represent the best fit to experimental data obtained for microgel suspensions (Bonnecaze & Cloitre, 2010; Cloitre et al., 2003), yielding a Herschel-Bulkley exponent of 0.45. The fitted experimental data match the simulated universal flow curve reasonably well for *n* = 1.5 and 3. The agreement with experiments is not as good for *n* = 5, the simulated data being above the experimental lines at the larger shear rates. For the first and second normal stress differences, the Herschel-Bulkley exponents $\tilde{m}_1$ and $\tilde{m}_2$ range from 0.53 to 0.62 as *n* increases from 1.5 to 5. For each force law, the Herschel-Bulkley exponents are about the same for N_1 and N_2. We observed that the error bars at low shear rates are large because of the large fluctuations relative to N_{1y} and $N_{2y.}$ Finally, it is interesting to note that the yield normal stresses N_{1y} and N_{2y} are about an order of magnitude smaller than the yield shear stress.

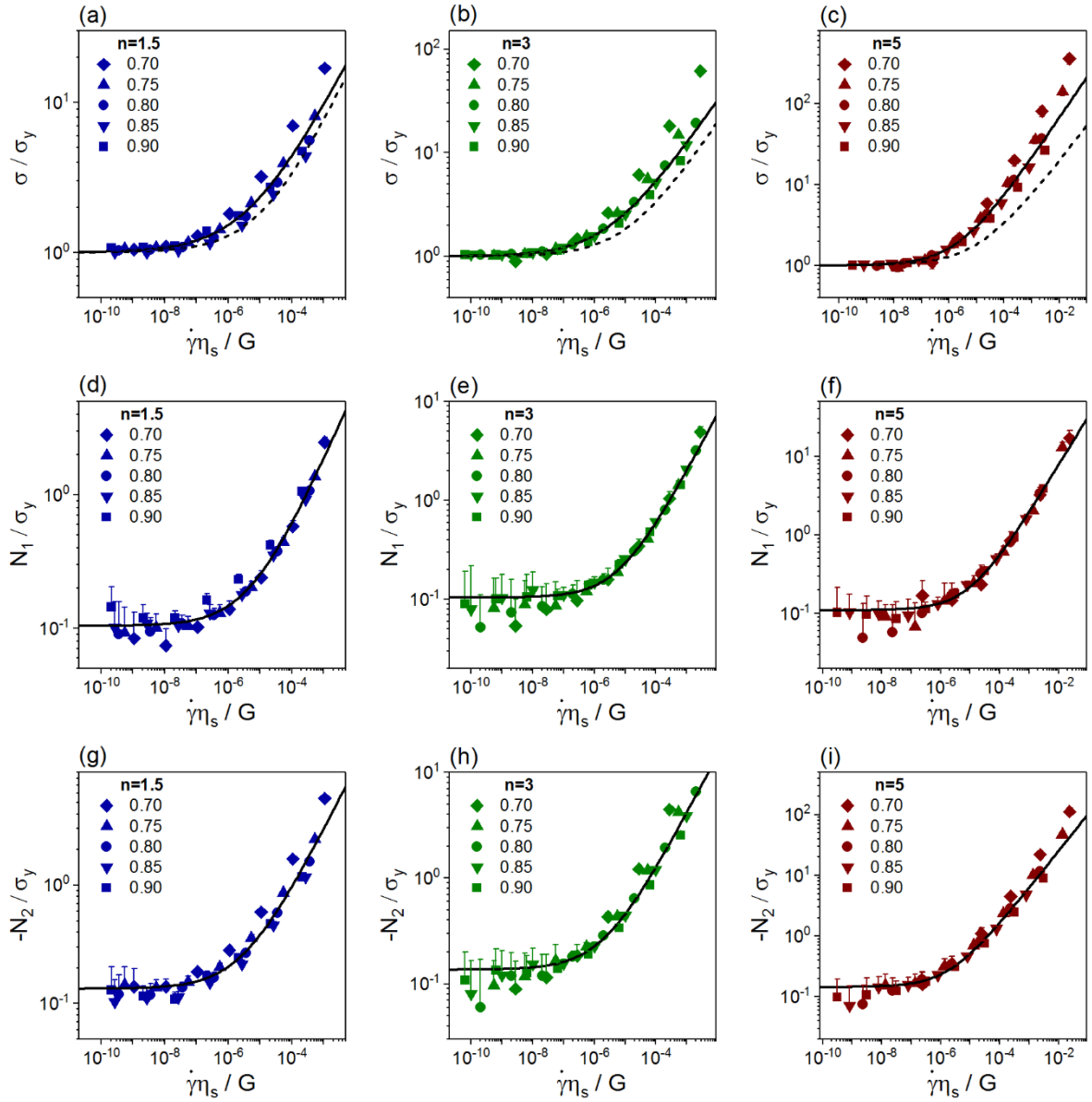

Figure 2.6: (a-c): Collapse of flow curves for elastic exponent n = 1.5, 3, and 5(c). The solid lines are the fitted Herschel–Bulkley curves; the dashed lines of equation $\sigma / \sigma_y = 1 + 150(\dot{\gamma}\eta_S / G)^{0.45}$ are fits to collapsed experimental data of microgels.(Cloitre et al., 2003; Pellet & Cloitre, 2016) (d-i): Collapse of first and second normal stress differences for n = 1.5, 3, 5. Only the upper halves of the error bars are shown for easier visualization. All Herschel-Bulkley parameters are listed in S2.2.

2.3.3 Discussion

Our results demonstrate that the elastohydrodynamic and Coulombic near-field drag are not important for predicting the rheology of SPGs. In our previous studies, we already observed that only the elastic contact forces contribute significantly to the shear and normal stresses for SPGs (Mohan, Pellet, et al., 2013; Seth et al., 2011). In those simulations, the near-field drag was included, which might influence the microstructure and so indirectly the rheology. The results presented in Figure 2.2 show that removing the near-field drag altogether has no substantial effect on the microstructure and the rheology. However, the result that the flow curves computed at different volume fractions or measured under different experimental conditions collapse when the shear rate is rescaled with $\dot{\gamma}\eta_S / G$ indicate that the viscous drag forces acting on the soft particles are important and that the shear rheology is clearly determined in part by the viscosity of the interstitial fluid (Bonnecaze & Cloitre, 2010; Cloitre et al., 2003; Seth et al., 2011). In the simulations, this effect is captured by the far-field drag force acting on the particles (Eq. 2.3).

As the relative velocities of particles increase at high shear rates, the near-field drag forces will likely become more important, because they may contribute a more significant amount to the force between the particles. This could increase the slope of the stress with the shear rate, and might be a partial explanation of the experimental results observed in a recent paper (Caggioni, Trappe, & Spicer, 2020). One can speculate particles that have fewer contacts, which means fewer restrictions for rearrangements from neighboring particles, might be more sensitive to the near-field elastohydrodynamics at high shear rates. Thus configurations with lower volume fractions close to the jamming point are more probable to show the impact.

It is noteworthy that the dimensionless shear rate $\dot{\gamma}\eta_S / G$ is effective in collapsing the shear stress and normal stress differences for different volume fractions for all the pairwise potentials considered in this study. Previously, this dimensionless shear rate has been used to successfully create master flow curves from experimental data on systems as different as microgels, concentrated emulsions, and star polymers (Bonnecaze & Cloitre, 2010; Cloitre et al., 2003; Erwin, Cloitre, Gauthier, & Vlassopoulos, 2010). The dimensionless shear rate $\dot{\gamma}\eta_S / G$ is the ratio of the time scale $1/\dot{\gamma}$ associated with the shear deformation, to the characteristic time η_S / G, which expresses the competition between the cage elasticity and the viscous forces acting on the particles when they rearrange. The volume fraction dependence of the characteristic time η_S / G is embodied in the shear modulus. The dimensionless shear rate $\dot{\gamma}\eta_S / G$ controls several other important dynamical phenomena in SPGs. First, the shear-induced crystallization of monodispersed SPGs or layering of polydisperse SPGs at different volume fractions occurs at some critical value of $\dot{\gamma}\eta_S / G$ (Khabaz et al., 2018; Khabaz et al., 2017). In another context, the initial short-time relaxation of the stress upon flow cessation is driven by a characteristic time which involves the dissipation time η_s / E^* and the dimensionless shear rate $\dot{\gamma}\eta_S / G$ applied during the initial flow (Mohan, Cloitre, & Bonnecaze, 2015). The resulting residual stresses trapped into SPGs are also controlled by $\dot{\gamma}\eta_S / G$ (Mohan, Bonnecaze, et al., 2013; Mohan et al., 2015). This scaling highlights the importance of the competition between viscous and elastic forces in sheared SPGs.

When the elastic repulsion between the particles obeys to the Hertz potential (C = 1 and n = 1.5 in Eq. 2.2), there exists an alternative non-dimensionalization of the

shear rate which collapses the flow curves onto master curves. Indeed in Figure 2.5a, the flow curves are of the form $\sigma / E^* = \sigma_y / E^* + k_\sigma \left(\dot{\gamma} \eta_s / E^* \right)^m$ and the prefactors k_σ are found proportional to G / E^* (see S2.2). Moreover, the yield stress and the elastic modulus are related through $\sigma_y = G \gamma_y$, where γ_y is the yield strain. The same reasoning holds for the first and second normal stress differences. It follows that the shear stress and normal stress differences at different volume fractions must be correlated using the equations:

$$\sigma / \sigma_y = 1 + \bar{k}_\sigma \left(\dot{\gamma} \eta_s / \gamma_y^2 E^* \right)^{\bar{m}} \tag{2.12a}$$

$$N_1 / \sigma_y = \bar{N}_{1y} + \bar{k}_{N1} \left(\dot{\gamma} \eta_s / \gamma_y^2 E^* \right)^{\bar{m}_1} \tag{2.12b}$$

$$-N_2 / \sigma_y = -\bar{N}_{2y} + \bar{k}_{N2} \left(\dot{\gamma} \eta_s / \gamma_y^2 E^* \right)^{\bar{m}_2} \tag{2.12c}$$

Figure 2.7 shows the normalized shear and normal stresses at different volume fractions on a master curve as a function of the dimensionless shear rate $\dot{\gamma} \eta_s / \gamma_y^2 E^*$. The new fitting parameters are listed in the SI. Now, the yield strain embodies the volume fraction dependence of the rescaled shear rate enabling a master flow curve. While this alternative rescaling works well for n = 1.5, it fails for n = 3 or 5 because for these potentials, the consistency parameters in the Herschel-Bulkley equations for the stress and normal stress differences do not vary linearly with G / E^*. It is interesting to note that the non-dimensional parameters used in Eqs. 2.11 and 2.12 simply differ by the ratio G / γ_y^2, which is found constant in our simulations. This follows from the scaling of G and σ_y with $\phi - \phi_c$. As noted in section 2.3.1.1, $G \sim (\phi - \phi_c)^{n-1/2}$; in addition the yield stress varies like $\sigma_y \sim (\phi - \phi_c)^n$ (see Figure 2.9 in S2.3), which has also been noted by others (Dinkgreve, Paredes, Michels, & Bonn, 2015; Peter Olsson & Teitel, 2011).

It follows that $\gamma_y \sim (\phi - \phi_c)^{1/2}$ and $G/\gamma_y^2 \sim (\phi - \phi_c)^{n-3/2}$. Clearly, for n = 1.5, G/γ_y^2 is a constant independent of volume fraction, but not so for other values of n. This alternative non-dimensionalization of the shear rate was noted earlier by Seth *et al.* (Seth et al., 2011) in simulations using the generalized Hertz potential given by Eq. 2.2 with varying C and n depending on the overlap of the particles (Seth et al., 2011), and in experiments (Pellet & Cloitre, 2016; Seth et al., 2011). The fact that it worked for this modified potential strongly indicates that the pairwise interactions with the modified potentials and in the experiments are close to that of the classic Hertz potential with n = 1.5.

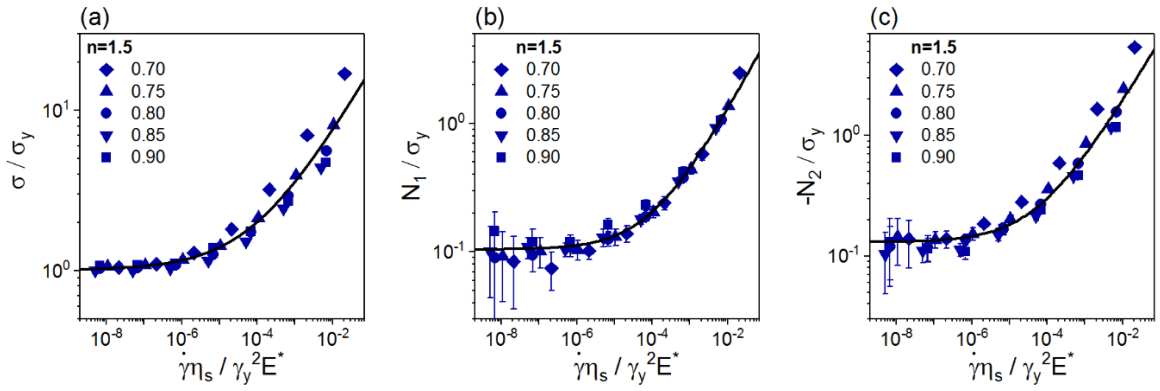

Figure 2.7: Collapse of all shear stresses and normal stress differences with $\dot{\gamma}\eta_s / \gamma_y^2 E^*$ for n = 1.5. The solid lines are Herschel–Bulkley fits to the data. The fitting parameters are listed in the SI.

Another question of interest concerns the value of the Herschel-Bulkley exponents, which for the shear stress and normal stress differences are close to 0.5. However a close examination of the results indicates a systematic variation that signals some effect of the potential. Indeed in Figure 2.6 the Herschel-Bulley exponents for the collapsed shear stress data are 0.41, 0.43, and 0.51 for n = 1.5, 3 and 5, respectively. A similar increase of the exponents with n is observed for the first and second normal stress differences. The variations are outside the confidence intervals showing that stiffer potentials yield slightly larger Herschel-Bulkley exponents. This trend is

supported by the fact that simulations using the generalized Hertz law, which progressively becomes stiffer as the particle compression is increased, yield exponents equal to 0.50 instead of 0.41 for the simple Hertz law (Seth et al., 2011). In experiments, the slight dependence of the exponent on the potential may explain the difference between concentrated emulsions (Bonnecaze & Cloitre, 2010; Seth et al., 2011) (m = 0.50) and microgel suspensions (Cloitre et al., 2003) (m = 0.45). It has been proposed that the physical origin of this non trivial value is associated to non-affine deformations that occur through individual rearrangements localized in time and space. In elastoplastic models the dynamics of long-ranged stress and strain fluctuations in the surrounding of a localized yielding event is accounted for by a Fokker-Planck equation which predicts exponents in the range of 0.50-0.59 (Agoritsas & Martens, 2017; Bocquet et al., 2009; Lin & Wyart, 2018). In this context, our results suggest that avalanches and cascade rearrangements can be affected by the exact shape of the elastic potential.

2.4 CONCLUSIONS

A computational study has been performed to show the universal form of the flow curve for soft particle glasses with different pairwise elastic and frictional forces. It is found that pairwise or near-field viscous and Coulombic sliding forces play no significant role in terms of the macroscopic rheology of these materials. The rheology is dominated by the elastic forces acting normally between the particles. For a given pairwise elastic interaction potential, the variations of the shear and normal stresses can be collapsed for all volume fractions by rescaling the stress by the yield stress and the shear rate by the characteristic time η_s / G, the ratio of the suspending viscosity and low frequency shear modulus. The exponent for the Herschel-Bulkley fits for these flow

curves ranges from about 0.4 to 0.6 and increases with the exponent of the elastic interaction. For a given elastic potential, there is a universal representation of the flow curves for SPGs for all volume fractions.

SUPPLEMENTAL S2.1 PAIR DISTRIBUTION FUNCTION FOR SUSPENSION FOR DIFFERENT FORCE LAWS.

The pair distribution function for suspensions with different pairwise elastic force laws have different maximum values, as noted in Figure 2.8.

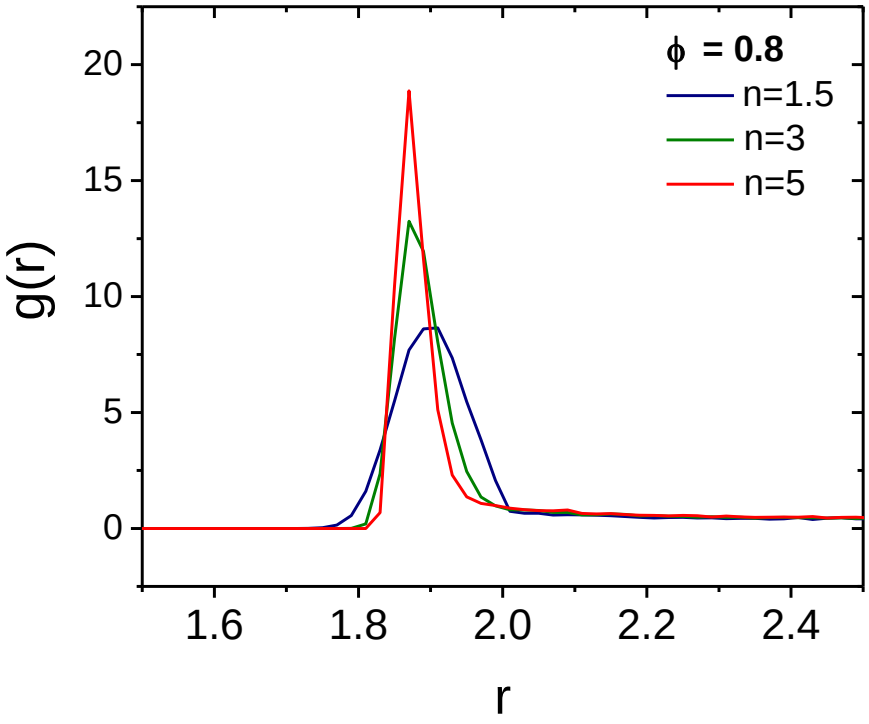

Figure 2.8: Pairwise particle distribution at rest for volume fraction = 0.8

SUPPLEMENTAL S2.2 FITTING PARAMETERS FOR CURVES IN FIGURES 2.2-2.6.

Tables 2.1-2.8 list the fitting parameters used for the curves in Figures 2.2-2.6 of the paper. Standard deviations are given inside parentheses following each data point. All the data shown in Table 2.1, 2.5-2.7 are based on the following dimensionless equations:

$$\sigma/E^* = \sigma_y/E^* + k_\sigma\left(\dot{\gamma}\eta_s/E^*\right)^m, \tag{2.13}$$

$$N_1/E^* = N_{1y}/E^* + k_{N1}\left(\dot{\gamma}\eta_s/E^*\right)^{m_1}, \tag{2.14}$$

$$-N_2/E^* = -N_{2y}/E^* + k_{N2}\left(\dot{\gamma}\eta_s/E^*\right)^{m_2}. \tag{2.15}$$

Table 2.1: Fitting parameters for curves in Figure 2.2.

Volume Fraction	σ_y	k_σ	m
0.70	1.36×10^{-4} (1.59×10^{-5})	2.93 (2.52)	0.606 (0.065)
0.80	6.29×10^{-4} (4.59×10^{-5})	1.86 (0.79)	0.500 (0.032)
0.90	2.69×10^{-3} (9.61×10^{-5})	3.51 (0.71)	0.488 (0.015)
Volume Fraction	N_{1y}	k_{N1}	m_1
0.70	1.15×10^{-5} (2.00×10^{-6})	0.838 (0.354)	0.693 (0.036)
0.80	6.76×10^{-5} (1.29×10^{-5})	0.301 (0.186)	0.535 (0.053)
0.90	2.49×10^{-4} (2.14×10^{-5})	0.666 (0.117)	0.538 (0.017)
Volume Fraction	N_{2y}	k_{N2}	m_2
0.70	2.49×10^{-5} (1.18×10^{-6})	1.98 (0.33)	0.669 (0.013)
0.80	1.11×10^{-4} (6.59×10^{-6})	2.02 (0.24)	0.615 (0.011)
0.90	3.48×10^{-4} (3.06×10^{-5})	2.77 (0.39)	0.587 (0.013)

(The fitting parameters are similar for simulations with and without near-field draft forces.)

Table 2.2: Parameters for static properties in Figures 2.3 and 2.4.

n	Parameters	Volume fraction				
		0.70	0.75	0.80	0.85	0.90
1.5	ε	0.079	0.140	0.196	0.251	0.300
	Z	8.04	8.86	9.51	10.04	10.51
	G	9.22×10^{-3} (0.00149)	1.85×10^{-2} (0.00258)	2.79×10^{-2} (0.00224)	3.71×10^{-2} (0.00403)	4.72×10^{-2} (0.00356)
3	ε	0.091	0.159	0.219	0.276	0.329
	Z	7.85	8.57	9.13	9.62	10.04
	G	3.63×10^{-4} (6.09×10^{-5})	1.82×10^{-3} (2.87×10^{-4})	4.95×10^{-3} (4.41×10^{-4})	1.00×10^{-2} (1.13×10^{-3})	1.56×10^{-2} (2.23×10^{-3})
5	ε	0.099	0.169	0.232	0.292	0.346
	Z	7.73	8.41	8.94	9.38	9.75
	G	4.21×10^{-6} (8.98×10^{-7})	7.48×10^{-5} (1.77×10^{-5})	4.28×10^{-4} (8.83×10^{-5})	1.26×10^{-3} (1.74×10^{-4})	3.25×10^{-3} (4.17×10^{-4})

Table 2.3: Fitting parameters for low-frequency modulus in Figure 2.3.

n	G_0	ϕ_c	γ (fixed to *n*-0.5)
1.5	0.188 (0.001)	0.651 (0.001)	1.0
3	0.508 (0.021)	0.645 (0.001)	2.5
5	1.460 (0.090)	0.641 (0.002)	4.5

Note: $G = G_0\left(\phi - \phi_c\right)^\gamma$

Table 2.4: Fitting parameters in Figure 2.4

n	Figure 2.4a			Figure 2.4b	
	Z_c	Z_0	ζ	ε_0	ϕ_c
1.5	6.0 (0.1)	8.96 (0.03)	0.49 (0.02)	1.24 (0.03)	0.63 (0.01)
3	6.3 (0.1)	7.98 (0.04)	0.54 (0.02)	1.19 (0.03)	0.62 (0.01)
5	6.0 (0.1)	7.32 (0.04)	0.49 (0.02)	1.10 (0.02)	0.62 (0.01)

Note: $Z - Z_c = Z_0 \left(\phi - \phi_c\right)^{\zeta}$ with ϕ_c fixed to 0.65; $\varepsilon = \varepsilon_0(\phi - \phi_c)$ with ϕ_c not fixed.

Table 2.5: Fitting parameters for shear stress in Figure 2.5.

n	Volume Fraction	σ_y	k_σ	m
1.5	0.70	2.01×10^{-4} (1.6×10^{-6})	0.517 (0.042)	0.438 (0.005)
	0.75	5.69×10^{-4} (6.0×10^{-6})	0.499 (0.055)	0.413 (0.008)
	0.80	1.07×10^{-3} (7.8×10^{-6})	0.637 (0.097)	0.415 (0.011)
	0.85	1.66×10^{-3} (3.5×10^{-5})	0.571 (0.102)	0.398 (0.014)
	0.90	1.83×10^{-3} (4.5×10^{-5})	0.344 (0.086)	0.341 (0.018)
3	0.70	6.71×10^{-6} (3.7×10^{-7})	0.475 (0.073)	0.517 (0.009)
	0.75	4.51×10^{-5} (7.8×10^{-7})	0.349 (0.031)	0.461 (0.006)
	0.80	1.39×10^{-4} (7.0×10^{-7})	0.404 (0.017)	0.441 (0.003)
	0.85	3.00×10^{-4} (1.7×10^{-6})	0.436 (0.016)	0.424 (0.003)
	0.90	5.56×10^{-4} (7.5×10^{-6})	0.504 (0.046)	0.417 (0.006)
5	0.70	1.00×10^{-7} (1.5×10^{-8})	1.015 (0.15)	0.637 (0.007)
	0.75	1.84×10^{-6} (2.0×10^{-7})	0.469 (0.087)	0.551 (0.011)
	0.80	1.06×10^{-5} (2.2×10^{-7})	0.350 (0.054)	0.500 (0.009)
	0.85	3.65×10^{-5} (5.3×10^{-7})	0.394 (0.051)	0.476 (0.008)
	0.90	9.73×10^{-5} (1.1×10^{-6})	0.531 (0.044)	0.470 (0.005)

Table 2.6: Fitting parameters for first normal stress difference N_1 in Figure 2.5.

n	Volume Fraction	N_{1y}	k_{N1}	m_1
1.5	0.70	1.91×10^{-5} (2.0×10^{-6})	0.650 (0.335)	0.629 (0.041)
	0.75	5.70×10^{-5} (2.0×10^{-6})	0.424 (0.061)	0.554 (0.012)
	0.80	1.07×10^{-4} (3.5×10^{-6})	0.456 (0.059)	0.529 (0.011)
	0.85	1.68×10^{-4} (4.3×10^{-6})	0.487 (0.061)	0.511 (0.010)
	0.90	2.10×10^{-4} (1.4×10^{-5})	0.359 (0.102)	0.464 (0.024)
3	0.70	5.95×10^{-7} (9.9×10^{-8})	0.232 (0.101)	0.645 (0.029)
	0.75	4.42×10^{-6} (3.2×10^{-7})	0.260 (0.091)	0.607 (0.025)
	0.80	1.39×10^{-5} (1.7×10^{-6})	0.402 (0.132)	0.596 (0.026)
	0.85	3.26×10^{-5} (1.6×10^{-6})	0.419 (0.065)	0.572 (0.013)
	0.90	5.70×10^{-5} (1.9×10^{-6})	0.342 (0.048)	0.534 (0.011)
5	0.70	1.45×10^{-8} (2.1×10^{-9})	0.147 (0.072)	0.707 (0.027)
	0.75	1.93×10^{-7} (5.2×10^{-8})	0.304 (0.245)	0.694 (0.051)
	0.80	1.08×10^{-6} (2.5×10^{-7})	0.113 (0.072)	0.589 (0.042)
	0.85	3.60×10^{-6} (3.1×10^{-7})	0.090 (0.029)	0.537 (0.022)
	0.90	1.06×10^{-5} (1.2×10^{-6})	0.408 (0.125)	0.611 (0.024)

Table 2.7: Fitting parameters for second normal stress difference N_2 in Figure 2.5.

n	Volume Fraction	$-N_{2y}$	k_{N2}	m_2
1.5	0.70	2.88×10^{-5} (1.1×10^{-6})	0.487 (0.042)	0.533 (0.007)
	0.75	7.40×10^{-5} (9.1×10^{-7})	0.421 (0.014)	0.501 (0.003)
	0.80	1.28×10^{-4} (2.0×10^{-6})	0.466 (0.020)	0.496 (0.004)
	0.85	1.79×10^{-4} (4.9×10^{-6})	0.481 (0.051)	0.487 (0.009)
	0.90	2.19×10^{-4} (8.6×10^{-6})	0.422 (0.054)	0.469 (0.011)
3	0.70	9.35×10^{-7} (1.8×10^{-7})	0.661 (0.121)	0.621 (0.012)
	0.75	6.68×10^{-6} (5.6×10^{-7})	0.577 (0.118)	0.584 (0.014)
	0.80	1.90×10^{-5} (1.1×10^{-6})	0.508 (0.038)	0.551 (0.006)
	0.85	3.96×10^{-5} (1.5×10^{-6})	0.557 (0.048)	0.539 (0.007)
	0.90	6.70×10^{-5} (1.2×10^{-6})	0.527 (0.022)	0.518 (0.004)
5	0.70	1.60×10^{-8} (3.0×10^{-9})	0.990 (0.093)	0.710 (0.005)
	0.75	3.55×10^{-7} (5.6×10^{-8})	0.821 (0.125)	0.664 (0.010)
	0.80	1.77×10^{-6} (2.8×10^{-7})	0.635 (0.139)	0.620 (0.015)
	0.85	5.08×10^{-6} (5.6×10^{-7})	0.511 (0.103)	0.580 (0.014)
	0.90	1.33×10^{-5} (6.4×10^{-7})	0.620 (0.049)	0.572 (0.006)

Table 2.8: Fitting parameters in Figure 2.6**.**

n		$\tilde{k}_\sigma$	m
1.5		145.7 (37.2)	0.407 (0.025)
3		224.9 (19.8)	0.428 (0.009)
5		692.3 (77.8)	0.505 (0.012)
n	$\tilde{N}_{1y}$	$\tilde{k}_{N1}$	$\tilde{m}_1$
1.5	0.104 (0.007)	72.5 (15.2)	0.537 (0.025)
3	0.104 (0.005)	112.4 (12.0)	0.588 (0.014)
5	0.110 (0.007)	132.2 (15.5)	0.616 (0.016)
n	$-\tilde{N}_{2y}$	$\tilde{k}_{N2}$	$\tilde{m}_2$
1.5	0.133 (0.023)	112.9 (49.8)	0.532 (0.053)
3	0.136 (0.027)	181.0 (45.6)	0.550 (0.033)
5	0.144 (0.026)	420.2 (75.2)	0.611 (0.023)

Note: $\sigma / \sigma_y = 1 + \tilde{k}_\sigma \left(\dot{\gamma} \eta_s / G_0 \right)^m$

$N_1 / \sigma_y = \tilde{N}_{1y} + \tilde{k}_{N1} \left(\dot{\gamma} \eta_s / G_0 \right)^{\tilde{m}_1}$; $-N_2 / \sigma_y = -\tilde{N}_{2y} + \tilde{k}_{N2} \left(\dot{\gamma} \eta_s / G_0 \right)^{\tilde{m}_2}$

Table 2.9: Fitting parameters in Figure 2.7.

	$\bar{k}_\sigma$	$\bar{m}$
	42.6 (7.9)	0.405 (0.025)
$\bar{N}_{1y}$	$\bar{k}_{N1}$	$\bar{m}_1$
0.104 (0.005)	14.7 (1.4)	0.540 (0.018)
$-\bar{N}_{2y}$	$\bar{k}_{N2}$	$\bar{m}_2$
0.130 (0.026)	20.1 (6.3)	0.517 (0.058)

(Note: $\sigma / \sigma_y = 1 + \bar{k}_\sigma \left(\dot{\gamma} \eta_s / \gamma_y^2 E^* \right)^{\bar{m}}$

$N_1 / \sigma_y = \bar{N}_{1y} + \bar{k}_{N1} \left(\dot{\gamma} \eta_s / \gamma_y^2 E^* \right)^{\bar{m}_1}$; $-N_2 / \sigma_y = -\bar{N}_{2y} + \bar{k}_{N2} \left(\dot{\gamma} \eta_s / \gamma_y^2 E^* \right)^{\bar{m}_2}$)

SUPPLEMENTAL S2.3 SCALING OF YIELD STRESS WITH DISTANCE TO JAMMING.

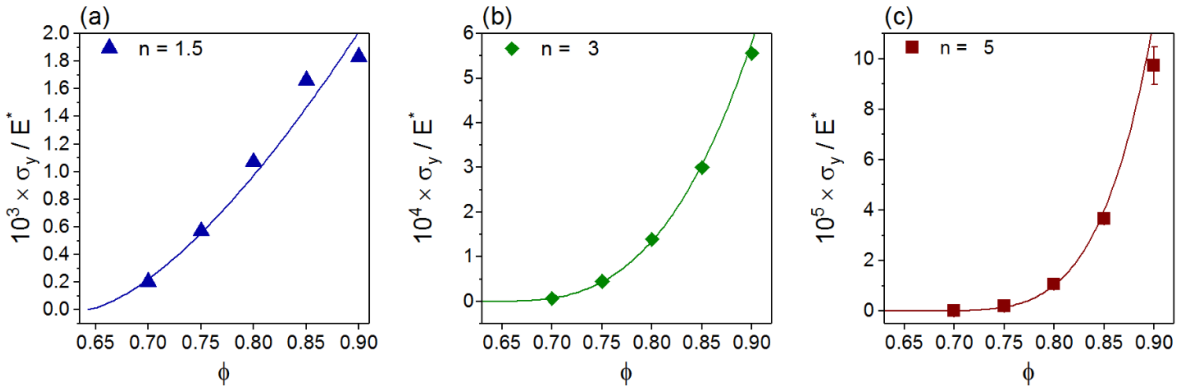

Figure 2.9: Scaling of yield stress with volume fraction. ϕ_c is assumed to be 0.64. The fitted curves are: (a) $\sigma_y / E^* = 0.0152 \left(\phi - \phi_c \right)^{1.5}$; (b) $\sigma_y / E^* = 0.0331 \left(\phi - \phi_c \right)^3$; (c) $\sigma_y / E^* = 0.0980 \left(\phi - \phi_c \right)^5$.

Chapter 3: Behavior of storage and loss moduli of jammed soft particles at high frequency

3.1 INTRODUCTION

Jammed soft particles are concentrated suspensions of soft, squishy particles with volume fractions beyond the random close packing limit of hard spherical particles. Common examples of jammed soft particles include solid inks, mayonnaise, yogurt, toothpaste, shampoo, and coating materials. They are viscoelastic yield-stress fluids, exhibiting both solid- and fluid-like properties depending on the amplitude and rate of external stimuli. The glassy state of these materials is athermal and the elastic contact forces are much larger than Brownian forces. With inertia being negligible, the system under shear can be modeled as a dynamic equilibrium of counterbalance between repulsive elastic forces and dissipative viscous forces. It has been shown that the two forces are essential to successfully capture major rheological behavior (T. Liu et al., 2018). The low-frequency limit G_0 of storage modulus G' is an important characteristic property of these materials and often encompasses the volume fraction dependency in non-dimensionalizations. In previous simulation and experimental research, G_0 has been used very effectively for collapsing rheological data like shear stress and normal stress difference of different systems onto universal curves (Cloitre et al., 2003; T. Liu et al., 2018). For the viscous force side of the system, loss modulus G'' is also important in understanding the relaxation of the material.

Storage and loss moduli can be measured by imposing small amplitude oscillatory shear (SAOS), which explores the linear viscoelastic regime of the material. When the applied deformation is small, the structure of the material is not too disturbed and the resulting shear stress is proportional to the amplitude of the applied strain. Pellet et al. (Pellet & Cloitre, 2016) showed the gradual change of storage and loss modulus during glass and jamming transitions for microgel suspensions using frequency sweep tests. They showed that as the effective volume fraction increases, the loss tangent G''/G' decreases, indicating the system is becoming more solid-like. In the jammed state, the storage modulus is much greater than the loss

modulus, and it is constant for low values of the frequency. This plateau value increases with concentration. The loss modulus seems to have a power-law increase with frequency, except at a very low frequency where the rheometers are not able to measure accurately. Experiments on water-in-oil emulsions (Shu et al., 2013) have observed similar results. Besides SAOS, researchers use large amplitude oscillatory shear (LAOS) (Hyun et al., 2011; Pellet & Cloitre, 2016; Shu et al., 2013) to probe the nonlinear viscoelastic behavior after yielding and measured the frequency dependence of *G'* and *G"*. In this paper, our focus is on SAOS.

Previous researchers have proposed several theoretical models to predict the frequency-dependent behavior of modulus. Zwanzig and Mountain proposed a classic equation to calculate the high-frequency limit of the elastic modulus for any isotropic material with particles interacting by pairwise two-body central forces (Zwanzig & Mountain, 1965). Lionberger and Russel have shown that elastic modulus of hard-sphere colloids without hydrodynamic interaction produces a power law of ½ with respect to frequency when approaching the high limit, without having a well-defined plateau as the Zwanzig and Mountain's model does (Lionberger & Russel, 1994). Liu et al. proposed a model assuming slip occurring in a local region during shear, causing the deformation to be non-affine and deducing complex dynamic shear modulus varying as a power law of ½ with frequency (A. J. Liu, Ramaswamy, Mason, Gang, & Weitz, 1996).

Conventional rheometers can only measure up to about 100 Hz. It's always been a challenge to measure the high-frequency SAOS rheology of complex fluids where classic time-temperature superposition doesn't apply (Plazek, 1996). A lot of efforts have been made to come up with new experimental methods to explore the high-frequency realm. An early successful method using dynamic light scattering was presented by Mason and Weitz (Mason & Weitz, 1995). The method could probe over a large frequency range by relating storage and loss moduli with the mean square displacement of a probe particle. Fritz et al. later proposed a new way using torsional resonators which can measure the linear viscoelastic behavior up to kilohertz range (Fritz, Pechhold, Willenbacher, & Wagner, 2003). A recent study by Nthanasiou et al. improved piezo-operated sliding-plate rheometry and managed to measure

frequencies as high as 1000Hz (Athanasiou, Auernhammer, Vlassopoulos, & Petekidis, 2019). They validated their result by comparing with the time-temperature data with emphasis on sensitive loss angle. These experiments didn't investigate jammed soft particle suspensions studied in this paper.

With all the previous efforts, there are still several open questions to be answered in this field. Although the formula by Zwanzig and Mountain offered a way to calculate the high-frequency limit of storage moduli G_∞, no current theory is available to estimate G_0, which is an important characteristic property for the jammed system as introduced earlier. The natural question following this would be, how does the system transition gradually from G_0 to G_∞ frequency increases? Our previous work has found that near-field viscous forces like elastohydrodynamic forces have a minimal role in capturing the major rheological behavior during steady shear (T. Liu et al., 2018). Will this be a similar situation here about the storage and loss moduli?

In this work, we try to tackle these questions by presenting our work in the following manner. First, the simulation method, pairwise forces, and data analysis method are introduced in detail. After that, results along with discussion are listed where storage and loss moduli results are given in two separate sections, followed by a third section comparing these results with experiments.

3.2 METHODS

3.2.1 Simulation method

Soft particle glasses are modeled as monodisperse elastic spheres with Young's modulus E, dispersed in a solvent of viscosity η_S, at a volume fraction ϕ higher than the random close packing of hard spheres as shown in Figure 3.1a. The jammed suspension is subject to a sinusoidal oscillatory shear strain of amplitude γ_0 and frequency ω. The strain changes with time as $\gamma = \gamma_0 \sin(\omega t)$. The maximum strain γ_0 used is 0.001, smaller than the yield strain of the suspensions, which is in the range of 0.018 to 0.045 for the cases below (T. Liu et al., 2018;

Seth et al., 2011). Before the oscillatory shear, the particles in the suspension are equilibrated using the conjugate gradient method so that they are force-free (T. Liu et al., 2018). The dynamics of the system evolve under shear and interparticle forces between particle and particle β as depicted in Figure 3.1b. The interparticle forces are pairwise repulsive elastic forces $\mathbf{f}_{\alpha\beta}^{\text{elas}}$ and pairwise viscous dissipative drag forces $\mathbf{f}_{\alpha\beta}^{\text{drag}}$. Note that, in the jamming regime, the local elastic forces that trap the particles hinder their rotation, which accordingly is not considered in the simulations (Dagallier et al., 2012).

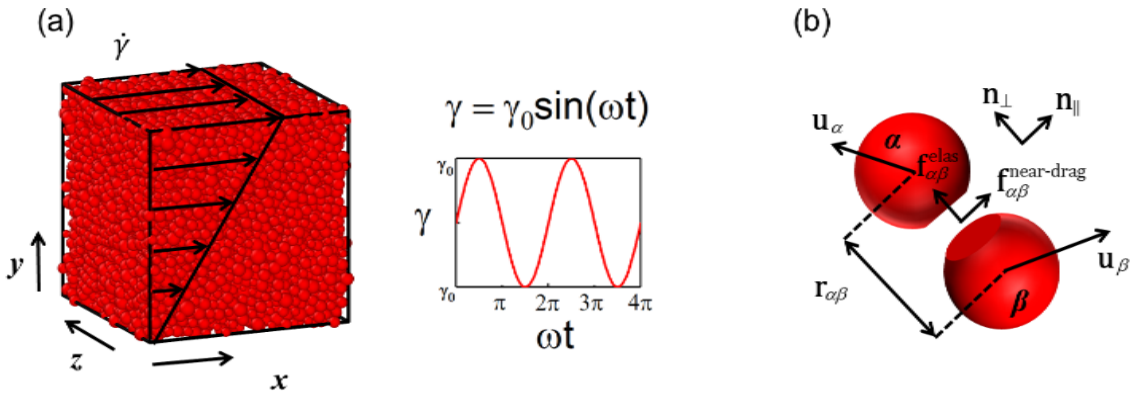

Figure 3.1: Schematic representation of a sheared suspension (a) and pairwise interaction (b).

The elastic forces take the form of

$$\mathbf{f}_{\alpha\beta}^{\text{elas}} = \frac{4}{3} E^* \varepsilon_{\alpha\beta}^n R_c^2 \mathbf{n}_\perp, \tag{3.1}$$

where $E^* = E/2(1-\nu^2)$ is the contact modulus based on the Young modulus E and Poisson ratio ν, $R_c = R_\alpha R_\beta / (R_\alpha + R_\beta)$ is the contact radius, $\varepsilon_{\alpha\beta} = \left(R_\alpha + R_\beta - r_{\alpha\beta}\right)/R_c$ is the dimensionless overlap distance characterizing the degree of compression, and $\mathbf{n}_\perp$ is the unit vector perpendicular to the flat surface representing the particle-particle contact. The values of n are 1.5, 3, and 5. Essentially, every continuous elastic force law can be approximated as a function of the overlap distance by a series addition of polynomials of different power. When n = 1.5, the equation is the same as simple Hertz law. Besides, n = 3 and 5 are explored to investigate the impact of n. The three numbers chosen here are examples to show the universal behavior for these materials regardless of the specific form of elastic force law.

The drag forces $\mathbf{f}_{\alpha\beta}^{\text{drag}}$ consist of both far-field drag forces and near-field drag forces. Far-field drag forces denote the hindered Stokes drag originating from the different velocities between particle α and ambient flow. Our earlier paper (T. Liu et al., 2018) showed that near-field drag forces are not important in computing shear stresses and normal stress differences under simple shear. The influence of near-field drag forces in calculating loss and storage modulus is evaluated. Two forms of near-field drag forces are studied, including elastohydrodynamic force $\mathbf{f}_{\alpha\beta}^{\text{EHD}}$ (T. Liu et al., 2018; Seth et al., 2011) as in Eq. 3.2 and a simple drag force $\mathbf{f}_{\alpha\beta}^{\text{r}}$ proportional to the power *p* of the relative velocity of contacting particles as in Eq. 3.3. Parameters E^*, R_c, and $\varepsilon_{\alpha\beta}$ are as defined in Eq. 3.1. The two near-field drag forces are computed using the difference between the center of mass velocities $\mathbf{u}_{\alpha\beta}$.

The equation of $\mathbf{f}_{\alpha\beta}^{\text{EHD}}$ is given as

$$\mathbf{f}_{\alpha\beta}^{\text{EHD}} = -\left(\eta_S C u_{\alpha\beta,\parallel} E^* R_c^3\right)^{1/2} \varepsilon_{\alpha\beta}^{(2n+1)/4} \mathbf{n}_{\alpha\beta,\parallel}, \tag{3.2}$$

where $\mathbf{n}_{\alpha\beta,\parallel} = \mathbf{u}_{\alpha\beta,\parallel} / \left|\mathbf{u}_{\alpha\beta,\parallel}\right|$ is a unit vector parallel to the relative velocity in the direction parallel to the contact surface, $\mathbf{u}_{\alpha\beta,\parallel}$. $\left|\mathbf{u}_{\alpha\beta,\parallel}\right|$ is also noted as $u_{\alpha\beta,\parallel}$. This formula was originally derived for a single particle dragged along a smooth surface (Steven P Meeker, Roger T Bonnecaze, & Michel Cloitre, 2004). The equation of $\mathbf{f}_{\alpha\beta}^{\text{r}}$ is given as,

$$\mathbf{f}_{\alpha\beta}^{\text{r}} = -\mu \left|\mathbf{u}_{\alpha\beta,\parallel}\right|^p \mathbf{n}_{\alpha\beta,\parallel}. \tag{3.3}$$

With inertia being negligible (T. Liu et al., 2018), the governing equation of motion of one soft particle α is derived to be

$$\frac{d\mathbf{x}_\alpha}{dt} = \mathbf{u}_\alpha = \dot{\gamma} y_\alpha \mathbf{e}_x + M_\alpha \sum_\beta \left(\mathbf{f}_{\alpha\beta}^{\text{near-drag}} + \mathbf{f}_{\alpha\beta}^{\text{elas}}\right), \tag{3.4}$$

where $\dot{\gamma}$ is the shear rate, y_α is the vertical location of the particle, and $\mathbf{e}_x$ is the unit vector in the *x*-direction; $M_\alpha = f(\phi)/6\pi R\eta_s$ is the mobility and is equivalent to the inverse of the dissipation constant in the Durian's model (Durian, 1995, 1997). The detailed model description and derivation of the equation of motion can be found in our earlier publications (T. Liu et al., 2018).

3.2.2 Analysis

The shear stress versus time from the oscillatory shear is used to extract storage and loss moduli. The system is equilibrated using conjugate gradient minimization of the overall energy and then is sheared over 20-100 periods depending on different configurations until the oscillation became stable and minimal difference is observed between consecutive periods. 20 periods of data are evaluated after the system entered such a state. The 20 periods are averaged to extract a single period for analysis.

In this one period, the stress doesn't oscillate around absolute zero due to numerical noise in many configurations because of residual stress even though the system is equilibrated. The one period of oscillating stress deducting the average stress during this period eliminates the vertical shift due to residual stress. The resulting one period of stress is fitted to the sine function,

$$\sigma(t) = \sigma_{\max} \sin(\omega t + \varphi). \tag{3.5}$$

Based on the definition of storage and loss modulus,

$$G' = \frac{\sigma_{\max} \cos\varphi}{\gamma_0}, \tag{3.6}$$

$$G'' = \frac{\sigma_{\max} \sin\varphi}{\gamma_0}. \tag{3.7}$$

3.3 RESULTS AND DISCUSSION

3.3.1 Storage Modulus

3.3.1.1 Variation with frequency

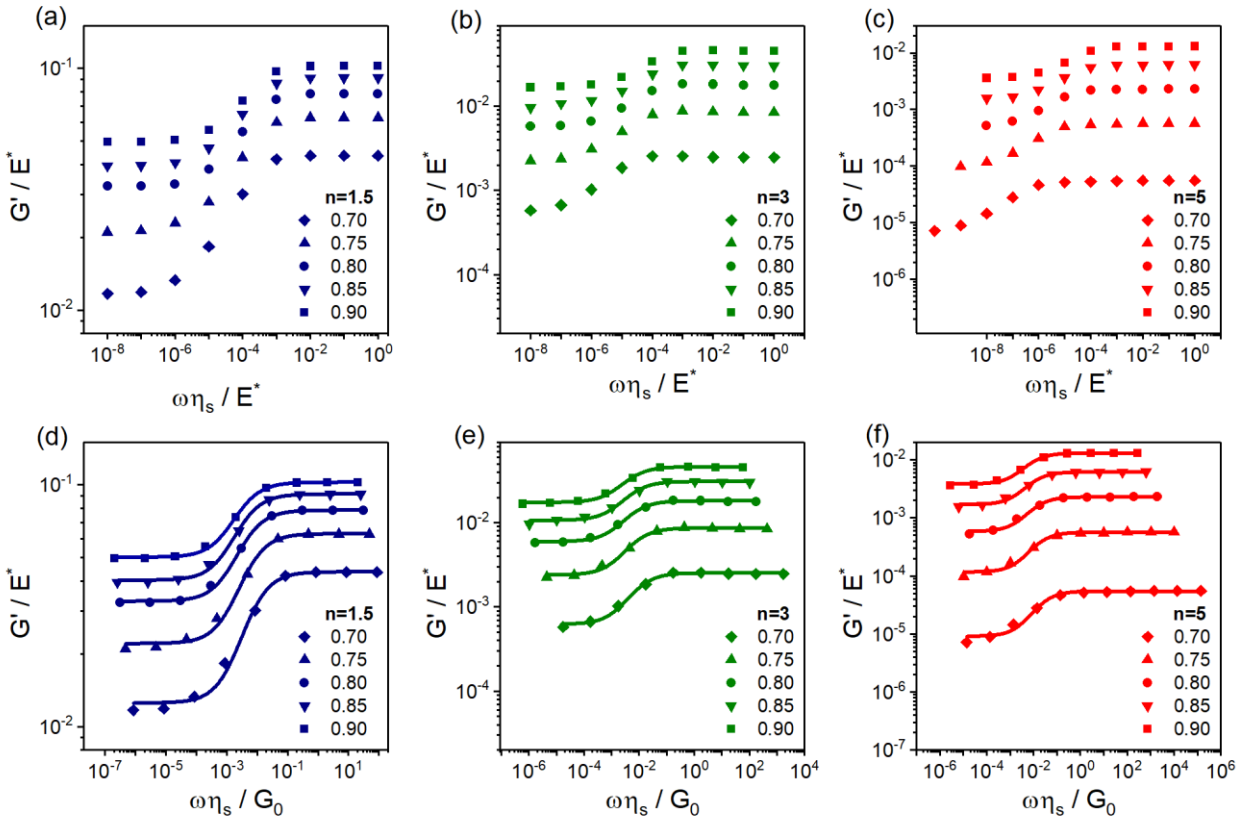

Figure 3.2: Dimensionless storage modulus variation versus dimensionless frequency (a-c) and scaled frequency (d-f) for all volume fractions at n = 1.5, 3 and 5.

Figures 3.2a-c show the extracted results of G' (written in short for the dimensionless G' / E, and similarly for G'' / E in the following text) for all volume fractions at n = 1.5, 3, and 5, respectively. In each case, the storage modulus transitions from a lower plateau value at low frequency to a higher plateau value at high frequency. The G' at the lowest frequency is noted as G_0 and at the highest frequency noted as G_∞.

G_0 embodies the stiffness unique to each material to start breaking cages and have a rearrangement of structure, given the material sufficient time to adjust their positions in the local environment. The low-frequency modulus G_0 agrees with the result in our earlier

publication (T. Liu et al., 2018) (known as *G* in the publication and shown as old data in half symbols in Figure 3.4d) which employs a different method of using elastic energy change of the system after very small steps. Enough relaxation is ensured between steps to approximate the 'low-frequency' requirement.

As the frequency increases, a fixed degree of rearrangement per time also gets more difficult. This explains the increase of *G'* with frequency. When the frequency increases to a point where the timescale of forced rearrangement is much smaller than the timescale required for adjusting their positions locally, the particles will act as if they cannot adjust locally. This is why *G'* will reach a limit at a high enough frequency. Theoretically, this limit can be computed with number density ρ, pair distribution function *g(r),* and the elastic interaction potential function *u(r)* using the formula in Eq. 3.8 developed by Zwanzig and Mountain (Zwanzig & Mountain, 1965). The G_∞ from our simulation agrees very well with the theoretical prediction using the same elastic force law as shown in Figure 3.4e.

$$G_\infty = -\frac{2\pi}{15}\rho^2 \int_0^{2R} g(r)\frac{d}{dr}\left[r^4 \frac{du(r)}{dr}\right]dr\,. \tag{3.8}$$

3.3.1.2 Empirical Equation

As is explained in earlier publications, η_s / G_0 is an effective generic timescale that embodied the competition between viscous dissipation in the solvent with viscosity η_s and the elastic rearrangement within cages with G_0. It has been shown to be effective in collapsing shear stress and normal stress differences under steady shear in both experiments and simulations. In this paper, the original *G'* is plotted against this scaled dimensionless frequency $\omega\eta_s$ / G_0 in the second row of Figure 3.2.

The transition between G_0 and G_∞ can be described by an empirical logistic formula in Eq. 3.9. In the classic logistic equation, the plot is symmetric with parameter 1/*A*, which signifies the center, and parameter *p* signifies the growth rate of *G'* with frequency. The plots in Figures 3.2d, 3.2e, and 3.2f are fitted using this formula and shown as continuous lines in

the figures. A value of p = 1 works well and the detailed fitting parameters are included in Table 3.1

$$G' = \frac{G_0 - G_\infty}{1 + \left(A \frac{\omega \eta_s}{G_0} \right)^p} + G_\infty . \tag{3.9}$$

Eq. 3.9 with p = 1 can be rearranged to the following transformed format of G',

$$\frac{G' - G_0}{G_\infty - G_0} = 1 - \frac{1}{1 + A \frac{\omega \eta_S}{G_0}} \tag{3.10}$$

Table 3.1: Parameter A in Eq. 3.9

	n = 1.5	n = 3	n = 5
0.70	413	264	151
0.75	380	234	128
0.80	306	221	99
0.85	237	176	74
0.90	175	126	50
Fitted result for all volume fractions	313	221	97
Fitted result for all volume fractions and all n's	194		

The transformed G' is plotted in Figures 3.3a, 3.3b, and 3.3c for n = 1.5, 3, and 5 accordingly. All the data points are shown together in Figure 3.3d. It can be observed that all results collapse roughly onto one curve. Each of them is fitted according to Eq. 3.10 and the detailed fitting parameters are included in Table 3.1. In Eq. 3.10, $A\eta_S / G_0$ symbolizes a characteristic timescale for particle local rearrangement at low frequency versus the affine motion. In Table 3.1, the value of parameter A increases as the volume fraction decreases and the elastic exponent n decreases. In all cases considered, A values differ within one order of magnitude, whereas A values for each different of n differ with a factor of 3.

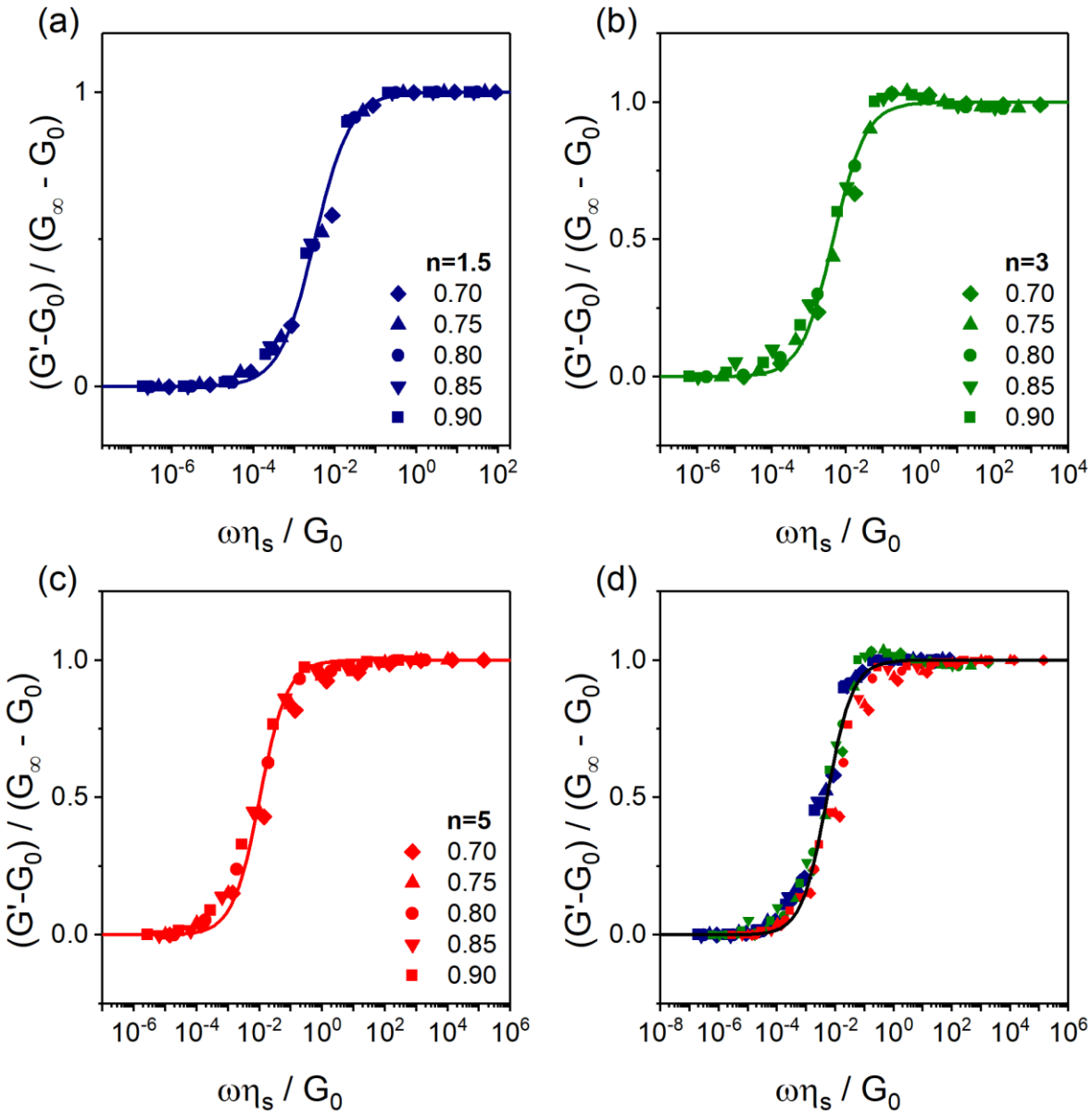

Figure 3.3 Transformed Storage modulus versus scaled frequency for all volume fractions at *n* = 1.5, 3, 5 (a-c) and combined three *n*'s (d).

3.3.1.3 Impact of near-field drag forces on G'

Adding near-field drag forces of various forms provides no substantial change to *G'* data as is shown in the supplementary material. This is similar to the non-significant role of near-field drag forces in steady shear (T. Liu et al., 2018). It is understandable due to the definition that *G'* describes the part in phase with the strain of overall modulus. At each specific time, the system is in a quasi-steady state and the overall forces on each particle are zero since

inertia is not important. In this case, the *G'* which is in phase with the strain is directly related to the elastic interaction between particles.

3.3.1.4 The relationship among G_0, G_∞, and g_{max}

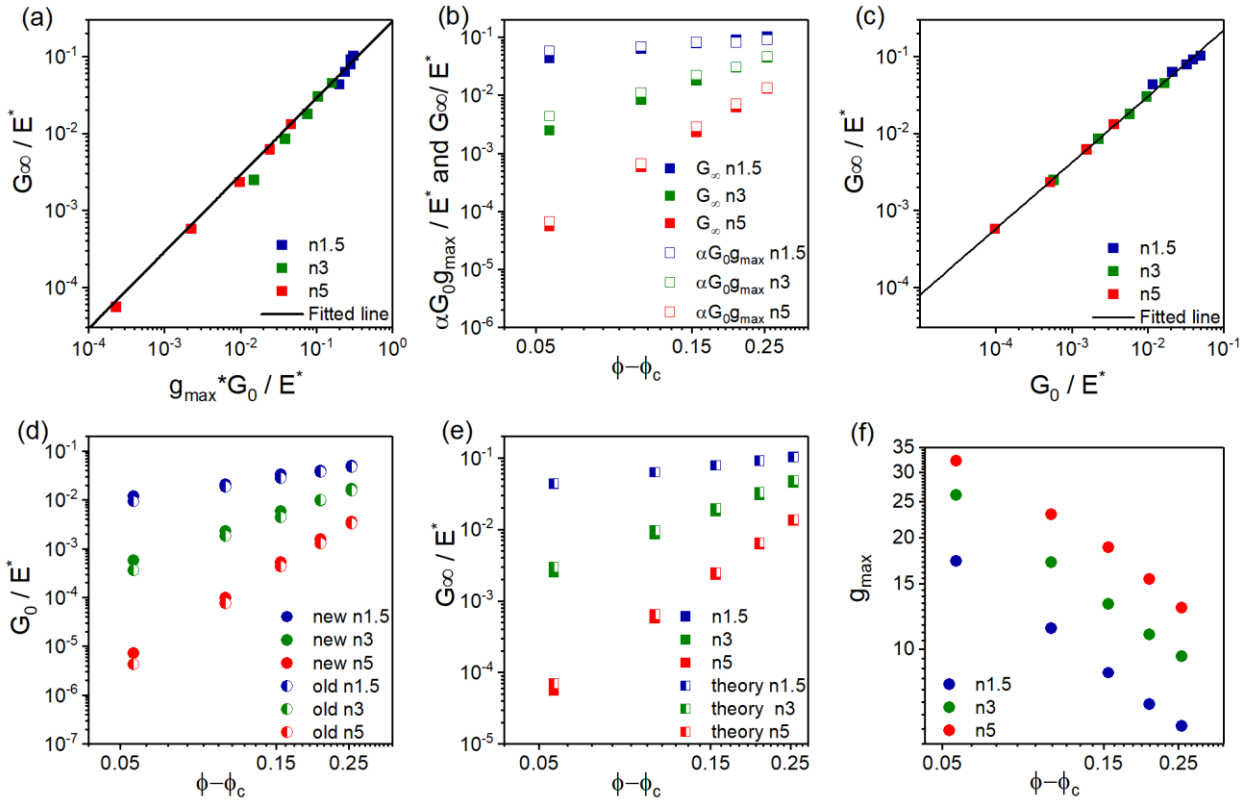

Figure 3.4: (a) G_∞ versus $g_{max}G_0$ with a solid fitted line as $G_\infty = 0.29 g_{max}G_0$; (b) $\alpha g_{max}G_0$ versus $\phi - \phi_c$ (empty symbols) compared with G_∞ versus $\phi - \phi_c$ (solid symbols); (c) G_∞ versus G_0 with fitted line as $G_\infty = 1.59G_0^{0.86}$; (d) Dimensionless G_0 versus $\phi - \phi_c$ for simulation results at the lowest frequency (closed symbols) and values obtained using a different method in (T. Liu et al., 2018) (half symbols); (e) Dimensionless G_∞ versus $\phi - \phi_c$ for simulation results at the highest frequency (closed symbols) and theoretical value with Eq. 3.8 (half symbols); (f) g_{max} versus $\phi - \phi_c$. (All G_∞ and G_0 are non-dimensionalized by E^* and omitted in the description)

It is found that G_∞ is roughly linear to the product of G_0 and g_{max} as in Eq. 3.11 and Figure 3.4a, where g_{max} is the maximum value of the pair distribution function $g(r)$. The value of linear coefficient α is around 0.29. The detailed $g(r)$ plots for all volume fractions at all n's are included in the supplemental information.

$$G_\infty = \alpha g_{\max} G_0 \tag{3.11}$$

This correlation is similar to and consistent with the argument (Brady, 1994) that the ratio of short-time diffusivity and long-time diffusivity scales as g_{max}. Without g_{max}, G_∞ is roughly a power law with respect to G_0 as shown in Figure 3.4c with a coefficient of 1.59 and an exponent of 0.86.

It has been shown in Figure 3.4d and in our earlier publication (T. Liu et al., 2018) that G_0 is a power-law function of the volume fraction distance to the jamming point $\phi - \phi_c$ as in Eq. 3.12, where ϕ is the volume fraction and ϕ_c is the random close packing value close to 0.645. The exponent p_1 is shown to be roughly n – 0.5. Plotting of G_∞ and g_{max} also shows power laws with respect to $\phi - \phi_c$, as shown in Figures 3.4e-f and Eqs. 3.13-3.14. Exponent p_2 is roughly n – 0.9 to n – 1.3 and p_3 takes values between - 0.6 to - 0.7. The detailed p_1, p_2, and p_3 values are included in Table 3.2. Variation of G_∞ and $\alpha g_{max} G_0$ with $\phi - \phi_c$ is shown in Figure 3.4(b). The fact that p_1+p_3 is roughly p_2 is consistent with Eq. 3.11.

$$G_0 = k_1(\phi - \phi_c)^{p_1} \tag{3.12}$$

$$G_\infty = k_2(\phi - \phi_c)^{p_2} \tag{3.13}$$

$$g_{\max} = k_3(\phi - \phi_c)^{p_3} \tag{3.14}$$

Table 3.2: Parameter k and p in Eqs. 12-14

n	1.5		3		5	
Parameter	k	p	k	p	k	p
G_0	0.2	1.0	0.3	2.3	1.0	4.1
G_∞	0.2	0.6	0.6	1.9	1.8	3.6
g_{max}	2.4	-0.7	3.8	-0.7	5.9	-0.6

3.3.2 Loss Modulus

3.3.2.1 Impact of near-field forces

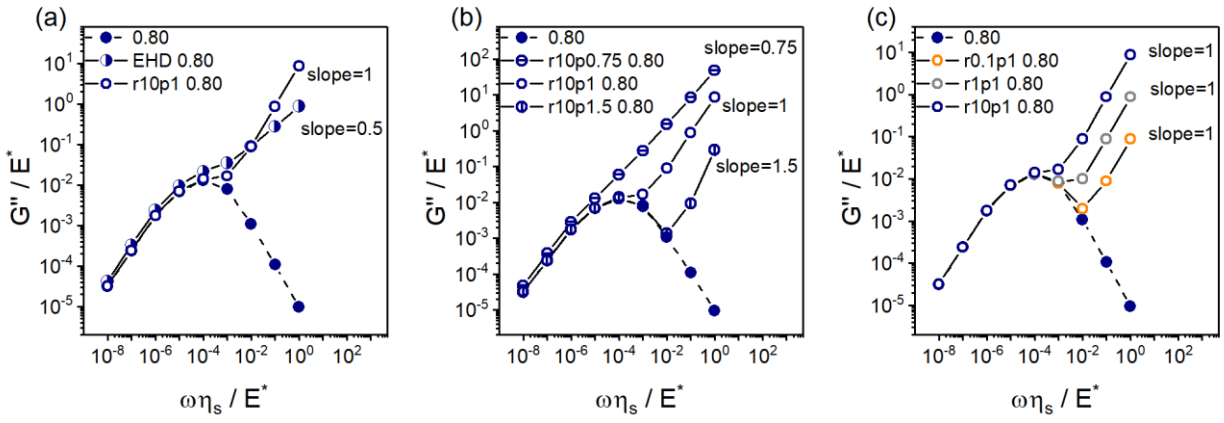

Figure 3.5: Dimensionless loss modulus versus dimensionless frequency at n =1.5 and ϕ = 0.80 for (a) different near-field drag forces (no near-field drag forces, $\mathbf{f}_{\alpha\beta}^{\mathrm{EHD}}$, and $\mathbf{f}_{\alpha\beta}^{\mathrm{r}}$ with μ = 10 and p = 1); (b) $\mathbf{f}_{\alpha\beta}^{\mathrm{r}}$ with different p and μ = 10; (c) $\mathbf{f}_{\alpha\beta}^{\mathrm{r}}$ with different μ and p = 1.

Unlike the storage modulus, the system shows very substantial differences for different near-field drag forces as shown in Figure 3.5a for n = 1.5 and ϕ = 0.80.

The solid symbols in Figure 3.5a show the results for systems with no near-field drag forces and demonstrate the effect of far-field drag forces which are embedded as Stokes' law in the equation of motion. As the dimensionless frequency increases, *G"* first increases; this is due to more frequent oscillation causing more vigorous drag forces and resulting in larger dissipation. As the frequency continues to increase, *G"* reaches a maximum and starts to decrease. Similar to the explanation in *G'* part, when the frequency increases to a point where the timescale of forced rearrangement is much smaller than the timescale required for adjusting their positions locally, the particles will act as if they can't adjust locally, the system will appear to be a purely elastic system, with particles doing almost affine movement in accordance of the strain. Consequently, the complex modulus is also almost entirely in phase with strain. Due to the definition of *G'*, the complex modulus is mainly *G'* with *G"* being minimal. This explains why *G"* keeps decreasing at high frequency.

The half and empty symbols in Figure 3.5a show the results for $\mathbf{f}_{\alpha\beta}^{\mathrm{EHD}}$ and $\mathbf{f}_{\alpha\beta}^{\mathrm{r}}$ (with μ = 10 and p = 1). The difference between them and solid symbols shows the effect of these two near-field drag forces. The results implicate large amounts of energy losses due to near-field drag forces which are directly related to the relative movement of neighboring particles. The figure also proves that the high-frequency *G"* is mainly due to viscous forces, not elastic forces**.**

Our previous publication has shown that near-field drag forces play a non-substantial role in shear and normal stress calculation for steady shear. Here it shows the opposite conclusion for *G"* in oscillatory shear at high frequency. This is probably because, in steady shear where the system is under constant shear rate, the effect of near-field drag forces on a specific particle from all its neighboring particles are centrosymmetric and counter-balance each other.

Figures 3.6a-f show the results for more volume fractions and *n*'s compared with Figure 3.5a. In all cases at high-frequency regions, the *G"* increases as a power law of frequency with the exponent being 0.5 for $\mathbf{f}_{\alpha\beta}^{\mathrm{EHD}}$ and being 1 for $\mathbf{f}_{\alpha\beta}^{\mathrm{r}}$ (with μ = 10 and p = 1). $\mathbf{f}_{\alpha\beta}^{\mathrm{EHD}}$ is related with the relative overlap distances in Eq. 3.2 and thus have different results for different volume fractions for the same frequency, whereas $\mathbf{f}_{\alpha\beta}^{\mathrm{r}}$ doesn't have the effect of the overlap distance and its results are irrelevant with volume fraction. In all cases, the near-field drag forces start to show their importance when the frequency is higher than the one corresponding to maximum *G"* in the non-near-field-drag-force cases.

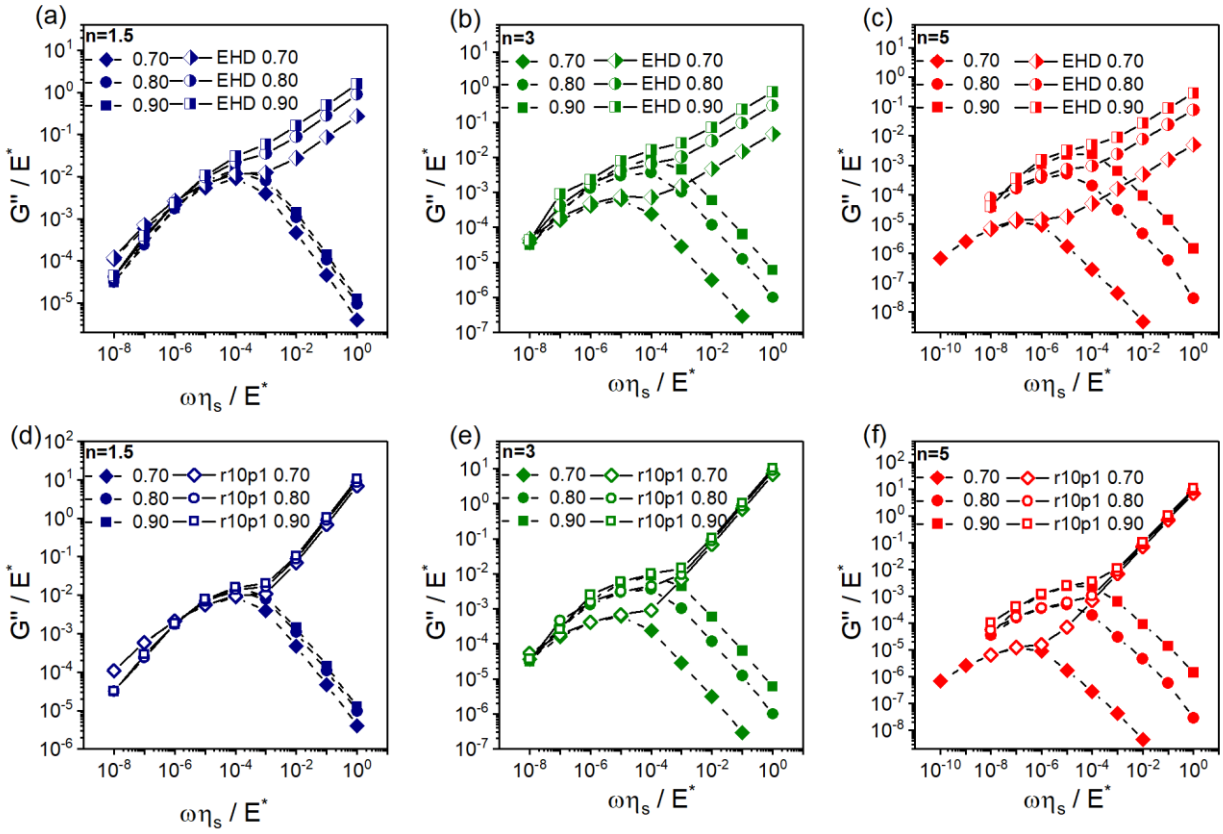

Figure 3.6: Dimensionless loss modulus versus dimensionless frequency with three volume fractions at n = 1.5, 3, and 5 for $\mathbf{f}_{\alpha\beta}^{\mathrm{EHD}}$ (a-c, half symbols) and $\mathbf{f}_{\alpha\beta}^{\mathrm{r}}$ with μ = 10 and p = 1 (d-f, empty symbols) comparing with cases without near-field drag forces (closed symbols).

3.3.2.2 Impact of different parameters in near-field force law

Figures 3.5b and 3.5c show the results for the impact of p and μ in $\mathbf{f}_{\alpha\beta}^{\mathrm{r}}$.

In the previous section, it is mentioned that the power-law exponent with respect to frequency being 0.5 for $\mathbf{f}_{\alpha\beta}^{\mathrm{EHD}}$ and being 1 for $\mathbf{f}_{\alpha\beta}^{\mathrm{r}}$ with p =1 at high-frequency regions. Considering the equation forms for these two force law in Eq. 3.2 and Eq. 3.3 where the exponent of $\left|\mathbf{u}_{\alpha\beta,\parallel}\right|$ being 0.5 and 1. It's natural to infer the exponent of *G"* versus frequency at high frequencies being equal to the exponent of $\left|\mathbf{u}_{\alpha\beta,\parallel}\right|$ in the near-field drag force law. Figure 3.5b proves this conclusion with two more cases and shows that with p = 0.75, the exponent of *G"* is 0.75 (symbols with horizontal lines in the middle) and with p =1.5, the exponent of *G"* is also 1.5 (symbols with vertical lines in the middle).

Figure 3.5c shows the effect of coefficient μ in $\mathbf{f}_{\alpha\beta}^{r}$ where μ = 10 is shown in blue, μ = 1 in grey, and μ = 0.1 in orange. It can be observed as expected that μ directly affects the magnitude of $\mathbf{f}_{\alpha\beta}^{r}$ and controls the frequency from which $\mathbf{f}_{\alpha\beta}^{r}$ starts to gain dominance in *G''*.

3.3.2.3 Scaled loss modulus

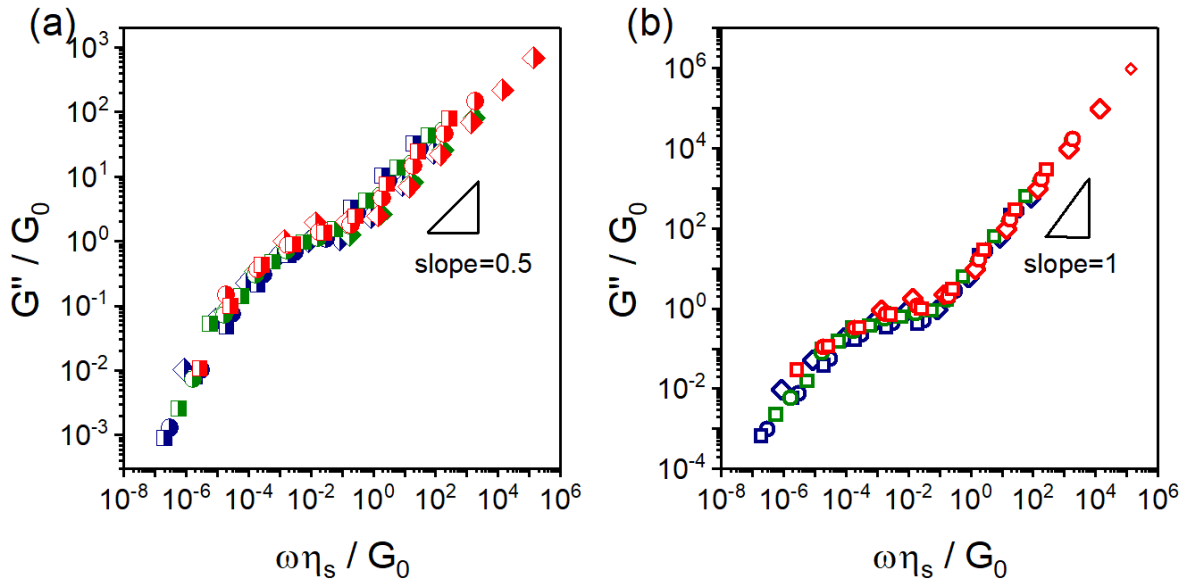

Figure 3.7: Scaled loss modulus versus scaled frequency for all volume fractions at n = 1.5, 3, 5 for $\mathbf{f}_{\alpha\beta}^{EHD}$ (a) and $\mathbf{f}_{\alpha\beta}^{r}$ with μ = 10 and p = 1 (b). (The symbols are the same as in Figure 3.6)

Similar to storage modulus in earlier sections and previous publications (T. Liu et al., 2018), scaling dimensionless modulus and dimensionless with dimensionless G_0 collapsed all data points at all n's with all volume fractions for both $\mathbf{f}_{\alpha\beta}^{EHD}$ in Figure 3.7a and $\mathbf{f}_{\alpha\beta}^{r}$ with μ = 10 and p = 1 in Figure 3.7b. The $\mathbf{f}_{\alpha\beta}^{r}$ force law, which has a simpler form compared to $\mathbf{f}_{\alpha\beta}^{EHD}$ with no relevance to volume fractions, also has a better collapse.

3.3.3 Comparison with experiments

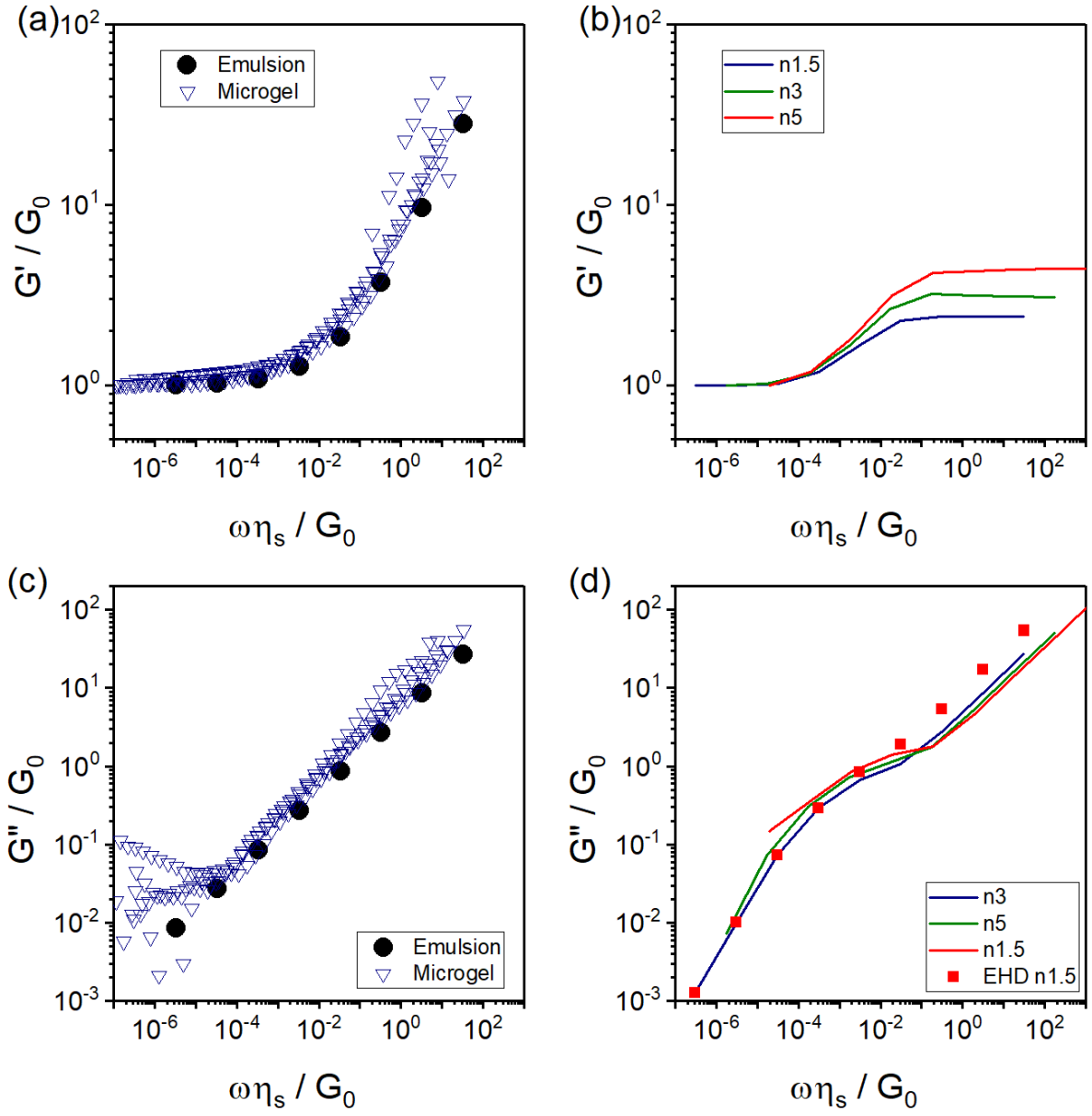

Figure 3.8: Simulation results of G' (b) and G" (d) compared with experimental data (a, c) from emulsion (A. J. Liu et al., 1996) (black solid circle) and microgel (Monti, 2010) (blue empty triangle). In (d), red squares denote simulation with the original EHD drag force multiplied by a factor of 2 in Eq. 3.2. In both (b) and (d), the three lines use the original EHD drag force in Eq. 3.2.

The comparison between experiments and simulations is shown in Figure 3.8. The emulsion experiments (A. J. Liu et al., 1996) use light scattering and measure concentrated

silicone oil droplets in water. The microgel experiments (Monti, 2010) use diffusing wave spectroscopy and measure 4 different systems including microgels with different crosslink densities and different solvents (water or water-glycerol). The chaotic scattering measurements at low frequency for microgel are due to unstableness when starting the experiment and can be omitted. When scaled with G_0 and solvent viscosity η_S, all these experimental results collapse onto the same curve for both storage and loss modulus.

The simulations with different elastic exponents are shown as lines with different colors in Figures 3.2b and 3.2d.

For storage modulus, simulation at n = 1.5 has a better agreement with experiments at low frequency compared to n = 3 or 5. This is probably due to the fact that the actual elastic law between emulsion and microgel particles is roughly Hertzian with an exponent of 1.5. The experiments don't show a plateau as the simulation results, which suggests the model might lack certain elements of physics at high frequency compared to the actual experiment.

For loss modulus, both simulations and experiments exhibit the same power of 0.5 at high frequency. Simulations with different elastic exponents and the original EHD drag force are shown in lines and have similar results. When the original EHD drag force is multiplied by a factor of 2, the best agreement is achieved between simulation and experiments.

3.4 CONCLUSIONS

In this work, we propose a way to calculate G_0 based on just pairwise distribution function $g(r)$ and force potential by first estimating G_∞ using Zwanzig and Mountain formula in Eq. 3.8 and then relating G_∞ to G_0 with g_{max}. The model could be applied to a wide range of pairwise elastic force laws since any force law can be decomposed into Taylor series of different elastic exponent and our work showed the universality of the model by presenting result for a range of n's. We've also summarized a universal sigmoidal rule describing how storage modulus varies with frequency when changing from G_0 to G_∞. As for loss moduli, we've identified the important influence of different near-field drag forces in high frequencies. It is found that the exponent of near-field drag forces regarding the relative

velocity of pairwise neighbors determines the power-law exponent of loss moduli with frequency at high-frequency range.

SUPPLEMENTAL S3

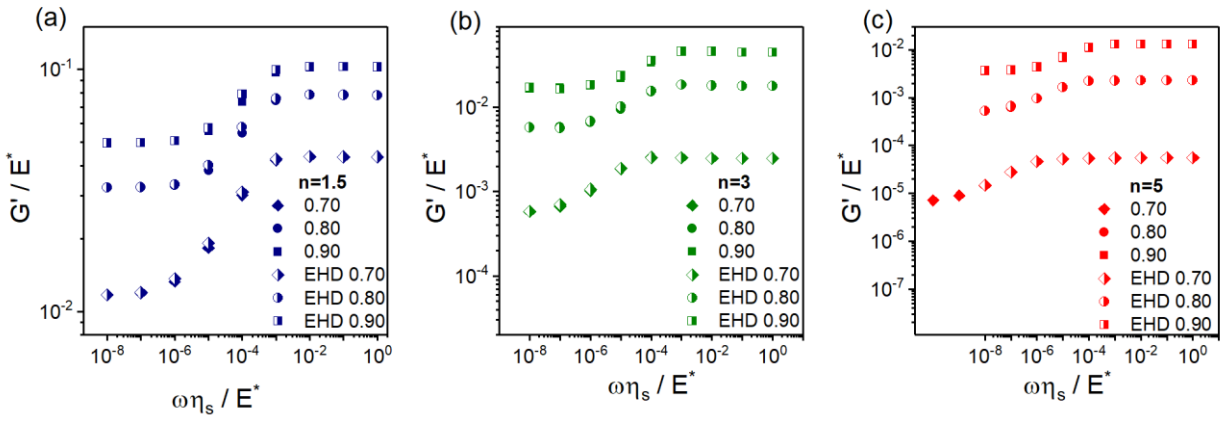

Figure 3.9: Dimensionless storage modulus variation versus dimensionless frequency for all volume fractions at n = 1.5, 3, and 5 for cases without near-field drag forces (closed symbols) and EHD (empty symbols).

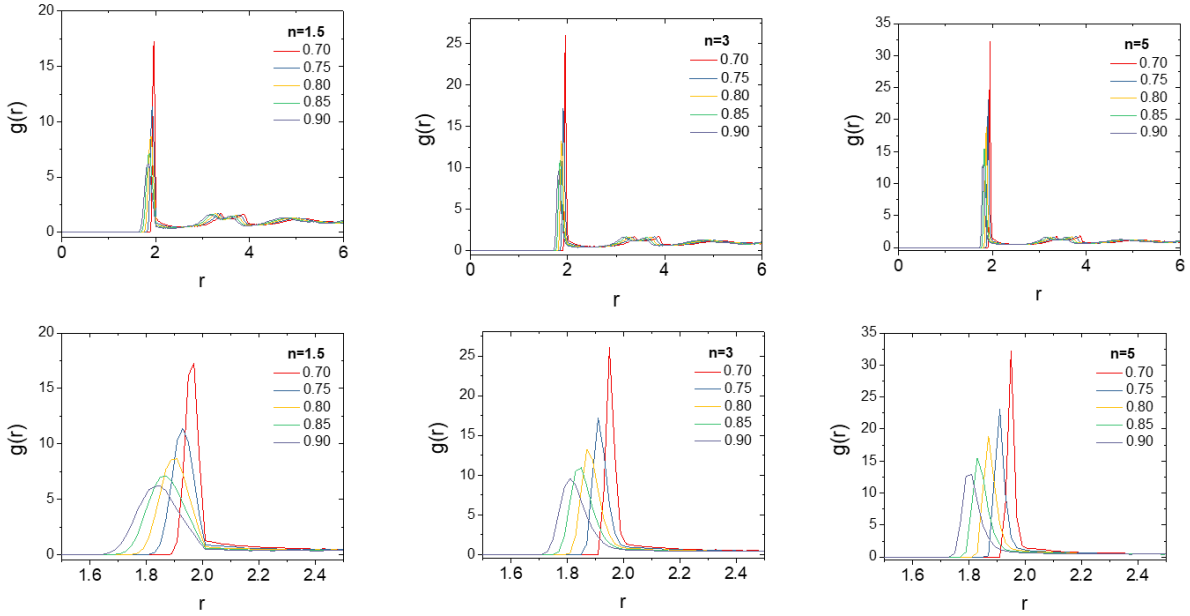

Figure 3.10: *g(r)* plots to extract g_{max} values for all volume fractions at all n's (first row: large range of r; second row: enlarged version of the first row).

Table 3.3: G_0, G_∞ , *and* g_{max} in Figure 3.4

	Volume fraction	n = 1.5	n = 3	n = 5
G_0	0.70	0.0117	5.77E-4	7.17E-6
	0.75	0.0210	0.00225	9.78E-5
	0.80	0.0325	0.00578	5.20E-4
	0.85	0.0395	0.00964	0.00157
	0.90	0.0497	0.01673	0.00359
G_∞	0.70	0.0435	0.00248	5.52E-5
	0.75	0.0625	0.00846	5.73E-4
	0.80	0.0783	0.0178	0.00231
	0.85	0.0914	0.0302	0.00620
	0.90	0.102	0.0450	0.0131
g_{max}	0.70	17.2	26.0	32.2
	0.75	11.3	17.1	23.0
	0.80	8.64	13.2	18.8
	0.85	7.11	10.9	15.4
	0.90	6.21	9.59	12.9

Chapter 4: A novel model on the rheology of soft particle materials near walls

4.1 INTRODUCTION

One fundamental component of the rheology of soft particle materials is wall slip that occurs in many natural phenomena and industrial processes. The identification and proper correction of wall slip are important to ensure proper rheological characterization and processing of soft particle materials (Cloitre & Bonnecaze, 2017; Hatzikiriakos, 2015; Malkin & Patlazhan, 2018). It's also important during the use and applications of soft glassy materials as slip over certain surfaces is a fundamental property of these materials which cannot be avoided. There are also circumstances where slip can be exploited as it enables materials to be transported with less friction and energy consumption. For example, a thin water film or hydrocarbon can be used in oil pipelining to form a thin layer around core oil and form a core-annular regime which provides lubrication of the oil core and promotes more efficient oil transportation (Joseph, 1997; Joseph, Bai, Chen, & Renardy, 1997)

The flow field of soft particle materials under shear is not always uniform and homogeneous. Under certain conditions, shear strain can be localized in a narrow zone, known as shear banding. Slip is an extreme form of strain localization. When slip occurs, a large velocity gradient and energy dissipation occur close to the wall. In many cases including polymer solutions, polymer melts, solid suspensions, and pastes, slip occurs in a thin layer near the wall; this phenomenon is known as the apparent slip (Hatzikiriakos, 2015), differentiating from true slip, where slip occurs abruptly at the interface between the fluid and the wall (Cloitre & Bonnecaze, 2017). Here we focus on the case of true slip, where the effects of shear banding are negligible or not apparent.

Soft particle materials only start to flow above yield stress σ_y when sheared over a no-slip rough surface. During wall slip, soft particle materials can move over a smooth surface subject to stress much smaller than the yield stress, but the stress needs to be larger than a critical value σ_c for some surfaces depending on the surface characteristics (Seth et al.,

2012). Zhang et al. have used the example of an oil-in-water emulsion to show that this critical stress σ_c is an artifact because of edge effects (evaporation along the line of contact) (Zhang et al., 2017; Zhang et al., 2018).

One interesting aspect of wall slip over a smooth wall is the relationship between slip velocity V_{slip} and the wall shear stress σ. For hard particle solutions, σ can generally be represented as the sum of a constant residual and a term linear to the velocity (P Ballesta, Besseling, Isa, Petekidis, & Poon, 2008; Pierre Ballesta, Koumakis, Besseling, Poon, & Petekidis, 2013; P Ballesta, Petekidis, Isa, Poon, & Besseling, 2012). For soft particle materials such as emulsions and microgels, previous wall slip experiments identified two power-law regimes between V_{slip} and σ: a parabolic dominated regime when the shear rate is small and soft particles move like a plug flow:

$$V_{slip} \sim \sigma^2 ; \tag{4.1}$$

and a linear dominated regime when the shear rate is large and soft particles develop flow within themselves:

$$V_{slip} \sim \sigma . \tag{4.2}$$

Meeker et al. and Seth et al. have developed models and experiments related to the parabolic regime shown as Eq. 4.1 (S. P. Meeker, R. T. Bonnecaze, & M. Cloitre, 2004; Steven P Meeker et al., 2004; Seth et al., 2008; Seth et al., 2012). In the parabolic regime, when the squeezed soft particles are sliding over the bottom smooth wall, a lift force is generated due to the asymmetric deformation and pressure distribution of the contacting facet. The elastohydrodynamic lubrication solvent layer is generated in this gap, facilitating the sliding motion.

While the mechanism in the parabolic regime is relatively well explained by the elastohydrodynamic lubrication theory, the microscopic origin of the linear regime between V_{slip} and σ hasn't been well investigated.

The work by Meeker et al. introduced elastohydrodynamic (EHD) forces, which were later incorporated and systematically analyzed in a simulation model developed by Seth et al

(Seth et al., 2011). This simulation model was able to simulate the case of bulk rheology, but can't serve as a tool for cases including walls.

Our previous work has shown that including elastohydrodynamic (EHD) forces in the equation of motion doesn't change the flow curves of bulk rheology (T. Liu et al., 2018). The role of EHD forces hasn't been investigated by simulation methods for shear between both rough-rough walls and rough-smooth walls.

In this work, we have developed simulation models for cases including shearing both rough-rough walls and rough-smooth walls, which can serve as generic tools for simulation including walls. Our model between rough-smooth walls proposes a mechanism that incorporates the temporary fixation of randomly-selected soft particles on the wall. This mechanism generates results that can replicate the experimental $V_{slip} \sim \sigma$ linear relationship, shedding light on the microscopic origin of this linear regime, which is still not well understood according to previous literature. Our models also investigated the role of EHD forces in cases of shear between both rough-rough walls and rough-smooth walls.

4.2 Computational Method

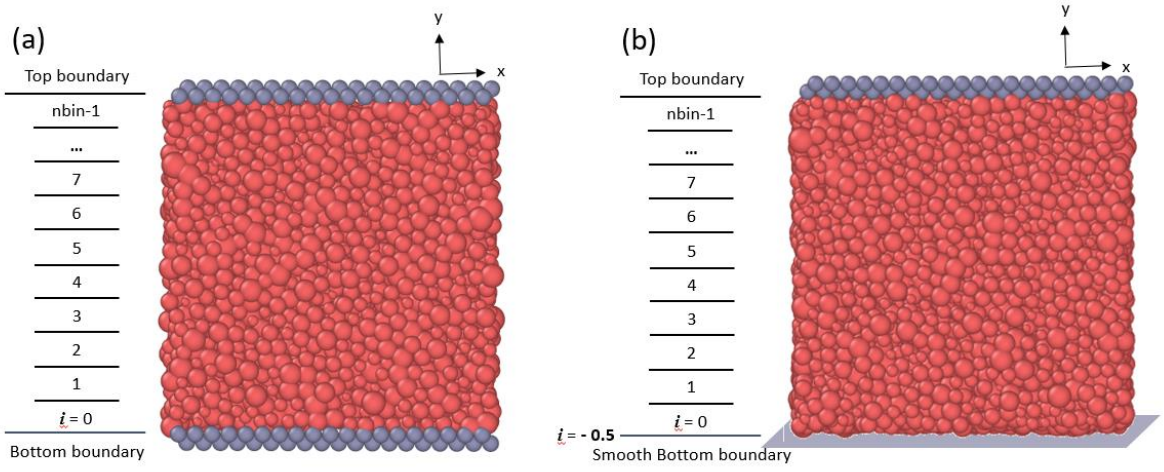

Figure 4.1: Soft particles sheared between rough-rough walls (a) and rough-smooth walls (b).

Around 10,000 soft particles (red in Figure 4.1) are randomly packed between two walls (grey in Figure 4.1) and are sheared by fixing the bottom wall and moving the top wall in the *x*-direction. The wall particles have the same radius as the average radii of all freely moving sheared particles, which have a polydispersity of 20% to avoid shear-induced structures (Khabaz et al., 2018; Khabaz et al., 2017).

Each rough wall contains two layers of wall particles. This is because one layer of wall particles forming square-lattice in the *x*-*z* plane would have interstices or holes in the centers of four neighboring wall particles, through which small free particles could escape during shearing. In the two-layer structure, the wall particles of the top layer lie right on top of the interstices of the bottom layer.

The shearing region of soft particles is divided into N_{bin} horizontal bins with bin index *i* listed from 0 to $N_{bin} - 1$ as is shown in Figure 4.1. The boundary of the region for the rough wall is located at the center of the inner layer. The smooth wall is a purely flat surface and thus defines its side of the region boundary.

The interaction between a rough wall particle and soft particles is the same as that between two soft particles α and β, including a pairwise repulsive elastic Hertzian-style force (K. K. Liu et al., 1998),

$$\mathbf{f}_{\alpha\beta}^{\text{elas}} = \frac{4}{3} C E^* \varepsilon_{\alpha\beta}^n R_c^2 \mathbf{n}_\perp , \tag{4.3}$$

where $E^* = E / 2(1-\nu^2)$ is the contact modulus based on the Young modulus E and Poisson ratio ν, $R_c = R_\alpha R_\beta / (R_\alpha + R_\beta)$ is the contact radius, $\varepsilon_{\alpha\beta} = \left(R_\alpha + R_\beta - r_{\alpha\beta}\right) / R_c$ is the dimensionless overlap distance characterizing the degree of compression, and $\mathbf{n}_\perp$ is the unit vector perpendicular to the flat surface representing the particle-particle contact. The values of C and n change with $\varepsilon_{\alpha\beta}$ as follows: when $0 < \varepsilon_{\alpha\beta} \le 0.1$, n

= 1.5 and C = 1; when $0.1 < \varepsilon_{\alpha\beta} \le 0.2$, n = 3 and C = 31.62; when $\varepsilon_{\alpha\beta} > 0.2$, n = 5 and C = 790.6. The wall particles are chosen to have the same properties (C, E^*) as soft particles for easier implementation.

The elastic force between a soft particle and the bottom smooth wall is the same as Eq. 4.3, in the limit of one of the two particles going to infinite radius and mass (flat wall), where C, E^* has the same meaning as before, $R_c = R_\alpha$ because of the infinite radius of a flat wall, and $\varepsilon_{\alpha\beta} = \left(R_\alpha - r_{\alpha\beta}\right)/R_\alpha$.

During shearing assuming Lees-Edwards boundary conditions (Seth et al., 2011) without walls, the equation of motion for particle α is,

$$\frac{d\mathbf{x}_\alpha}{dt} = \mathbf{u}_\alpha = u_\infty \mathbf{e}_x + M_\alpha \sum_\beta \mathbf{f}_{\alpha\beta}^{\text{elas}} . \tag{4.4}$$

The velocity field $u_\infty = \dot{\gamma} y_\alpha$ is the expected shearing result. However, we cannot impose this velocity but rather achieve it by ensuring the shear stress is uniform across the gap.

In our model, in order to simulate the effect of walls, we describe two different methods of updating the term u_∞: method 1 that works for when both walls are rough, and method 2 for one wall is rough and the other is smooth.

4.2.1 Method 1: Shear between rough-rough walls

At steady state, the fluid maintains uniform shear stress σ across all the bins in the y direction. Thus,

$$\frac{d\sigma}{dy} = \frac{d}{dy}\left(\eta \frac{du}{dy}\right) = 0 , \tag{4.5}$$

$$\frac{\left(\eta \frac{du}{dy}\right)\Big|_{i+0.5} - \left(\eta \frac{du}{dy}\right)\Big|_{i-0.5}}{\Delta y} = 0 , \tag{4.6}$$

where *i* denotes the bin number.

(1) For the internal bins (*i* from 1 to N_{bin} - 2),

$$\eta_{i+0.5}^{n}\frac{u_{i+1}^{n}-u_{i}^{n}}{\Delta y}-\eta_{i-0.5}^{n}\frac{u_{i}^{n}-u_{i-1}^{n}}{\Delta y}=0 \quad \Rightarrow \quad u_{i}^{n+1}=u_{i}^{n}=\frac{\eta_{i+0.5}^{n}u_{i+1}^{n}+\eta_{i-0.5}^{n}u_{i-1}^{n}}{\eta_{i+0.5}^{n}+\eta_{i-0.5}^{n}}, \tag{4.7}$$

where $\eta_{i+0.5}^{n}=\dfrac{\dfrac{\sigma_{i+1}^{n}+\sigma_{i}^{n}}{2}}{\dfrac{u_{i+1}^{n}-u_{i}^{n}}{\Delta y}}$ and $\eta_{i-0.5}^{n}=\dfrac{\dfrac{\sigma_{i-1}^{n}+\sigma_{i}^{n}}{2}}{\dfrac{u_{i}^{n}-u_{i-1}^{n}}{\Delta y}}$.

(2) For the top bin ($i = N_{bin}$ - 1),

$$\eta_{i+0.5}^{n}\frac{u_{i+1}^{n}-u_{i}^{n}}{0.5\Delta y}-\eta_{i-0.5}^{n}\frac{u_{i}^{n}-u_{i-1}^{n}}{\Delta y}=0 \quad \Rightarrow \quad u_{i}^{n+1}=u_{i}^{n}=\frac{2\eta_{i+0.5}^{n}u_{i+1}^{n}+\eta_{i-0.5}^{n}u_{i-1}^{n}}{2\eta_{i+0.5}^{n}+\eta_{i-0.5}^{n}}, \tag{4.8}$$

where $\eta_{i+0.5}^{n}=\dfrac{\dfrac{\sigma_{top}^{n}+\sigma_{i}^{n}}{2}}{\dfrac{u_{top}-u_{i}^{n}}{y_{top}-y_{i}}}$ and $\eta_{i-0.5}^{n}=\dfrac{\dfrac{\sigma_{i-1}^{n}+\sigma_{i}^{n}}{2}}{\dfrac{u_{i}^{n}-u_{i-1}^{n}}{\Delta y}}$.

(3) For the bottom bin (i = 0),

$$\eta_{i+0.5}^{n}\frac{u_{i+1}^{n}-u_{i}^{n}}{\Delta y}-\eta_{i-0.5}^{n}\frac{u_{i}^{n}-u_{i-1}^{n}}{0.5\Delta y}=0 \quad \Rightarrow \quad u_{i}^{n+1}=u_{i}^{n}=\frac{\eta_{i+0.5}^{n}u_{i+1}^{n}+2\eta_{i-0.5}^{n}u_{i-1}^{n}}{\eta_{i+0.5}^{n}+2\eta_{i-0.5}^{n}}, \tag{4.9}$$

where $\eta_{i+0.5}^{n}=\dfrac{\dfrac{\sigma_{i+1}^{n}+\sigma_{i}^{n}}{2}}{\dfrac{u_{i+1}^{n}-u_{i}^{n}}{\Delta y}}$ and $\eta_{i-0.5}^{n}=\dfrac{\dfrac{\sigma_{bottom}^{n}+\sigma_{i}^{n}}{2}}{\dfrac{u_{i}^{n}-u_{bottom}}{y_{i}-y_{bottom}}}$.

In Eq. 4.7 – 4.9, $\eta_{i+0.5}^{n}$ or $\eta_{i-0.5}^{n}$ is the viscosity at the interface between neighboring bins; u_{i}^{n} is the average velocity of particles in the i^{th} bin at timestep *n*; σ_{i}^{n} is the shear stress in the i^{th} bin at timestep *n* and is calculated using Kirkwood formula (R. G. Larson, 1999). σ_{top}^{n}, σ_{bottom}^{n} is the stress on top/bottom walls calculated by dividing the total force on the wall by the cross-sectional area in the *x*-*z* plane, serving as boundary conditions.

The velocity is interpolated according to their *y* positions between neighboring bins as

$$u_{i+1/2}^{n+1}\left(\text{interpolate}\right)=\frac{u_{i+1}^{n+1}-u_{i}^{n+1}}{2\Delta y}\left(y-y_{mid}\right), \tag{4.10}$$

where y_{mid} is the middle position in the *y* direction in the bin, and applied in the next timestep. The equation of motion is:

$$\frac{d\mathbf{x}_\alpha}{dt}=\mathbf{u}_\alpha=u_{i+1/2}^{n+1}(\text{interpolate})\mathbf{e}_x+M_\alpha\sum_\beta\mathbf{f}_{\alpha\beta}^{\text{elas}}\ . \tag{4.11}$$

Note that the $u_i^{n+1}(\text{interpolate})$ replaces u_∞ in Eq. 4.4, estimating with information from neighboring bins instead of forcing a linear velocity profile.

As will be shown, this method successfully simulates the velocity and shear stress profile when shear between two rough walls. However, it doesn't work for cases between a rough wall and a smooth wall. For the rough-smooth wall case, we use a second method.

The simulations between rough-rough walls resemble those of bulk rheology and don't include EHD forces. Including EHD forces for shear between rough-rough walls doesn't change the result, consistent with our previous conclusion about the negligible role of EHD forces for bulk flow curves.

4.2.2 Method 2: Shear between rough–smooth or rough-rough walls

The velocity magnitude of a soft particle in the *x* direction *u* can be related with the shear stress σ using the density ρ and time *t* in equation 4.10,

$$\rho\frac{\partial u}{\partial t}=\frac{\partial\sigma}{\partial y}. \tag{4.12}$$

(1) For internal bins (*i* from 1 to N_{bin} - 2), this equation can be rewritten as,

$$\rho\frac{u_i^{n+1*}-u_i^n}{\Delta t}=\frac{\sigma_{i+1}^n-\sigma_{i-1}^n}{2\Delta y}, \tag{4.13}$$

which enables us to derive the velocity in each bin using information from the last time step.

(2) For the top bin ($i = N_{bin} - 1$),

$$\rho\frac{u_i^{n+1*}-u_i^n}{\Delta t}=\frac{\partial\sigma}{\partial y}\Big|_{i+0.5}=\frac{\sigma_{i-1}^n-9\sigma_i^n+8\sigma_{top}^n}{3\Delta y}. \tag{4.14}$$

(3) For the bottom bin ($i = 0$),

$$\rho\frac{u_i^{n+1*}-u_i^n}{\Delta t}=\frac{\partial\sigma}{\partial y}\Big|_{i-0.5}=\frac{\sigma_{i+1}^n+3\sigma_i^n-4\sigma_{bottom}^n}{3\Delta y}. \tag{4.15}$$

Since $\sigma_i^n=\sigma_0^n=\sigma_{bottom}^n$, this equation can also be transformed into,

$$\rho\frac{u_i^{n+1*}-u_i^n}{\Delta t}=\frac{\partial\sigma}{\partial y}\Big|_{i-0.5}=\frac{\sigma_{i+1}^n-\sigma_{bottom}^n}{3\Delta y}. \tag{4.16}$$

In Eq. 4.13 to Eq. 4.16, u_i^n is the average velocity of particles in the i th bin at timestep n; σ_{top}^n, σ_{bottom}^n is the stress on top/bottom walls calculated by dividing the total force on the wall by the cross-sectional area in the x-z plane. When $i = 0$, u_0^n is the slip velocity over a smooth surface.

The Lax method is required for numerical stability:

(1) For inner bins, we use $0.5(u_{i-1}^n+u_{i+1}^n)$ to replace u_i^n in Eq. 4.13 and get,

$$u_i^{n+1*}=0.5(u_{i-1}^n+u_{i+1}^n)+\frac{\Delta t}{2\rho\Delta y}(\sigma_{i+1}^n-\sigma_{i-1}^n). \tag{4.17}$$

(2) For the top bin (*i=nbin-1*), we use $(\frac{2}{3}u_{i+0.5}^n+\frac{1}{3}u_{i-1}^n)$ to replace u_i^n in Eq. 4.14 and get,

$$u_i^{n+1*}=(\frac{2}{3}u_{i+0.5}^n+\frac{1}{3}u_{i-1}^n)+\frac{\Delta t}{3\rho\Delta y}(\sigma_{i-1}^n-9\sigma_i^n+8\sigma_{top}^n). \tag{4.18}$$

(3) For the bottom bin (i = 0), the traditional lax method uses velocity from neighboring bins to substitute u_i^n in Eq. 4.16. However, considering the discontinuity of velocity near the bottom boundary due to slip, we can use $(2u_{i+1}^n - u_{i+2}^n)$ to replace u_i^n because of the linear relationship between u_i^n, u_{i+1}^n and u_{i+2}^n.

With rearrangement, we get,

$$u_0^{n+1*} = (2u_1^n - u_2^n) + \frac{\Delta t}{3\rho\Delta y}(\sigma_1^n - \sigma_{bottom}{}^n). \tag{4.19}$$

Method 2 can also be applied to rough-rough walls. For rough-rough walls, the boundary condition at the bottom rough wall need to be modified to

$$u_i^{n+1*} = (\frac{2}{3}u_{i-0.5}^n + \frac{1}{3}u_{i+1}^n) + \frac{\Delta t}{3\rho\Delta y}(-\sigma_{i+1}^n + 9\sigma_i^n + 8\sigma_{bottom}{}^n). \tag{4.20}$$

When slip occurs, the microscopic role of EHD forces between soft particles and the smooth wall is still not clear. We have run simulations to investigate the effect of EHD forces by comparing the results using the equation of motion in Eq. 4.11 versus using a modified equation that includes EHD forces:

$$\frac{d\mathbf{x}_\alpha}{dt} = \mathbf{u}_\alpha = u_\infty \mathbf{e}_x + M_\alpha \sum_\beta (\mathbf{f}_{\alpha\beta}^{\text{elas}} + \mathbf{f}_{\alpha\beta}^{\text{EHD}}) \tag{4.21}$$

$$\mathbf{f}_{\alpha\beta}^{\text{EHD}} = -\left(\eta_S C u_{\alpha\beta,\|} E^* R_c^3\right)^{1/2} \varepsilon_{\alpha\beta}^{(2n+1)/4} \mathbf{n}_{\alpha\beta,\|} \tag{4.22}$$

where $\mathbf{n}_{\alpha\beta,\|} = \mathbf{u}_{\alpha\beta,\|} / \left|\mathbf{u}_{\alpha\beta,\|}\right|$ is a unit vector parallel to the relative velocity in the direction parallel to the contact surface, $\mathbf{u}_{\alpha\beta,\|}$, and other parameters with the same definition as Eq. 4.3. $\left|\mathbf{u}_{\alpha\beta,\|}\right|$ is also noted as $u_{\alpha\beta,\|}$.

The force $\mathbf{f}_{\alpha\beta}^{\text{EHD}}$ between the soft particles and the smooth wall uses the same equation as the forces between two soft particles, in the limit of one of the two particles going to an infinite radius.

4.2.3 Random particles stuck on smooth wall

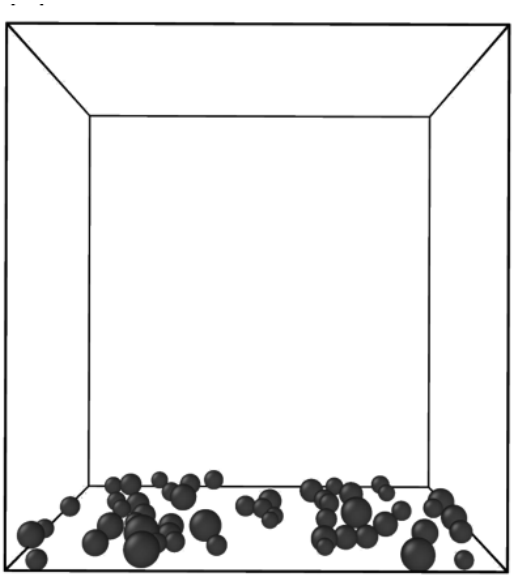

Figure 4.2: Illustration of random particles fixed at the bottom smooth wall with a stuck fraction of particles of 0.15

We developed a hypothetic model to explain the Stokes-like linear regime of V_{slip} and σ.

Similar to Figure 4.1b, soft particles are sheared between a moving top rough wall and a fixed bottom smooth wall. Soft particles move along the top wall since no slip occurs between soft particles and the top rough wall. When the top rough wall is moving at a large speed, some of the bottommost soft particles are pushed against the smooth wall in a random pattern as they move randomly relative to their neighboring soft particles. These random movements of bottommost particles, especially those in the *y* direction, disrupt the lubrication layer over the bottom smooth wall, causing temporary fixation of soft particles on the smooth wall. The viscous drag force of the soft particles F_{drag} over these temporary fixed spherical barriers can be scaled as the Stocks law,

$$F_{drag} = 6\pi\eta Rv, \tag{4.23}$$

where R is the size of the barrier, and v is the relative velocity between the fixed barrier particle and viscous fluid, in this case, other moving soft particles. Shear stress σ scales linearly with F_{drag}, and V_{slip} scales linearly with v, accounting for the linear relationship $V_{slip} \sim \sigma$.

For simpler implementation, a fixed random selection of barrier soft particles is chosen throughout each simulation. An example of a system including these barrier particles is shown in Figure 4.2 with a "stuck fraction" of 0.15, denoting 15% of soft particles that have interaction with the bottom wall. These barrier particles are viewed as being stuck to the bottom wall and are not allowed to move horizontally. Thus, their velocities in the x direction are set to 0.

4.3 RESULTS AND DISCUSSION

4.3.1 Rough-rough wall

Between two rough walls, two methods that divide the soft particles using horizontal bins are introduced in the method section. Their velocity and shear stress profiles are shown in Figure 4.3, with each symbol represents the average velocity or shear stress of soft particles from each horizontal bin. In both figures, there is minimal difference between the two methods.

Figure 4.3a clearly shows linear velocity profiles, with no slip occurring at both rough walls. Figure 4.3b shows a uniform stress profile across the y direction, as expected in the simulation. The profiles in Figure 4.3 are from the results of volume fraction 0.8 at an apparent shear rate of 10^{-5}. Profiles of other volume fractions at other shear rates are similar to Figure 4.3 and the values are presented in Figure 4.4.

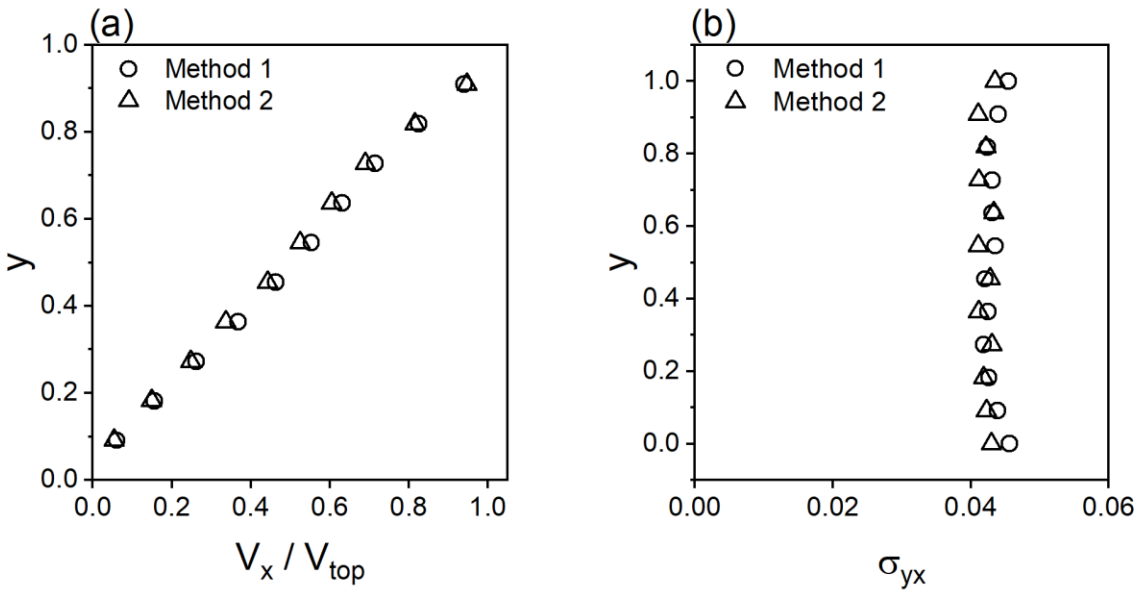

Figure 4.3: (a) Velocity profiles of soft particles sheared between two rough walls using the two methods, where V_{top} denotes the velocity of moving top wall. (b) Stress profiles of soft particles sheared between two rough walls using two methods.

Comparison of flow curves between two rough walls using the two methods and flow curves from corresponding bulk rheology is shown in Figure 4.4 for volume fractions 0.7, 0.8, and 0.9 at various shear rates. Figure 4.4 proves that the two methods have matching flow curves with bulk rheology, demonstrating the validity of both two methods between rough walls.

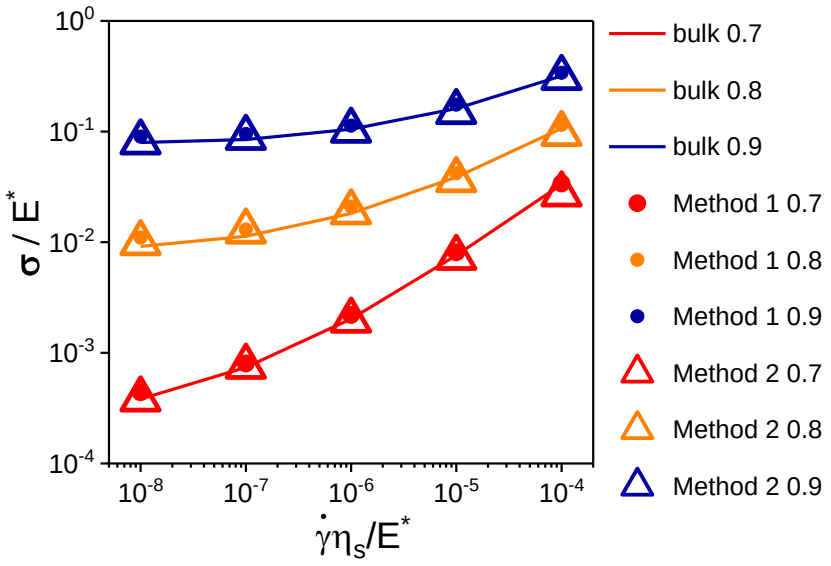

Figure 4.4: Flow curves of soft particles from bulk rheology (lines), when sheared between two rough walls using Method 1 (solid circle symbols), and Method 2 (empty triangle symbols) at volume fractions of 0.7 (red), 0.8 (yellow) and 0.9 (blue).

4.3.2 Rough-smooth wall

4.3.2.1 Effect of stuck fraction and the difference from rough-rough wall results.

Figures 4.5a and 4.5b show the velocity profiles and stress profiles of soft particles sheared between a rough wall and smooth wall with different stuck fractions. The particles are of volume fraction 0.8, being sheared at an apparent shear rate of 10^{-5}, where the apparent shear rate is defined as the velocity difference of two walls divided by the distance between them. To illustrate the isolated effect of stuck particles, no EHD forces are included in the simulations of this section.

Velocity profiles in Figure 4.5a clearly indicate that more stuck particles would discourage slip, causing the smooth wall with stuck particles to behave more like a complete rough wall. The velocity profile with a stuck fraction of 0 is a complete uniform velocity profile across y, the result of a complete plug flow where there exists zero fiction over the smooth wall. The velocity profile with a stuck fraction of 0.025 has only minor deviation from the result of a stuck fraction of 0. The velocity profile with a stuck fraction of 0.15, on the other hand, presents nearly no-slip, giving close results to a rough wall. The change from a stuck

fraction of 0.025 to a stuck fraction of 0.05 is the most outstanding among all the neighboring stuck fractions, revealing a drastic increase in the stuck particles' ability to preventing slip in this fraction range.

Stress profiles in Figure 4.5b exhibit results consistent with the velocity profiles mentioned above, showing larger stresses for simulations of larger stuck fractions, which have larger velocity gradients. The stresses are mostly uniform across all bins as expected from our simulation method. Values in different bins have relatively larger oscillations compared to results of rough - rough walls, causing the profiles of different stuck fractions not very well separated, in contrast with more separated velocity profiles in Figure 4.5a. These oscillations could be improved by averaging results of larger simulation systems with more particles and more bins, running longer simulations, and using more diverse random stuck configurations.

Both velocity profiles and stress profiles have minor artifacts in the bins near the smooth wall boundary: the stress is more deviated from the values of higher bins, and the velocity profile is not a completely straight line. The artifacts are mainly due to the special boundary conditions in the finite difference numerical method. Furthermore, stuck particles in the lowest bin are absolutely frozen and act as part of the bottom smooth wall, causing the effective bin thickness shrinking and motions of nearby mobile particles to be interfered by the barriers.

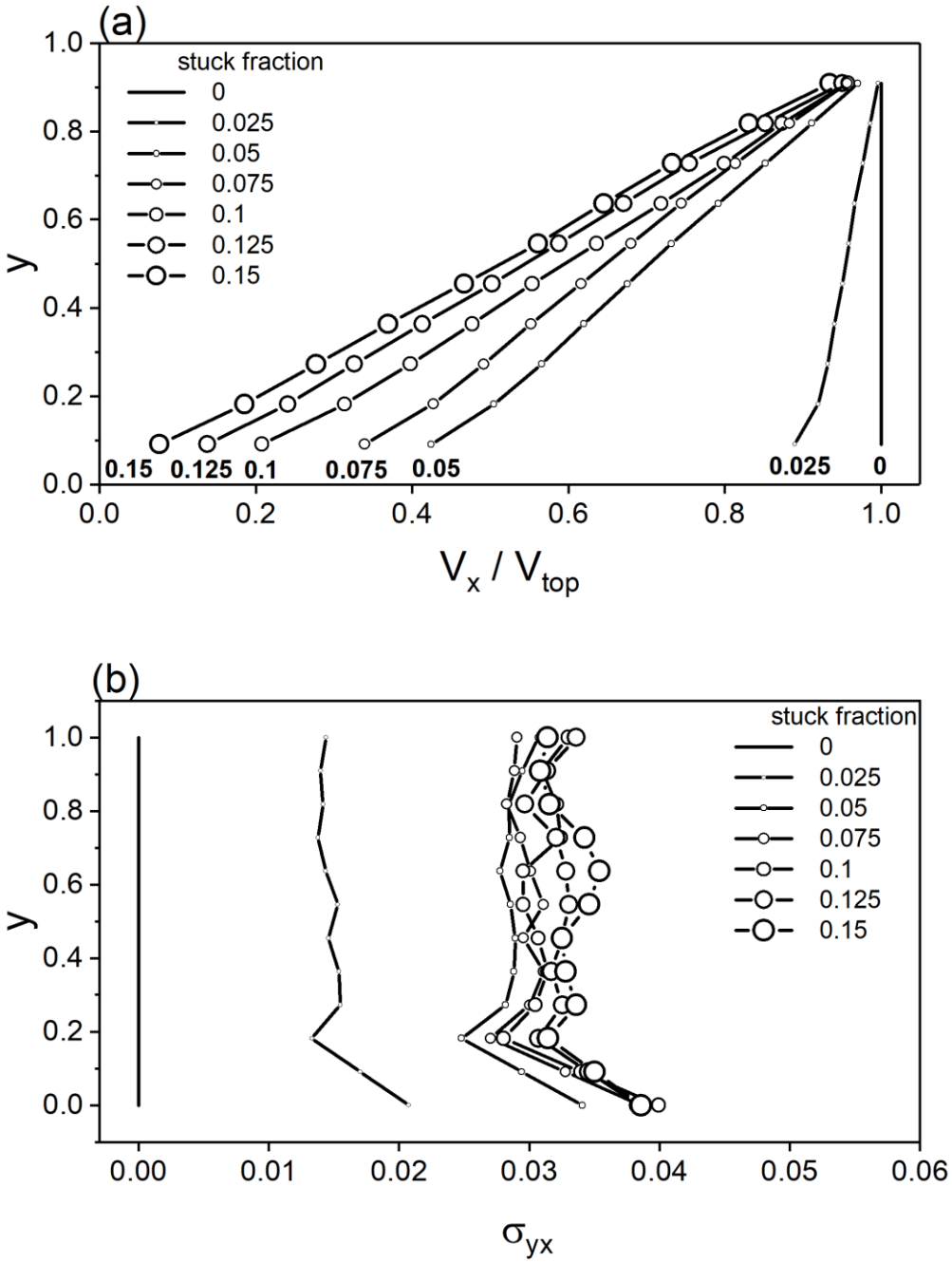

Figure 4.5: Velocity profiles (a) and stress profiles (b) of particles sheared between a rough wall and a smooth wall with different stuck fractions noted in the legend. (V_{top} is the velocity of the moving top wall; the volume fraction of moving particles is 0.8; the apparent shear rate is 10^{-5}; no EHD forces are included.)

4.3.2.2 Effect of shear rates

Figures 4.6a-d show the velocity profiles of soft particles sheared between a rough wall and a smooth wall with different stuck fractions. The particles are of volume fraction 0.8, being sheared at an apparent shear rate 5×10^{-7} to 10^{-5}. Similar to the last section, no EHD forces are included in the simulations of this section.

For all shear rates, results for a stuck fraction of 0 indicate complete plug flow, while results for a stuck fraction of 0.15 indicate a no-slip boundary condition, similar to a rough wall. Results of stuck fractions of 0.05 and 0.1 show variations among different shear rates, with the variations for a stuck fraction of 0.05 more noticeable compared to a stuck fraction of 0.1.

For both stuck fractions of 0.05 and 0.1, despite noises and oscillations, the trend is clear that the barrier effect is stronger for larger shear rate, with the slip velocity being smaller and the velocity profile appearing more like a straight line.

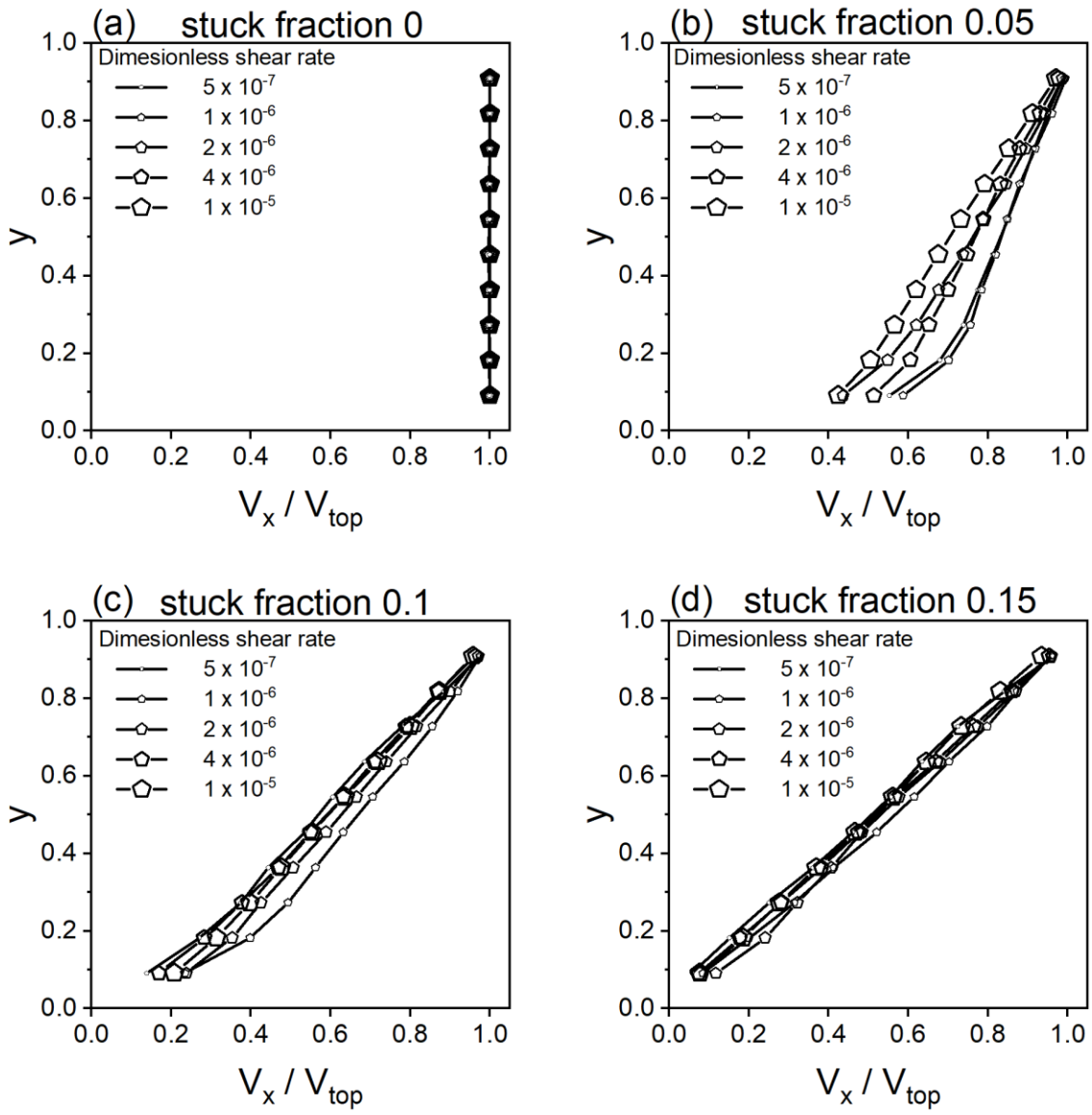

Figure 4.6: Velocity profiles of particles sheared between a rough wall and a smooth wall with stuck fractions of (a) 0, (b) 0.05, (c) 0.1, and (d) 0.15 at different apparent shear rates noted in the legend. (The volume fraction of moving particles is 0.8; no EHD forces are included.)

4.3.2.3 Effect of EHD force vs no EHD force.

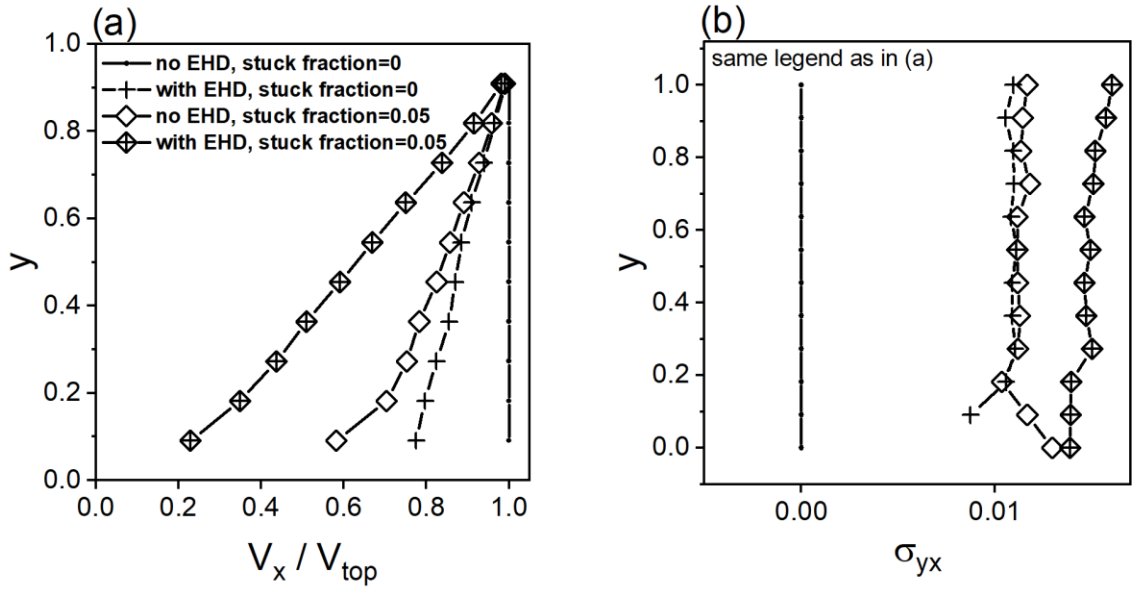

Figure 4.7: Velocity profiles (a) and stress profiles (b) of particles sheared between a rough wall and a smooth wall in four different settings: (1) no EHD forces and no stuck particles (dot symbol); (2) with EHD forces and no stuck particles (cross symbol); (3) no EHD forces and with a stuck fraction of 0.05 (diamond symbol); (4) with EHD forces and with a stuck fraction of 0.05 (diamond and cross symbol). (The volume fraction of moving particles is 0.8; the apparent shear rate is 10^{-6}.)

The comparison of EHD forces' effect and stuck particles' effect is illustrated by the velocity profiles and the stress profiles in Figure 4.7. With no EHD forces and no stuck fraction, velocities across all bins are the same as the velocity of the moving top rough wall, and the stresses are straight zero, the same as introduced in previous sections. With EHD forces and no stuck fraction, slip is inhibited, and its degree of slip inhibition is roughly equivalent to the case without EHD forces but with a stuck fraction of 0.05, where the two cases exhibit similar velocity and stress profiles. With both EHD forces and a stuck fraction of 0.05, both effects are composed into a stronger effect, and the velocity profile and stress profile deviate to larger degrees from those of total plug flow. Whether this composition is a linear composition needs more investigation.

4.3.2.4 Comparison with Experiment

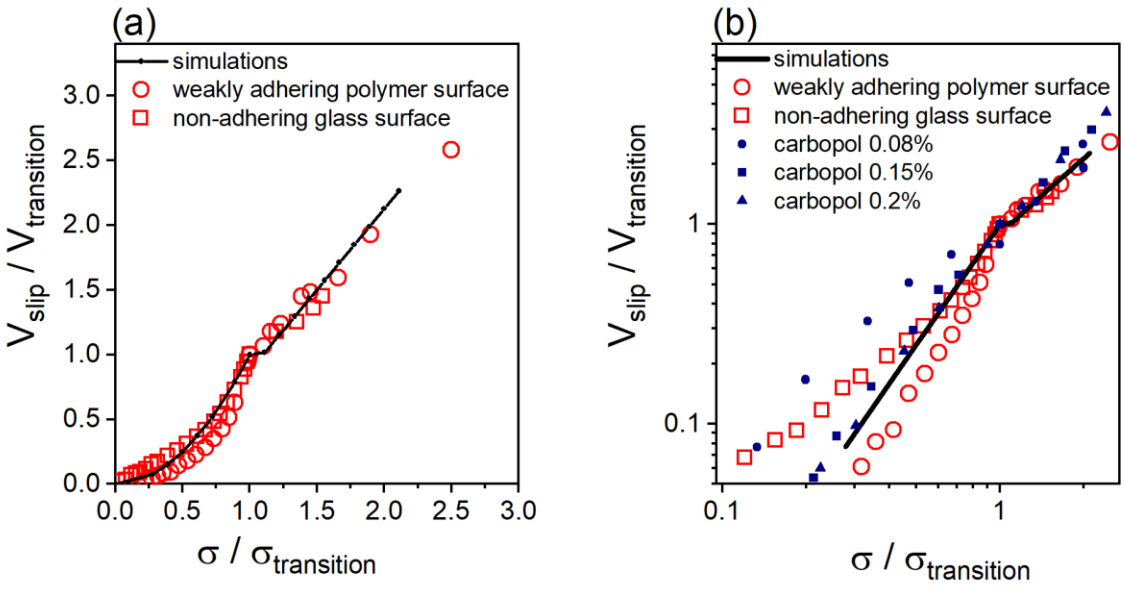

Figure 4.8: Comparison of simulation and corresponding experimental results of scaled slip velocity versus scaled stress when sheard between a rough surface and a smooth surface in linear scale (a) and logarithmic scale (b). The volume fraction used in the simulations (black lines) is 0.8. Experimental results in red symbols in both Figure 4.8a and 4.8b are results of concentrated silicone oil emulsions from research work by Seth *et al.* (Seth et al., 2012) when sheared between a rough surface and a smooth surface. Red circles and red squares are different smooth surface materials as noted in the legend. Blue symbols in Figure 4.8b denotes experimental results by Pemeja *et al.* (Péméja, Géraud, Barentin, & Le Merrer, 2019) on different concentrations of Carbopol microgels.

In Figures 4.8a-b, the slip velocity versus stress profiles show clearly two regimes: a parabolic nonlinear regime at low shear rates, and a linear regime at high shear rates. The turning point between the linear and the nonlinear regime is noted as the transition point, and the slip velocity and stress at the transition point separating the two regimes are noted as $V_{transition}$ and $\sigma_{transition}$. In experimental work by Seth *et al.* (Seth et al., 2012) (red symbols), $\sigma_{transition}$ is the same as the yielding stress of the soft particle material, and the transition between the two regimes is strictly well-separated. In contrast, in experimental work by Pemeja *et al.* (Péméja et al., 2019) (blue symbols), the transition is more obscure and doesn't coincide with yielding stress, and they have used a sum of both a nonlinear term and linear term in their model to depict this obscure transition and fit their data. Both slip velocity and stress are scaled

using the transitional value for more consistent comparison between results from different settings.

In the simulations, before the transition point, EHD forces are included without stuck particles; after the transition point, EHD forces are included with stuck particle fraction 0.01. Stuck particle fraction 0.01 is selected to match the results from the experiment. In both Figure 4.8a and Figure 4.8b, the experimental data are in good agreement with our simulation results. This agreement proves the possible validity of our proposed model with fixed particles, which depicts that the microscopic origin of the Stokes-like linear regime might be due to the temporary adhering of random particles to the smooth surface.

4.4 CONCLUSIONS

In summary, we have developed two generic frameworks for simulating shear between walls, method 1 and method 2. Both methods divide the simulation box into horizontal bins for horizontal flows in the *x* direction. Since the macroscopic values such as stresses and velocities should theoretically be constant with the *x* direction and only vary with the *y* direction, these values are averaged for each horizontal bin for each iteration of the simulation. Like all finite element methods, larger simulation systems with more element density would generate more accurate results.

Method 1 uses the idea that stresses should be constant in the vertical direction for horizontal flows, and uses the definition of viscosity assuming linear relationship as Newton's law within infinitesimal distances. Method 2 introduces the dimension of time and uses the relationship between stress and velocity for low Reynolds number flow, and updates the stresses and velocities of each bin after small time steps.

Both methods work well for the case of shear between rough-rough walls, and the results are the same as that of bulk rheology. The role of EHD forces is negligible in this rough-rough wall case, similar to the conclusion for bulk rheology.

Method 2 works for the case of shear between rough-smooth walls. Including EHD forces between soft particles and a smooth wall leads to the parabolic relationship between slip

velocity and slip stress, but can't explain the linear regime with slower shear and smaller slip stress. We propose a mechanism that includes the temporary fixation of randomly selected soft particles on the smooth wall, and this gives results of a linear relationship between slip velocity and slip stress. We investigate the role of stuck fraction in this model and concludes that 15% percent of particles stuck to the smooth wall would be enough to prevent slip from happening and make the smooth wall behave like a rough wall. The inclusion of EHD force (between particle and smooth wall) and stuck particles both reduces the slip velocity; the quantitative comparison and whether their effects can be linearly added needs further research.

Chapter 5: Conclusions and Future Work

5.1 Conclusions

Three aspects of SPGs are investigated using computational simulations developed based on a pairwise theory.

In Chapter 2, we show the universal form of the flow curve for SPGs with different pairwise elastic and frictional forces. We identify two kinds of forces as minimal ingredients to predict the simulations of SPGs: viscous or frictional drag forces and elastic contact forces. The shear stress, the first and second normal stress differences for different interparticle force laws collapse onto universal master curves of the Herschel–Bulkley form by non-dimensionalizing the stress with the yield stress and the shear rate with the viscosity of the suspending fluid divided by the low-frequency shear modulus. The Herschel–Bulkley exponents are close to 0.5 with a slight dependence on the repulsive pairwise elastic forces.

In Chapter 3, we study the behavior of the storage and loss moduli for SPGs. The storage modulus follows a universal sigmoidal rule which varies with frequency. While the high frequency modulus G_∞ follows the prediction of the Zwanzig- Mountain formula, which depends on the pair distribution function and interparticle potential, no such formula exists for the low frequency modulus G_0. Here, we show that for jammed soft particles at a given volume fraction $G_0 \sim G_\infty / g_{max}$, where g_{max} is the maximum in the pair distribution function. For a given drag force law, the loss moduli also follow a universal function of the frequency with the appropriate non-dimensionalization. Predictions from the computational simulations match available data in the literature.

In Chapter 4, we have developed two generic frameworks for simulating shear between walls. Both methods divide the simulation box into horizontal bins for horizontal flows in the x direction. Both methods work well for the case of shear between rough-rough walls, and the results are the same as that of bulk rheology. The role of EHD forces is negligible in this rough-rough wall case, similar to the conclusion for bulk rheology. The second method works for the case of shear between rough-smooth walls. Including EHD forces between the soft particles

and the smooth wall can't explain the linear regime with slower shear and smaller slip stress. We propose a mechanism that includes the temporary fixation of randomly selected soft particles on the smooth wall, and this gives results of the linear relationship between slip velocity and slip stress. We investigate the role of stuck fraction in this model and conclude that 15% percent of particles stuck to the smooth wall would be enough to prevent slip from happening and make the smooth wall behave like a rough wall. The inclusion of EHD force (between soft particles and the smooth wall) and stuck particles both reduces the slip velocity.

5.2 FUTURE WORK

For future work, a lot of interesting questions still remain open in the wall slip field. For example, how will the attractive or repulsive forces between soft particles and the wall affect the rheological behavior near the wall? What about other properties of the wall, such as the shape of the wall's roughness? Will the microstructure near the wall reflect related differences for different situations? How will the macroscopic parameters correlate with different cases quantitatively? More simulation work can be done using the simulation framework introduced by this dissertation. The following introduces a few ideas which could be explored in future work.

5.2.1 SPGs-wall interaction

The force between SPGs and wall particles can be attractive or repulsive depending on different chemistry (Seth et al., 2008). As one basic example, the added interaction potential could be set to:

$$U = Ce^{\pm r/r^*}, \tag{5.1}$$

where C is the coefficient, r is the distance between a wall particle and an SPG particle, and r^* is the characteristic distance. The sign of the exponent depends on whether the interaction is attractive or repulsive. As another example, the attractive force model to use is the JKR force model developed by Johnson, Kendall, and Roberts (Johnson, Kendall, & Roberts, 1971). This adhesion arises fundamentally from the short-range interaction between molecules:

$$\mathbf{f}_{\alpha\beta}^{\mathrm{JKR}} = C_{\mathrm{JKR}} \pi E^{*} R_c^2 f\left(\varepsilon_{\alpha,\beta}^{\mathrm{JKR}}\right) \mathbf{n}_{\perp}, \tag{5.2}$$

where $C_{\mathrm{JKR}} = w/R_c E^{*}$ and w is the adhesion work (Israelachvili, 2011). The relationship between the overlap distance and force is implicit, so nondimensional JKR force $f\left(\varepsilon_{\alpha,\beta}^{\mathrm{JKR}}\right)$ is obtained numerically and fitted with nondimensional overlap distance.

5.2.2 Characterization of wall roughness and its impact

A modified version of the framework between rough-smooth walls with stuck particles proposed in Chapter 4 can be used to study the impact of wall roughness. In this modified version, the stuck particles are no longer randomly selected soft particles from the suspension. Instead, the size of SPGs particles and how to place them on the ideal wall are accurately controlled. Important variable parameters of placing stuck particles include the height and distance of the stuck particles. Placing variations in the *y*-direction the *z*-direction could both have an impact.

Besides, in characterizing wall roughness, several other schemes of roughness can be proposed by directly changing the shape of the wall, and the hints come from previous literature.

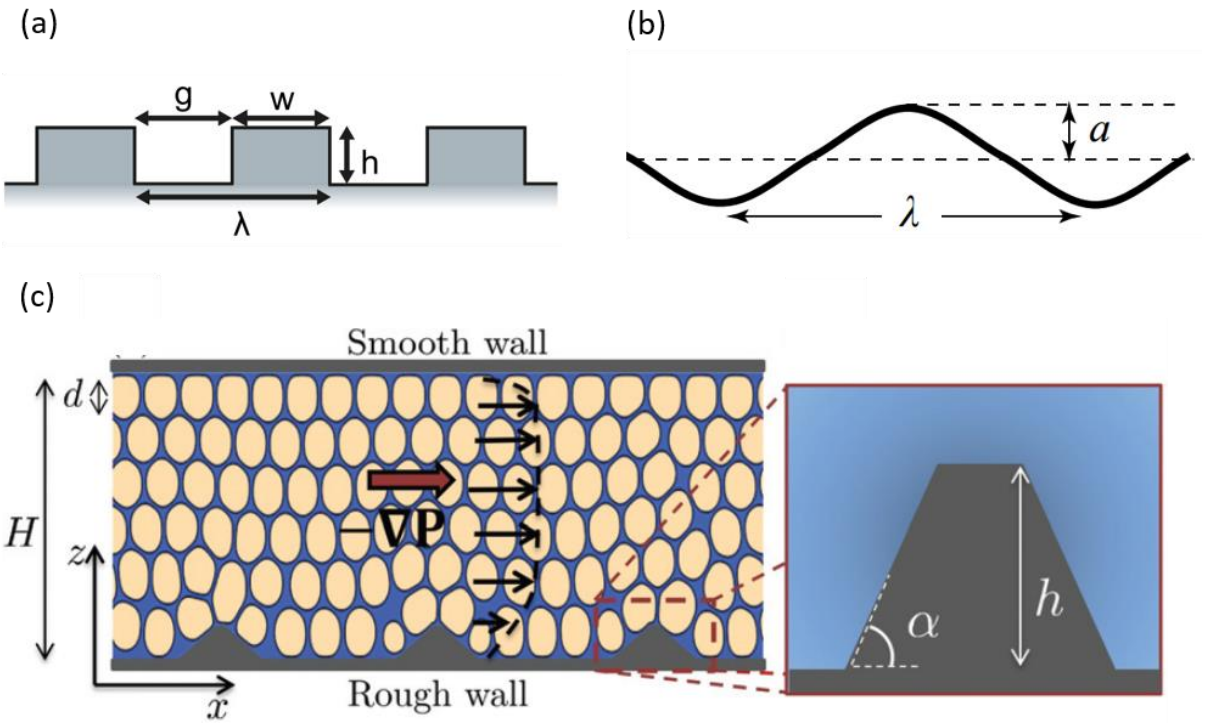

Figure 5.1: (a) rectangular rough pattern with equally spaced grooves (Derzsi et al., 2017); (b) sinusoidal wavy rough pattern (Jabbarzadeh, Atkinson, & Tanner, 2000); (c) trapezoidal pattern with equally spaced posts of trapezoidal shape (Pelusi et al., 2019).

The first one is a rectangular rough pattern with equally spaced grooves shown in Figure 5.1a, same as the experiment work done by Derzsi et al. in which they studied fluidization and wall slip of concentrated emulsions by controlling surface roughness in a confined microfluidic channel (Derzsi et al., 2017). They have found a scaling law describing fluidization as the density of grooves. The basic parameters to characterize the wall include periodic length λ, groove height h, gap g, and width w.

The second scheme is to use a sinusoidal wavy wall as shown in Figure 5.1b. This is a classical way of characterizing wall roughness used by many previous research works because of its simplicity (Jabbarzadeh et al., 2000; Priezjev & Troian, 2006). This method has only two parameters including wavelength λ and amplitude a. The sinusoidal shape makes it possible to compare simulation results with theoretical analysis and prediction.

The third scheme in Figure 5.1c was previously explored by Pelusi et al. to evaluate the impact of controlled wall roughness on the flow of soft materials using a lattice-Boltzmann

numerical simulation of pressure-driven flow between a smooth wall and rough wall. This scheme allows more flexible control of the shape of equally spaced posts on the rough wall compared to the rectangular pattern and introduces more free parameters including angle α as in the enlarged picture in Figure 5.1c.

5.2.3 Characterization of microstructure near the wall

Two of the useful tools to analyze the microstructure are the average particle velocity fluctuations and pair distribution function. The pair distribution function *g(r)* describes how density varies as a function of distance from a reference particle. *g(r)* can be decomposed into an orthogonal series of spherical harmonic functions (Hanley, Rainwater, & Hess, 1987; Morris & Katyal, 2002) to quantify the distortion and asymmetry in the microstructure.

References

Agoritsas, E., & Martens, K. (2017). Non-trivial rheological exponents in sheared yield stress fluids. *Soft Matter, 13*(26), 4653-4660.

Athanasiou, T., Auernhammer, G. K., Vlassopoulos, D., & Petekidis, G. (2019). A high-frequency piezoelectric rheometer with validation of the loss angle measuring loop: application to polymer melts and colloidal glasses. *Rheologica Acta, 58*(9), 619-637.

Bahnemann, D. (2004). Photocatalytic water treatment: solar energy applications. *Solar energy, 77*(5), 445-459.

Ballesta, P., Besseling, R., Isa, L., Petekidis, G., & Poon, W. (2008). Slip and flow of hard-sphere colloidal glasses. *Physical Review Letters, 101*(25), 258301.

Ballesta, P., Koumakis, N., Besseling, R., Poon, W. C., & Petekidis, G. (2013). Slip of gels in colloid–polymer mixtures under shear. *Soft Matter, 9*(12), 3237-3245.

Ballesta, P., Petekidis, G., Isa, L., Poon, W., & Besseling, R. (2012). Wall slip and flow of concentrated hard-sphere colloidal suspensions. *Journal of Rheology, 56*(5), 1005-1037.

Basu, A., Xu, Y., Still, T., Arratia, P., Zhang, Z., Nordstrom, K., . . . Yodh, A. (2014). Rheology of soft colloids across the onset of rigidity: scaling behavior, thermal, and non-thermal responses. *Soft Matter, 10*(17), 3027-3035.

Beatrice, C. A., Rosa-Sibakov, N., Lille, M., Sözer, N., Poutanen, K., & Ketoja, J. A. (2017). Structural properties and foaming of plant cell wall polysaccharide dispersions. *Carbohydrate Polymers, 173*, 508-518.

Becu, L., Manneville, S., & Colin, A. (2006). Yielding and flow in adhesive and nonadhesive concentrated emulsions. *Physical Review Letters, 96*(13), 138302.

Berryman, J. G. (1983). Random close packing of hard spheres and disks. *Physical Review A, 27*(2), 1053-1061.

Bertsch, P., & Fischer, P. (2020). Adsorption and interfacial structure of nanocelluloses at fluid interfaces. *Advances in Colloid and Interface Science, 276*, 102089.

Bhattacharjee, T., & Angelini, T. E. (2018). 3D T cell motility in jammed microgels. *Journal of Physics D: Applied Physics, 52*(2), 024006.

Bocquet, L., Colin, A., & Ajdari, A. (2009). Kinetic Theory of Plastic Flow in Soft Glassy Materials. *Physical Review Letters, 103*(3), 036001.

Bonn, D., Denn, M. M., Berthier, L., Divoux, T., & Manneville, S. (2017). Yield stress materials in soft condensed matter. *Reviews of Modern Physics, 89*(3), 035005.

Bonnecaze, R. T., & Cloitre, M. (2010). Micromechanics of Soft Particle Glasses. *Advances in Polymer Science, 236*, 117-161. doi:10.1007/12_2010_90

Brady, J. F. (1994). The long-time self-diffusivity in concentrated colloidal dispersions. *Journal of Fluid Mechanics, 272*, 109-134.

Bysell, H., Månsson, R., Hansson, P., & Malmsten, M. (2011). Microgels and microcapsules in peptide and protein drug delivery. *Advanced drug delivery reviews, 63*(13), 1172-1185.

Caggioni, M., Trappe, V., & Spicer, P. T. (2020). Variations of the Herschel–Bulkley exponent reflecting contributions of the viscous continuous phase to the shear rate-dependent stress of soft glassy materials. *Journal of Rheology, 64*(2), 413-422.

Chaudhuri, P., Berthier, L., & Bocquet, L. (2012). Inhomogeneous shear flows in soft jammed materials with tunable attractive forces. *Physical Review E, 85*(2), 021503. doi:10.1103/PhysRevE.85.021503

Cloitre, M., & Bonnecaze, R. T. (2017). A review on wall slip in high solid dispersions. *Rheologica Acta, 56*(3), 283-305. doi:10.1007/s00397-017-1002-7

Cloitre, M., Borrega, R., Monti, F., & Leibler, L. (2003). Glassy dynamics and flow properties of soft colloidal pastes. *Physical Review Letters, 90*(6), 068303. doi:10.1103/PhysRevLett.90.068303

Corma, A., Concepción, P., & Serna, P. (2007). A different reaction pathway for the reduction of aromatic nitro compounds on gold catalysts. *Angewandte Chemie International Edition, 46*(38), 7266-7269.

Dagallier, C., Cardinaux, F., Dietsch, H., & Scheffold, F. (2012). Magnetic orientation of soft particles in a jammed solid. *Soft Matter, 8*(15), 4067-4071.

Dang, P. N., Herberg, S., Varghai, D., Riazi, H., Varghai, D., McMillan, A., . . . Nguyen, M. K. (2017). Endochondral ossification in critical ‐ sized bone defects via readily implantable scaffold ‐ free stem cell constructs. *Stem cells translational medicine, 6*(7), 1644-1659.

de Lima, C. S., Balogh, T. S., Varca, J. P., Varca, G. H., Lugão, A. B., A Camacho-Cruz, L., . . . Kadlubowski, S. S. (2020). An Updated Review of Macro, Micro, and Nanostructured Hydrogels for Biomedical and Pharmaceutical Applications. *Pharmaceutics, 12*(10), 970.

Denkov, N. D., Tcholakova, S., Golemanov, K., Ananthapadmanabhan, K. P., & Lips, A. (2008). Viscous Friction in Foams and Concentrated Emulsions under Steady Shear. *Physical Review Letters, 100*(13), 138301.

Derzsi, L., Filippi, D., Mistura, G., Pierno, M., Lulli, M., Sbragaglia, M., . . . Garstecki, P. (2017). Fluidization and wall slip of soft glassy materials by controlled surface roughness. *Physical Review E, 95*(5). doi:10.1103/PhysRevE.95.052602

Dickinson, E. (2015). Structuring of colloidal particles at interfaces and the relationship to food emulsion and foam stability. *Journal of Colloid and Interface Science, 449,* 38-45.

Dinkgreve, M., Paredes, J., Michels, M., & Bonn, D. (2015). Universal rescaling of flow curves for yield-stress fluids close to jamming. *Physical Review E, 92*(1), 012305.

Durian, D. J. (1995). Foam mechanics at the bubble scale. *Physical Review Letters, 75*(26), 4780-4783. doi:10.1103/PhysRevLett.75.4780

Durian, D. J. (1997). Bubble-scale model of foam mechanics:mMelting, nonlinear behavior, and avalanches. *Physical Review E, 55*(2), 1739-1751.

Erwin, B. M., Cloitre, M., Gauthier, M., & Vlassopoulos, D. (2010). Dynamics and rheology of colloidal star polymers. *Soft Matter, 6*(12), 2825-2833. doi:10.1039/b926526k

Eswaramma, S., Reddy, N. S., & Rao, K. K. (2017). Carbohydrate polymer based pH-sensitive IPN microgels: Synthesis, characterization and drug release characteristics. *Materials Chemistry and Physics, 195,* 176-186.

Fritz, G., Pechhold, W., Willenbacher, N., & Wagner, N. J. (2003). Characterizing complex fluids with high frequency rheology using torsional resonators at multiple frequencies. *Journal of Rheology, 47*(2), 303-319.

Fusco, C., Albaret, T., & Tanguy, A. (2014). Rheological properties vs. local dynamics in model disordered materials at low temperature. *European Physical Journal E, 37*(5), 43.

Gao, W., Guan, N., Chen, J., Guan, X., Jin, R., Zeng, H., . . . Zhang, F. (2003). Titania supported Pd-Cu bimetallic catalyst for the reduction of nitrate in drinking water. *Applied Catalysis B: Environmental, 46*(2), 341-351.

Gong, J., Iwasaki, Y., Osada, Y., Kurihara, K., & Hamai, Y. (1999). Friction of gels. 3. Friction on solid surfaces. *Journal of Physical Chemistry B, 103*(29), 6001-6006.

Gross, M., Krüger, T., & Varnik, F. (2014). Rheology of dense suspensions of elastic capsules: normal stresses, yield stress, jamming and confinement effects. *Soft Matter, 10*(24), 4360-4372.

Gupta, V. K., Jain, R., Mittal, A., Saleh, T. A., Nayak, A., Agarwal, S., & Sikarwar, S. (2012). Photo-catalytic degradation of toxic dye amaranth on TiO2/UV in aqueous suspensions. *Materials Science and Engineering: C, 32*(1), 12-17.

Hanley, H. J. M., Rainwater, J. C., & Hess, S. (1987). Shear-Induced Angular-Dependence of the Liquid Pair Correlation-Function. *Physical Review A, 36*(4), 1795-1802. doi:10.1103/PhysRevA.36.1795

Hatzikiriakos, S. G. (2015). Slip mechanisms in complex fluid flows. *Soft Matter, 11*(40), 7851-7856.

Hébraud, P., & Lequeux, F. (1998). Mode-Coupling Theory for the Pasty Rheology of Soft Glassy Materials. *Physical Review Letters, 81*(14), 2934-2937.

Highley, C. B., Song, K. H., Daly, A. C., & Burdick, J. A. (2019). Jammed microgel inks for 3D printing applications. *Advanced Science, 6*(1), 1801076.

Hipfinger, C., Subbiah, R., Tahayeri, A., Athirasala, A., Horsophonphong, S., Thrivikraman, G., . . . Zahariev, A. (2020). 3D printing of microgel-loaded modular LEGO-like cages as instructive scaffolds for tissue engineering. *bioRxiv*.

Hyun, K., Wilhelm, M., Klein, C. O., Cho, K. S., Nam, J. G., Ahn, K. H., . . . McKinley, G. H. (2011). A review of nonlinear oscillatory shear tests: Analysis and application of large amplitude oscillatory shear (LAOS). *Progress in Polymer Science, 36*(12), 1697-1753.

Israelachvili, J. N. (2011). 17 - Adhesion and Wetting Phenomena *Intermolecular and Surface Forces (Third Edition)* (pp. 415-467). San Diego: Academic Press.

Jabbarzadeh, A., Atkinson, J. D., & Tanner, R. I. (2000). Effect of the wall roughness on slip and rheological properties of hexadecane in molecular dynamics simulation of Couette shear flow between two sinusoidal walls. *Physical Review E, 61*(1), 690-699. doi:10.1103/PhysRevE.61.690

Jeon, O., Lee, Y. B., Hinton, T. J., Feinberg, A. W., & Alsberg, E. (2019). Cryopreserved cell-laden alginate microgel bioink for 3D bioprinting of living tissues. *Materials Today Chemistry, 12*, 61-70.

Johnson, K. L., Kendall, K., & Roberts, A. D. (1971). Surface Energy and the Contact of Elastic Solids. *Proceedings of the Royal Society of London. A. Mathematical and Physical Sciences, 324*(1558), 301-313. doi:10.1098/rspa.1971.0141

Jooybar, E., Abdekhodaie, M. J., Mousavi, A., Zoetebier, B., & Dijkstra, P. J. (2019). Enzymatically crosslinked hyaluronic acid microgels as a vehicle for sustained delivery of cationic proteins. *European Polymer Journal, 115*, 234-243.

Joseph, D. D. (1997). Lubricated pipelining. *Powder Technology, 94*(3), 211-215. doi:10.1016/S0032-5910(97)03296-8

Joseph, D. D., Bai, R., Chen, K. P., & Renardy, Y. Y. (1997). Core-annular flows. *Annual Review of Fluid Mechanics, 29*, 65-90. doi:10.1146/annurev.fluid.29.1.65

Jungst, T., Smolan, W., Schacht, K., Scheibel, T., & Groll, J. r. (2016). Strategies and molecular design criteria for 3D printable hydrogels. *Chemical Reviews, 116*(3), 1496-1539.

Khabaz, F., Cloitre, M., & Bonnecaze, R. T. (2018). Structural state diagram of concentrated suspensions of jammed soft particles in oscillatory shear flow. *Physical Review Fluids, 3*(3), 033301.

Khabaz, F., Liu, T., Cloitre, M., & Bonnecaze, R. T. (2017). Shear-induced ordering and crystallization of jammed suspensions of soft particles glasses. *Physical Review Fluids, 2*(9), 093301.

Lacasse, M. D., Grest, G. S., Levine, D., Mason, T. G., & Weitz, D. A. (1996). Model for the elasticity of compressed emulsions. *Physical Review Letters, 76*(18), 3448-3451. doi:10.1103/PhysRevLett.76.3448

Langer, J. S. (2015). Shear-transformation-zone theory of yielding in athermal amorphous materials. *Physical Review E, 92*(1), 012318.

Langlois, V. J., Hutzler, S., & Weaire, D. (2008). Rheological properties of the soft-disk model of two-dimensional foams. *Physical Review E, 78*(2), 021401.

Larson, R. (1997). The elastic stress in "film fluids". *Journal of Rheology, 41*(2), 365-372.

Larson, R. G. (1999). *The structure and rheology of complex fluids*. New York: Oxford University Press.

Lemaître, A., & Caroli, C. (2009). Rate-Dependent Avalanche Size in Athermally Sheared Amorphous Solids. *Physical Review Letters, 103*(6), 065501.

Lin, J., Lerner, E., Rosso, A., & Wyart, M. (2014). Scaling description of the yielding transition in soft amorphous solids at zero temperature. *Proceedings of the National Academy of Sciences of the United States of America, 111*(40), 14382-14387.

Lin, J., & Wyart, M. (2018). Microscopic processes controlling the Herschel-Bulkley exponent. *Physical Review E, 97*(1), 012603. doi:10.1103/PhysRevE.97.012603

Lionberger, R., & Russel, W. (1994). High frequency modulus of hard sphere colloids. *Journal of Rheology, 38*(6), 1885-1908.

Liu, A. J., Ramaswamy, S., Mason, T., Gang, H., & Weitz, D. (1996). Anomalous viscous loss in emulsions. *Physical Review Letters, 76*(16), 3017.

Liu, K. K., Williams, D. R., & Briscoe, B. J. (1998). The large deformation of a single micro-elastomeric sphere. *Journal of Physics D-Applied Physics, 31*(3), 294-303. doi:10.1088/0022-3727/31/3/008

Liu, T., Khabaz, F., Bonnecaze, R. T., & Cloitre, M. (2018). On the universality of the flow properties of soft-particle glasses. *Soft Matter, 14*(34), 7064-7074.

Lopez, V. C., Hadgraft, J., & Snowden, M. (2005). The use of colloidal microgels as a (trans) dermal drug delivery system. *International Journal of Pharmaceutics, 292*(1-2), 137-147.

Lubachevsky, B. D., & Stillinger, F. H. (1990). Geometric-Properties of Random Disk Packings. *Journal of Statistical Physics, 60*(5-6), 561-583. doi:10.1007/Bf01025983

Malkin, A. Y., & Patlazhan, S. (2018). Wall slip for complex liquids–Phenomenon and its causes. *Advances in Colloid and Interface Science, 257*, 42-57.

Mansard, V., Colin, A., Chaudhuri, P., & Bocquet, L. (2013). A molecular dynamics study of non-local effects in the flow of soft jammed particles. *Soft Matter, 9*(31), 7489-7500. doi:10.1039/c3sm50847a

Mason, T. G., & Weitz, D. (1995). Optical measurements of frequency-dependent linear viscoelastic moduli of complex fluids. *Physical Review Letters, 74*(7), 1250.

Matsumoto, A., Ishii, T., Nishida, J., Matsumoto, H., Kataoka, K., & Miyahara, Y. (2012). A synthetic approach toward a self‐regulated insulin delivery system. *Angewandte Chemie International Edition, 51*(9), 2124-2128.

Meeker, S. P., Bonnecaze, R. T., & Cloitre, M. (2004). Slip and flow in pastes of soft particles: Direct observation and rheology. *Journal of Rheology, 48*(6), 1295-1320. doi:10.1122/1.1795171

Meeker, S. P., Bonnecaze, R. T., & Cloitre, M. (2004). Slip and flow in soft particle pastes. *Physical Review Letters, 92*(19), 198302.

Mohammadian, M., & Madadlou, A. (2018). Technological functionality and biological properties of food protein nanofibrils formed by heating at acidic condition. *Trends in Food Science & Technology, 75*, 115-128.

Mohan, L. (2013). *Microstructure and rheology of soft particle glasses.* (Dissertation/Thesis).

Mohan, L., & Bonnecaze, R. T. (2012). Short-ranged pair distribution function for concentrated suspensions of soft particles. *Soft Matter, 8*(15), 4216-4222.

Mohan, L., Bonnecaze, R. T., & Cloitre, M. (2013). Microscopic Origin of Internal Stresses in Jammed Soft Particle Suspensions. *Physical Review Letters, 111*(26), 268301.

Mohan, L., Cloitre, M., & Bonnecaze, R. T. (2015). Build-up and two-step relaxation of internal stress in jammed suspensions. *Journal of Rheology, 59*(1), 63-84. doi:10.1122/1.4901750

Mohan, L., Pellet, C., Cloitre, M., & Bonnecaze, R. (2013). Local mobility and microstructure in periodically sheared soft particle glasses and their connection to macroscopic rheology. *Journal of Rheology, 57*(3), 1023-1046.

Monti, F. (2010). Microrheology of non-ergodic colloidal suspensions: local relaxations, slow dynamics and aging. 131.

Moroni, L., Burdick, J. A., Highley, C., Lee, S. J., Morimoto, Y., Takeuchi, S., & Yoo, J. J. (2018). Biofabrication strategies for 3D in vitro models and regenerative medicine. *Nature Reviews Materials, 3*(5), 21-37.

Morris, J. F., & Katyal, B. (2002). Microstructure from simulated Brownian suspension flows at large shear rate. *Physics of Fluids, 14*(6), 1920-1937. doi:10.1063/1.1476745

Murray, B. S. (2019). Pickering emulsions for food and drinks. *Current Opinion in Food Science, 27*, 57-63.

Murray, B. S. (2020). Recent developments in food foams. *Current Opinion in Colloid & Interface Science, 50*. doi:10.1016/j.cocis.2020.101394

Nicolas, A., & Barrat, J. L. (2013). Spatial Cooperativity in Microchannel Flows of Soft Jammed Materials: A Mesoscopic Approach. *Physical Review Letters, 110*(13), 44003.

Nicolas, A., Martens, K., & Barrat, J.-L. (2014). Rheology of athermal amorphous solids: Revisiting simplified scenarios and the concept of mechanical noise temperature. *EPL (Europhysics Letters), 107*(4), 44003.

Nordstrom, K. N., Verneuil, E., Arratia, P. E., Basu, A., Zhang, Z., Yodh, A. G., . . . Durian, D. J. (2010). Microfluidic Rheology of Soft Colloids above and below Jamming. *Physical Review Letters, 105*(17), 175701. doi:10.1103/PhysRevLett.105.175701

O'Hern, C. S., Silbert, L. E., Liu, A. J., & Nagel, S. R. (2003). Jamming at zero temperature and zero applied stress: The epitome of disorder. *Physical Review E, 68*(1), 011306.

Olsson, P., & Teitel, S. (2011). Critical scaling of shearing rheology at the jamming transition of soft-core frictionless disks. *Physical Review E, 83*(3), 030302.

Olsson, P., & Teitel, S. (2012). Herschel-Bulkley Shearing Rheology Near the Athermal Jamming Transition. *Physical Review Letters, 109*(10), 108001. doi:10.1103/PhysRevLett.109.108001

Paredes, J., Michels, M. A. J., & Bonn, D. (2013). Rheology across the Zero-Temperature Jamming Transition. *Physical Review Letters, 111*(1), 015701.

Pellet, C., & Cloitre, M. (2016). The glass and jamming transitions of soft polyelectrolyte microgel suspensions. *Soft Matter, 12*(16), 3710-3720. doi:10.1039/c5sm03001c

Pelusi, F., Sbragaglia, M., Scagliarini, A., Lulli, M., Bernaschi, M., & Succi, S. (2019). On the impact of controlled wall roughness shape on the flow of a soft material. *EPL (Europhysics Letters), 127*(3), 34005.

Péméja, J., Géraud, B., Barentin, C., & Le Merrer, M. (2019). Wall slip regimes in jammed suspensions of soft microgels. *Physical Review Fluids, 4*(3), 033301.

Peng, D., Jin, W., Tang, C., Lu, Y., Wang, W., Li, J., & Li, B. (2018). Foaming and surface properties of gliadin nanoparticles: Influence of pH and heating temperature. *Food Hydrocolloids, 77*, 107-116.

Phillips, R., Brady, J., & Bossis, G. (1988). Hydrodynamic transport properties of hard ‐ sphere dispersions. I. Suspensions of freely mobile particles. *Physics of Fluids, 31*(12), 3462-3472.

Plazek, D. J. (1996). 1995 Bingham Medal Address: Oh, thermorheological simplicity, wherefore art thou? *Journal of Rheology, 40*(6), 987-1014.

Plimpton, S. (1995). Fast Parallel Algorithms for Short-Range Molecular-Dynamics. *Journal of Computational Physics, 117*(1), 1-19. doi:10.1006/jcph.1995.1039

Priezjev, N. V., & Troian, S. M. (2006). Influence of periodic wall roughness on the slip behaviour at liquid/solid interfaces: molecular-scale simulations versus continuum predictions. *Journal of Fluid Mechanics, 554*, 25-46. doi:10.1017/S0022112006009086

Puosi, F., Olivier, J., & Martens, K. (2015). Probing relevant ingredients in mean-field approaches for the athermal rheology of yield stress materials. *Soft Matter, 11*(38), 7639-7647.

Ranquin, A., Versées, W., Meier, W., Steyaert, J., & Van Gelder, P. (2005). Therapeutic nanoreactors: combining chemistry and biology in a novel triblock copolymer drug delivery system. *Nano Letters, 5*(11), 2220-2224.

Rapaport, D. C. (2004). *The art of molecular dynamics simulation* (2nd ed.). Cambridge, UK ; New York, NY: Cambridge University Press.

Saunders, B. R., & Vincent, B. (1999). Microgel particles as model colloids: theory, properties and applications. *Advances in Colloid and Interface Science, 80*(1), 1-25. doi:10.1016/S0001-8686(98)00071-2

Scheffold, F., Cardinaux, F., & Mason, T. G. (2013). Linear and nonlinear rheology of dense emulsions across the glass and the jamming regimes. *Journal of Physics: Condensed Matter, 25*(50), 502101. doi:10.1088/0953-8984/25/50/502101

Seth, J. R., Cloitre, M., & Bonnecaze, R. T. (2006). Elastic properties of soft particle pastes. *Journal of Rheology, 50*(3), 353-376.

Seth, J. R., Cloitre, M., & Bonnecaze, R. T. (2008). Influence of short-range forces on wall-slip in microgel pastes. *Journal of Rheology, 52*(5), 1241-1268. doi:10.1122/1.2963135

Seth, J. R., Locatelli-Champagne, C., Monti, F., Bonnecaze, R. T., & Cloitre, M. (2012). How do soft particle glasses yield and flow near solid surfaces? *Soft Matter, 8*(1), 140-148. doi:10.1039/c1sm06074k

Seth, J. R., Mohan, L., Locatelli-Champagne, C., Cloitre, M., & Bonnecaze, R. T. (2011). A micromechanical model to predict the flow of soft particle glasses. *Nature Materials, 10*(11), 838-843. doi:10.1038/Nmat3119

Shahid, M., Farooqi, Z. H., Begum, R., Arif, M., Wu, W., & Irfan, A. (2020). Hybrid microgels for catalytic and photocatalytic removal of nitroarenes and organic

dyes from aqueous medium: a review. *Critical Reviews in Analytical Chemistry, 50*(6), 513-537.

Shu, R., Sun, W., Wang, T., Wang, C., Liu, X., & Tong, Z. (2013). Linear and nonlinear viscoelasticity of water-in-oil emulsions: Effect of droplet elasticity. *Colloids and Surfaces A: Physicochemical and Engineering Aspects, 434*, 220-228.

Sollich, P. (1998). Rheological constitutive equation for a model of soft glassy materials. *Physical Review E, 58*(1), 738-759.

Subbiah, R., Hipfinger, C., Tahayeri, A., Athirasala, A., Horsophonphong, S., Thrivikraman, G., . . . Zahariev, A. (2020). 3D Printing of Microgel‐Loaded Modular Microcages as Instructive Scaffolds for Tissue Engineering. *Advanced Materials, 32*(36), 2001736.

Thorne, J. B., Vine, G. J., & Snowden, M. J. (2011). Microgel applications and commercial considerations. *Colloid and Polymer Science, 289*(5-6), 625-646. doi:10.1007/s00396-010-2369-5

Tighe, B. P., Woldhuis, E., Remmers, J. J. C., van Saarloos, W., & van Hecke, M. (2010). Model for the Scaling of Stresses and Fluctuations in Flows near Jamming. *Physical Review Letters, 105*(8), 088303. doi:10.1103/PhysRevLett.105.088303

Tzoumaki, M. V., Karefyllakis, D., Moschakis, T., Biliaderis, C. G., & Scholten, E. (2015). Aqueous foams stabilized by chitin nanocrystals. *Soft Matter, 11*(31), 6245-6253.

van Hecke, M. (2010). Jamming of soft particles: geometry, mechanics, scaling and isostaticity. *Journal of Physics-Condensed Matter, 22*(3), 033101.

Vasisht, V. V., Dutta, S. K., Del Gado, E., & Blair, D. L. (2018). Rate Dependence of Elementary Rearrangements and Spatiotemporal Correlations in the 3D Flow of Soft Solids. *Physical Review Letters, 120*(1), 018001.

Vlassopoulos, D., & Cloitre, M. (2014). Tunable rheology of dense soft deformable colloids. *Current Opinion in Colloid & Interface Science, 19*(6), 561-574. doi:10.1016/j.cocis.2014.09.007

Wang, Y., Guo, L., Dong, S., Cui, J., & Hao, J. (2019). Microgels in biomaterials and nanomedicines. *Advances in Colloid and Interface Science, 266*, 1-20.

Wilke, P., Coger, V., Nachev, M., Schachschal, S., Million, N., Barcikowski, S., . . . Pich, A. (2015). Biocompatible microgel-modified electrospun fibers for zinc ion release. *Polymer, 61*, 163-173.

Wouters, A. G., Schaefer, S., Joye, I. J., & Delcour, J. A. (2019). Relating the structural, air-water interfacial and foaming properties of wheat (Triticum aestivum L.) gliadin and maize (Zea mays L.) zein based nanoparticle suspensions. *Colloids and Surfaces A: Physicochemical and Engineering Aspects, 567*, 249-259.

Wu, C., Böttcher, C., & Haag, R. (2015). Enzymatically crosslinked dendritic polyglycerol nanogels for encapsulation of catalytically active proteins. *Soft Matter, 11*(5), 972-980.

Zhang, X., Lorenceau, E., Basset, P., Bourouina, T., Rouyer, F., Goyon, J., & Coussot, P. (2017). Wall slip of soft-jammed systems: A generic simple shear process. *Physical Review Letters, 119*(20), 208004.

Zhang, X., Lorenceau, E., Bourouina, T., Basset, P., Oerther, T., Ferrari, M., . . . Coussot, P. (2018). Wall slip mechanisms in direct and inverse emulsions. *Journal of Rheology, 62*(6), 1495-1513.

Zwanzig, R., & Mountain, R. D. (1965). High ‐ frequency elastic moduli of simple fluids. *The Journal of Chemical Physics, 43*(12), 4464-4471.